Time-Resolved Whole Field Investigation of the Phenomena of Laser Produced Plasma-Induced Shockwaves in Media of Different Densities

Submitted in partial fulfilment of the requirements

for the degree of

Doctor of Philosophy

of the
Indian Institute of Technology Bombay, India
and
Monash University, Australia

by

Kaushik Choudhury

Supervisors:

Prof. Atul Srivastava (IIT Bombay)

Prof. Ajai Kumar (Institute for Plasma Research, Gandhinagar, India)

Prof. Wenlong Cheng (Monash University)

The course of study for this award was developed jointly by
the Indian Institute of Technology, Bombay and Monash University, Australia
and given academic recognition by each of them.
The programme was administered by The IITB-Monash Research Academy

2017

Dedicated to

My parents and teachers

Declaration

I declare that this written submission represents my ideas in my own words and where others' ideas or words have been included, I have adequately cited and referenced the original sources. I also declare that I have adhered to all principles of academic honesty and integrity and have not misrepresented or fabricated or falsified any idea/data/fact/source in my submission. I understand that any violation of the above will be cause for disciplinary action by the Institute and can also evoke penal action from the sources which have thus not been properly cited or from whom proper permission has not been taken when needed.

Notice 1

Under the Copyright Act 1968, this thesis must be used only under the normal conditions of scholarly fair dealing. In particular no results or conclusions should be extracted from it, nor should it be copied or closely paraphrased in whole or in part without the written consent of the author. Proper written acknowledgement should be made for any assistance obtained from this thesis.

Notice 2

I certify that I have made all reasonable efforts to secure copyright permissions for third-party content included in this thesis and have not knowingly added copyright content to my work without the owner's permission.

[redacted]

Student Name: Kaushik Choudhury

IITB ID: 114174004

[redacted]

Approval Sheet

The thesis entitled "*Time-Resolved Whole Field Investigation of the Phenomena of Laser Produced Plasma-Induced Shockwaves in Media of Different Densities*" by *Kaushik Choudhury* is approved for the degree of **Doctor of Philosophy**

[redacted]

(Prof. Ashwini K. Sharma)
External Examiner

[redacted]

(Prof. Suneet Singh)
Internal Examiner

[redacted]

(Prof. Atul Srivastava)
IITB Supervisor

[redacted]

(Prof. Wenlong Cheng)
Monash Supervisor

[redacted]

(Prof. Ajai Kumar)
External Supervisor
(IPR, Gandhinagar)

[redacted]

(Prof. Sreedhara Sheshadri)
Chairman

Date: 18 December 2017
Place: Mumbai, India

Abstract

Experimental investigation of the phenomena of laser produced plasma-induced shockwaves in media of different densities (air as well as liquids) has been carried out using non-intrusive and real time diagnostic techniques. One of the refractive index-based imaging techniques, namely laser interferometry has been employed to map the field of interest. In order to record the transients associated with the plasma plume, a Mach Zehnder interferometer has been coupled with an intensified charge coupled device (ICCD) camera. An Nd: YAG laser operating at its fundamental wavelength (1064 nm) at a repetition rate of 10 Hz with a pulse duration of 6 ns has been employed to achieve the process of laser ablation. Majority of the experiments reported in the present thesis have been carried out with copper as the target material. A select set of experiments have also employed titanium as the target material (these experiments were performed to understand the effect of target material on the shape and/or size of the nanostructures produced as a result of the process of laser ablation in liquids). For any given target material, the influence of the presence of physical boundaries placed in the vicinity of the ablation site on the dynamics of the shockwaves propagating through the medium has been studied. These experiments clearly brought out the plausible role(s) of the different configurations of the physical barriers (placed parallel and/or perpendicular with respect to the target) on the density of the ambient medium, which in turn was seen to have significant impact on the size and size distribution of the resultant nanostructures produced as part of the process. The whole field data recorded in the form of transient evolution of the interferometric images provided a direct evidence of the back reflection of the shockwaves from the physical boundaries placed around the ablation site. The phenomenon of reflection of shockwaves from the confining boundaries led to a periodic compression of the ambient medium, thereby affecting the medium density as part of the process. Boundaries of the propagating shockwaves have been identified in the form of sharp deformation of the interference fringe patterns in the field of view. The recorded interferometric images have been quantitatively analysed using the customised data reduction algorithms, developed as part of the present work, to retrieve the whole field data of refractive index, mass density (of the ambient) and charge density (primarily the electronic charge density in the plume region).

Effect of density of the medium on the characteristics of the shockwaves has been studied by performing laser ablation experiments in liquid media of different densities (water,

25% (w/w) and 50% (w/w) aqueous solutions of ethylene glycol with densities of 1.0203 gm/cm^3 and 1.0446 gm/cm^3 respectively). Observations made in the liquid media have also been compared with those of the experiments conducted with air as the ambient medium. As compared to liquids, a sharp and distinctly visible shockfront was to be seen in the experiments conducted with air as ambient medium. The observed differences in the nature of the shockfronts have been attributed to the existence of multiple secondary shockfronts that were observed to be following the primary shockfront in the shadowgraph images in the case of laser ablation in liquid. These shockfronts resulted from the reflection of the stress wave (that has its origin at the point where the laser strikes the target and travels further inside the target material) from inside of the target material. Thus, the observed perturbation of the medium density was the resultant of multiple shockwaves propagating through it. The shockfront was seen to be spread over a larger distance (i.e. wider) in the case of liquid ambient in contrast to a much sharper and distinct shockfront that was observed with air ambient. Another significant observation that has been made from the liquid-based experiments is that the lifetime of the plasma depends on the density of the ambient liquid. In a medium of higher density, the plasma has been seen to thermalize faster in comparison to a medium of lower density.

The potential of the presence of confining physical boundaries placed on either side of the ablation site in controlling the size and size distribution of nanoparticles produced as a result of laser ablation of metallic target placed in liquid medium has also been explored. The study has been motivated by the fact that the presence of physical boundaries leads to a longer thermalisation time of the plasma plume produced as a result of the interaction of the high energy short laser pulses with the target material. Thermalisation time of the plasma plume has a direct impact on the size distribution of the nanostructures produced through the laser ablation in liquid. As part of this study, experiments have been performed in two different liquid media (water and isopropyl alcohol) and two different target materials (copper and titanium). For any given combination of liquid medium and target material, two target configurations have been employed; first; open (flat) target wherein no confining boundaries are present on the target surface, and second; the target surface is fitted with two aluminium walls as the confining boundaries placed equidistantly on either side of the ablation site. Results of the experiments revealed that the nanoparticles (nanostructures) produced through the ablation of target with confining geometries are significantly larger in size as compared to those obtained through the ablation of flat targets, irrespective of the type of target material and liquid medium employed. This study holds its importance in view of the fact that it successfully demonstrates the potential of the proposed methodology as one of the simpler, yet effective ways of controlling the size and size distribution of nanoparticles through laser ablation of metallic target in liquid medium, which is one of the relatively greener methods in comparison to the other conventionally employed methods, e.g. chemical methods.

Effect of application of electric field during the process of laser ablation has also been explored towards the final stages of the present work. Although plasma is inherently quasi-neutral, still the negative and positive charges present in the plume respond differently to the applied external electric and magnetic fields. The available literature shows that electric field affects the size of the nanoparticles produced due to the process of laser ablation. For the present set of experiments, the target itself has been biased (while being immersed in the experimental liquid medium) and the other electrode has been placed at a fixed distance from the target and parallel to it. Three different cases have been considered; in the first case, the target has been given a positive bias while the other electrode has been grounded; in the second case, the target has been given a negative bias while the other electrode was maintained on ground potential and finally, in the third case, no bias has been applied to the target material. It has been observed that in the case of applied bias, the particle sizes are significantly different as compared to those produced in the case when no bias was applied. Through the findings of the initial sets of these experiments (that are currently underway), the importance of electric field assisted laser ablation in liquid (EFLAL) in controlling the size of the nanostructures has been demonstrated. However, the technique also has the potential to control the shape of the nanostructures by facilitating the oriented growth, an area that forms the future scope of the present work.

Table of Contents

List of Figures

List of Tables

Nomenclature

A	DC component of the intensity function
α	Smoothening parameter (range: 0.1-1)
α_m	Molecular polarisibility
B	Amplitude of the sinusoidal component of the intensity function
β	Angle of incidence of shockwave
c	Speed of light
γ	Ratio of specific heat capacities of air
δ	Angle of reflection/deflection of shockwave
e_0	Electronic charge
ϵ	RMS error
ϵ_0	Permittivity of free space
ε	Optical path length ($\lambda.\Delta\varphi/2\pi$)
f	Modulating frequency (spatial frequency of interferogram)
I	Intensity function of the recorded interferogram
J_0	Basel function of zero order
η	Interpolation parameter (range: 0.0001 to 0.1)
θ	Orientation of the fringes with respect to the x-axis
$\Delta\theta$	Change in orientation
λ	Wavelength of the light
λ_l	Spatial fringe separation
M	Mach number
M_a	Mass of the ambient gas in the shockfront
M_p	Ablated mass in the plume
m	Molecular mass
m_e	Mass of electron
N	Number of pixels in the image, along the axis perpendicular to the symmetry axis
N_A	Avogadro's number
N_e	Charge density
n	Refractive index of the test medium
n_∞	Refractive index of the background
P_i	Pressure at the incident shockfront

P_r	Pressure at the reflected shockfront
R	Radial extent ($N \times pixel\ size$)
ρ	Number density of particles constituting the medium
ρ_b	Mass density of background
ρ_m	Mass density of medium
ρ_s	Mass density at shockfront
S	Range of the scaling factors
s	Scale factor for the mother wavelet
σ	FWHM of the Gaussian function
T_b	Temperature of the background
T_i	Temperature at the incident shockfront
T_r	Temperature of the reflected shockfront
T_s	Temperature of the reflected shockfront
V_p	Plume velocity
V_s	Shock velocity
φ	Phase
φ_a	Actual phase
$\Delta\varphi$	Phase difference
ψ	Morlet wavelet
W	Wavelet coefficient
ω_0	Amplitude factor

Chapter 1: Introduction

The phenomenon of laser ablation (LA) finds importance in a wide range of applications of scientific and technological importance, such as, thin film deposition, preparation of nanoparticles, surgical tools in the field of medicine etc. The available literature in the concerned field shows that this subject has attracted the attention of researchers well over the past five decades and still there has been a considerable interest in understanding this process from a fundamental viewpoint [1-3]. Over the years, the process of laser ablation has been primarily studied in two regimes; ablation in air/gas based ambient and ablation with liquid/water as the surrounding medium. LA in air needs to be understood from the point of view of laser-induced breakdown spectroscopy (LIBS), material processing and elemental analysis [4-7]. Contrary to that, ablation in liquid ambient has applications in the field of medicine and life-sciences, owing to the fact that, entities like tissues, cells etc., have good amount of water content [8-14]. Apart from this, LA has been used as one of the methods for fabrication of nanostructures/nanoparticles in the liquid media [15-18]. Over the years, LA has evolved as both a processing as well as a potential diagnostic technique.

The mechanism of LA involves many complex processes, depending on factors like, the kind of laser source being used (visible/IR/UV), the pulse duration (nanosecond/femtosecond) etc. For example, response of a target material changes depending on the wavelength of the laser employed for ablating the material, and hence different kinds of lasers are used for processing different materials and achieving different end goals [19-20]. Similarly the pulse duration affects the threshold laser fluence required to ablate a certain material because of the differences in the processes involved leading to LA [3, 21].

Of all the processes that are associated with the phenomenon of LA, the laser produced plasma (LPP) plume and its interaction with the surrounding medium has been of considerable interest among the researchers in the field. The interaction of a high power short laser pulse, as it hits the metal target, leads to an almost instantaneous generation of plasma plume starting from the target surface. The characteristic features of this plasma plume include very high pressure, density and temperature. The presence of strong pressure gradients in the medium leads to a sudden expansion of the LPP plume and hence the process is considered to be nearly adiabatic in nature. As this expanding plume compresses the surrounding ambient medium (gas/liquid), it transfers its momentum and kinetic energy to the medium in a very short span of time, thereby resulting in the generation of a shockwave in the medium. The region of the medium that is compressed and prevails ahead of the propagating plume can be identified as the shock front. Thus, the shock front propagates with a velocity that is relatively higher than the velocity of the plume (soon after the ablation process has taken place). This process has been schematically shown in the Figure 1.1 below, which is inspired from a published research article [22].

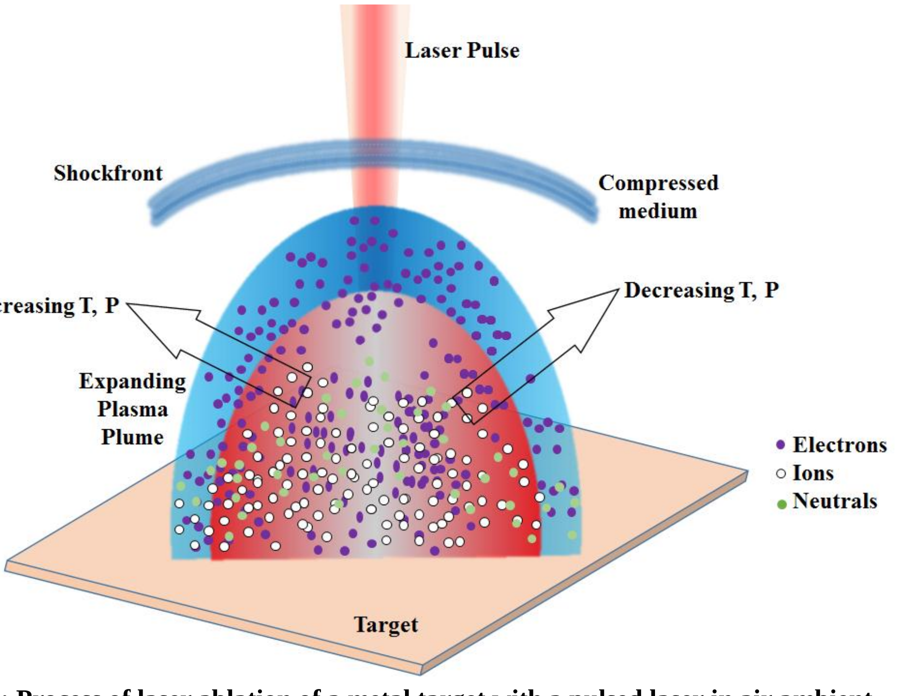

Figure 1.1: Process of laser ablation of a metal target with a pulsed laser in air ambient.

In the case of laser ablation in liquid (LAL), apart from the shockwaves, cavitation bubble is also very important. Cavitation bubble forms due to the sudden evaporation of metal and the ambient liquid. The cavitation bubble comprises of the plasma, neutral particles and the metal and liquid vapour. This bubble expands with time, under the influence of the pressure at its interior, till the point where the pressure inside the bubble matches the external hydrostatic pressure. Till this point, the plasma cools and the pressure follows a downward trend. Due to this when the pressure at the interior falls below the external pressure, the bubble starts collapsing leading to the heating of the plasma at its interior. After a certain point when the pressure at the interior becomes greater than the external pressure, the bubble starts expanding again. This cyclic process of expansion and compression goes on for a while and then finally the bubble collapses releasing the nanoparticles in the ambient liquid. This process has been extensively studied experimentally and a wide range of theoretical models have also been developed [11, 15, 23-25].

The survey of the literature carried out on the basis of the studies reported by various researchers in the past shows that the emphasis of the experimental and/or numerical models has primarily been laid on the characteristics of LPP plume and shockwaves during their early stage of formation. However for various applications, e.g. preparation of nanoparticles through laser ablation of metals, the understanding of the effect of shockwaves on the ambient medium during relatively later time instants (~ tens of μs) becomes important. Moreover, from the application point of view, the time over which the plasma cools down and condenses in the form of nanoparticles is one of the important parameters. In this context, it is believed that, a detailed understanding of the effects of forward moving and the reflected shockwaves on these lifetimes would let us have greater control over the size and size-distribution of the nanoparticles.

As discussed above, the process of laser ablation is important from the point of view of fabrication of nanostructures. Several efforts have been made in this direction [18, 26, 27]. Metallic nanoparticles have been of significant scientific interest since long [28-30]. The nanoparticles have been used for several applications, ranging from cosmetics to medicine to paints and emulsions, since ages now. Gold and silver nanoparticles top the list followed by copper and some other metals [15, 16, 31-33]. Now a days, nanoparticles have found applications in the fields of sensors, drug delivery and other such relatively newer areas of research [32, 34-36].

There are several methods of preparation of nanoparticles, which may be broadly categorised into wet or chemical methods and physical methods. Researchers in the field have devised a range of methods to synthesise nanoparticles in colloid or grow them using seed nanoparticles. Not only that, nanoparticles of different shapes and sizes have also been synthesised [37–39]. These methods produce nanoparticles suspended in a host medium. Nanoparticles produced by these methods have been used widely for bio-medical and electro-chemical applications.

Physical methods involve processes like ball-milling, sputtering, ablation etc. Ball milling provides a very fundamental approach to nanoparticle fabrication, whereby a material is ground and reduced to a nanoparticles. This method is commonly used for making non-metallic and metallic nanoparticles [18, 40]. Laser ablation, on the other hand, provides a method that is more sophisticated in nature and when employed, apart from formation of nanoparticles, disseminates a lot of compositional information about the material itself [15, 23, 26, 33]. Preparation of nanoparticles by laser ablation of metals is governed by the physics of laser-matter interaction. From this point of view, the study of laser-produced plasma-induced shockwave generation and propagation is of immense importance.

Currently, the idea of nanofabrication is not just confined to nanoparticles. It has rather grown into a bigger arena of research and development and encompasses different shapes of such nanostructures ranging from cubes to cages to prisms and even complex dendritic structures [18]. The shape control has been explored since quite some time now and has been achieved primarily by chemical means [42-45]. Mostly, researchers have achieved this feat of shape control by varying the concentration of capping agent (that arrests the growth along one crystallographic plane while not affecting the others) or by changing process parameters like temperature, pressure etc. Similar attempts have been made in the case of laser ablation. For instance, researchers have used electric field as one of the means to control the shape of the nanoparticles that result from the phenomena of laser ablation [45, 46].

To observe and understand the phenomena of LPP and the subsequent processes (and their plausible effects), most of the research groups have resorted to the use of spectroscopy and ICCD-based fast photography techniques as the primary diagnostic tools. These diagnostics have provided insights into the various processes that occur during different phases of the plume formation and expansion [6, 7, 48-52]. As is known, spectroscopy is one of the widely used and most effective methods for finding the temperature and density of the plume. Also, it gives information about the structural composition of the target material (which eventually leads to a completely different field of research namely, laser-induced breakdown spectroscopy (LIBS)). Contrary to this, most of the studies performed to understand the shockwave phenomenon and the cavitation bubble have used intensified charge coupled device (ICCD)-based shadowgraph imaging technique as the primary diagnostic tool [12, 53-55]. Nevertheless, this technique has been successful in disseminating information on the shape of the shockwave, shock temperature, shock pressure and shock velocity in different media; it lacks the ability to accurately map the whole field in quantitative terms. However, it is interesting to note that Mach Zehnder interferometry (MZI) has also been used as a tool to observe the charge density and change in the density of the medium induced by the shock that is created due to the plume expansion. MZI integrated with ICCD-based fast photography has come up as an effective diagnostic tool [56-59].

A vis-à-vis comparison of the various diagnostic tools reveals that spectroscopy gives us information about the plume and its properties, like constitution of the plume (proportion of ions, electrons and neutrals), the temperature of the plume, the state of ionisation of the ions present in the plume etc. However, it is unable to give any directly quantifiable information on the shockwave or medium compression. Shadowgraph provides information about the density variations in the medium due to shock, as it clearly shows the shock boundary or the region with maximum changes in refractive index (RI). A time-correlated study also shows the evolution of the shockfront. Not only that, when laser ablation is performed in liquid media, shadowgraph images have been able to capture the phenomena of formation and oscillation of the cavitation bubble and the release of nanoparticles in the medium (in the case of ablation of solid targets). On the other hand, interferometry, specifically Mach Zehnder interferometer (MZI), puts forth a method of differential measurement and is able to reveal any variation in the RI field of the medium, be it a lowering of the RI because of the presence of the negatively charged electrons or be it a rise of RI because of the compression resulting from the propagating shockwave. As has been discussed in Chapter 3, this technique has been exploited well for these measurements. In the case of a process like LPP and the subsequent processes which occur in the duration of nano and micro-seconds, all these measurements be it, spectroscopy or shadowgraphy or be it interferometry need very fast methods of capturing the images. ICCD-based imaging is one such method. In view of this, all the three methods discussed above employ ICCD as the capturing device. Here it is important to mention that interferometry is a superior method compared to shadowgraphy, for two reasons – first, it is based on the concept of differential measurements so the accuracy is high, and second, the error is less in the case of the processing of interferometric data. Shadowgraph provides second derivative of the RI (n), and hence, to generate the RI map of the whole field of view from the shadowgraph data, one needs to integrate the data twice, whereas to extract the same information from an interferometric images, one needs to integrate the data just once [59]. Thus, RI field reconstructed from the interferometric images have lesser scope for error as compared to that reconstructed from the shadowgraphic images.

With this background, the present work is concerned with a detailed investigation of the phenomena of laser produced plasma-induced shockwave propagation in the media of different densities. The absence of a method that could accurately map the whole field medium (mass) density and charge (electron) density perturbation, following the laser pulse hitting the target material, was a strong motivation behind taking up this work. As mentioned in the previous paragraphs, the use of the process of laser ablation for producing nanoparticles is in practice since quite some time and it is known that the nanoparticles result from the cooling down (thermalisation) of the plasma resulting from the ionization of the target occurring due to the laser pulse hitting the target material. This plasma expansion causes generation and propagation of shockwaves in the ambient medium which leads to the formation of a region of a high density (shockfront) and the trailing low density region behind the shockfront. These propagating shockwaves have been extensively probed by means of ICCD-based interferometric technique to get a detailed quantitative information the refractive index (RI) field and the corresponding time-evolution of the density distribution of the medium, as the shockwaves propagate. Furthermore, physical boundaries have been fitted on the target surface so as to facilitate the reflection of the shockwaves. The physical boundaries were put laterally (in form of aluminium walls) and longitudinally (in form of aluminium top plate) to study the effect of reflection of the shockwaves on the medium density distribution and on the charge density distribution in the plume. The comparison of the results obtained with and without any confinement show significant differences in the time evolution of the RI field and hence in the distribution of mass and charge density at different instants of time after the ablation has taken place. These studies have revealed that the medium mass density and the electron density in the plasma plume are significantly affected by the presence of physical confines in the close vicinity of the ablation spot.

Having carried out these studies on air ambient, the experiments were conducted to characterise the laser produced plasma-induced shockwaves in liquid media of different densities. It was observed that the density of the medium has a significant role to play in the shockwave propagation and the lifetime of the plasma plume. The ambient medium density and the presence of confining boundaries both were seen to be playing crucial roles in altering the lifetime of the plasma plume. Having understood this, the laser ablation in liquid (LAL) was carried out with high purity copper and titanium targets as the target materials and water and isopropyl alcohol as the ambient fluids. Also, for every target material, two different geometries of the target plate were considered. In one case, the target surface was flat and was kept beneath a fixed liquid column, whereas in the other case, the target plate had aluminium walls on either side of the ablation site, causing reflection of the shockwave. The findings showed that there was an appreciable difference in the sizes of the nanoparticles that were formed due to the ablation of a target material(s) with and without confining boundaries for any given target-liquid combination. The present work is expected to provide useful insights on the effect of the shockwave and reflected shockwave resulting from the expansion of plasma plume on the shape and size of the nanostructures formed due to laser ablation of metals placed in liquid medium.

The present thesis has been organised in six chapters, first being the present chapter, which has given an overview and scope of the research work that has been carried out. The references that have been included in this chapter are to show that how the present work aligns with the existing literature. It also gives a glimpse of the relevance of the present work vis-à-vis the existing sphere of knowledge. The second chapter is a brief account of the literature that has been surveyed before these studies were undertaken. Significant research outcomes have been discussed appropriately in this chapter. The third chapter deals with the instrumentation aspects of the experiment. It includes the technical details pertaining to the crucial and major experimental components used in the study. The fourth chapter is on the data reduction methods and tools. It discusses the methodology that has been adhered to for retrieving the RI field distribution from the recorded interferometric images. It also discusses the relation of the RI field and the various physically observable variables like, charge density, mass density etc. The fifth chapter comprises of detailed analysis of the results and the interpretation of the analysed data. This chapter gives a perspective on how the results obtained have been exploited to gain control over the size and size distribution of the nanoparticles resulting from the process of laser ablation of metallic targets. The last chapter highlights the conclusions of all the studies performed and gives an outlook to the directions that may be taken in future.

Chapter 2: Literature Survey

The subject of laser ablation has been one of the widely studied topics in the area of laser-matter interaction due to its importance in several scientific and technological applications. There is a range of published literature on the various methods in which laser ablation is carried out, for example, laser ablation in gas/vacuum, laser ablation in liquid etc. which shows that extensive studies were carried out in this domain [3, 60, 61]. A very lucid description of the series of events that led to the advent of laser ablation as a field of study and its evolution to this current state may be found in the works of Miller [62, 63]. A detailed survey of the existing literature in this area was done. A brief account of the same follows henceforth.

To begin with, the present work is primarily about the laser-produced plasma-induced shockwave and its effect on the medium density. The studies have been carried out with different ambient mediums, air, water, 50% aqueous solution of ethylene glycol (w/w) and 25% aqueous solution of ethylene glycol (w/w). The reason behind the choice of media is their varying densities. Also, water and ethylene glycol are used as coolants, so ablation in these media may be seen as a method to generate nanoparticle suspensions, which enhances the cooling capacity of these liquids to a great extent [64]. Studies on the reflection of shockwaves have also been performed by putting physical barriers in the vicinity of the ablation site. In the end the laser ablation of metal targets have been carried out in the liquid ambient, with and without putting a barrier in the vicinity of the ablation cite. Therefore, in context of the present work the literature survey has been broadly categorised into three sections *viz*. laser ablation, fabrication of nanostructures, Mach Zehnder Interferometry.

2.1 Laser ablation

The ablation of metals by laser has been investigated since long [3, 53, 66-69]. Laser ablation is carried out in vacuum, gas-atmosphere and in liquid ambient based on the desired end result. Researchers have studied these phenomenon in different ambient, viz. air, water, gasses at different pressure, and also between confining surfaces [5, 53, 69, 70]. The objectives were mainly to understand the distinct processes that take place in the course of ablation. Laser matter interaction and interaction of either of these with the ambient, triggers different physical processes [3, 7, 17, 66, 71] . These studies become important from the point of view of science and engineering because of involvement of plasma production and its use in sputtering (which happens to be a very precise method for thin film deposition) and elemental analysis (laser spectroscopy for analysis of composition of the specimen being ablated) [72]. Also, there are applications of laser ablation in the field of biomedical engineering, where it is used as a tool to ablate biological cells and tissues [73].

A very fundamental work on modelling the interaction of laser pulse with matter and subsequent plasma formation and plume expansion was accomplished by Singh *et. al.* [74]. In this work the plasma plume was assumed to be behaving like an ideal gas at high pressure and temperature. They theoretically analysed the effect of most of the beam and substrate parameters (spot size, energy density, atomic mass of the substrate etc.) on the plume and its expansion. This model predicted most of the features of the film that is deposited using pulsed laser evaporation. Although this work was carried out to understand and predict the process of pulsed laser evaporation this throws light on fundamental aspects of the plasma generation and plume expansion. Another interesting experiment was carried out by Anthes *et. al.* in 1978, where they observed the fast-ions, generated as a result of ablation of target being irradiated by 8 ns pulsed Nd: glass laser, using a Faraday cup and Thomson parabola. [75]. This is probably one of the early experiments performed to observe laser ablation and its effects. Here the experimental results were also corroborated with a model.

One of the most interesting parameters to study when it comes to the study of laser ablation is the amount of mass ejected from the substrate. This aspect is important when it comes to certain applications like thin film deposition or fabrication of nanoparticles. Different models, both analytical and empirical, were proposed to estimate the ejected mass and its dependence on parameters like, laser fluence, laser wavelength etc. In this regard the notable works were carried out by many research groups at different times and at different places. Dahmani and co-workers, in their paper have shown the wavelength dependence of the ablation rate and ablation pressure [76]. Burdt *et.al.* have, in their work, presented an experimentally established relation for the ablation rate [77]. They have shown that the ablation depth scales to the power of 5/9 with the laser intensity. Torrisi *et.al.* have shown the dependence of ablation yield on the laser fluence. They have done it for two different wavelengths and have shown that the required fluence for producing same ablated mass depends on the wavelength of the ablating laser [20]. The experiments carried out with 1064 nm and 308 nm laser showed that the threshold energy requirement for ablation is less for shorter wavelength.

Apart from free expansion of the plasma plume, researchers have also studied the effect of confinement on the process of laser ablation. In this regard the work carried out by

Fabbro *et. al.* is very significant. Here, a physical model has been developed to understand the laser ablation process and the pressure generated due to the shockwave in a confined geometry [68]. Experimentally it was pointed out that the longer laser pulses (in 6 – 30 ns range) generate more pressure and the pressure generated in a confined geometry is much higher compared to the open geometry. This work also underlined the fact that the amount of pressure generated is limited by the extent of ionization that takes place because of the laser-matter interaction.

In the similar lines, Yeates and co-workers studied the plasma parameters (electron and ion densities and temperatures), by putting physical barriers and arresting the free expansion of plasma [78,79]. These works are very much related to the work that has been carried out in this thesis. The studies of Yeates *et. al.* show that carrying out laser ablation in a confined geometry cause the reflection of shockwave, which in turn alters the plasma lifetime, charge density and temperature. These studies were performed using ICCD and spectroscopic means. They have also shown that the effect of lateral and longitudinal confinement are different from one another.

Recently Kumar *et. al.* have studied the dynamics of Li plume in the confined geometry using ICCD-based fast shadowgraphic and spectroscopic technique [71]. This work was fundamental in nature from the point of view of understanding the effects of confinement. A vis-à-vis comparison of the plasma parameters was made between the two cases, namely, freely expanding plasma plume and plasma plume expanding in confined geometry. It was observed that in case of confined geometry that the intensity of certain lines were increased. This observation was related to the presence of reflected shockwave in the medium.

It has been seen time and again that restricting the expansion of the plume affects the plasma parameters and the properties of the film that is formed in case of PLD. Therefore, it becomes imperative to study the process that causes these effects – the laser-produced plasma induced-shock. This process has been studied in detail in the present work. Therefore, a discussion on the outcomes of the available literature is quite relevant.

The Spatio-temporal evolution of nanosecond laser ablation plumes of Al in the Ar background at the atmospheric pressure has been studied by Harilal *et. al.* using a 1064 nm laser [54]. They observed the features of hydrodynamic expansion of plume, material ejection and shockfront using shadowgraph with the aid of an ICCD camera. They also reported the generation and propagation of a secondary shockfront resulting from the fast ejection of target material in a time window of 100 ns – 500 ns. They were able to show that most of the plume expansion features may be reproduced by using a continuum hydrodynamics model.

Ecault *et. al.* have been able to observe the shear wave propagation in epoxy-resins using a specific shadowgraphy device, based on the principle of photoelasticity. These waves are triggered in the target material in response to the interaction of laser with the target. They have calculated the velocity of shear waves and compared it to the velocity of the shock in the medium. The results were able to bring out the relation of the relation between the shear wave distributions on the initial pressure loading. These results were also corroborated with the numerical results [80].

Recently Nguyen *et. al.* have also studied the laser-induced stress waves (LSW) by ablating an epoxy-resin target. They have reported the effect of confinement of plasma using a liquid layer overlay. It was proven using the obtained results that LSW is weaker with thinner liquid layer. It had clearly been shown that the liquid film needs to be thicker than a threshold value to observe the same effect with the bulk liquid [81, 82].

Different aspects of laser ablation and laser plasma induced shockwave were also investigated from time to time. Pulsed laser deposition is one such technique that uses laser ablation as a process to produce thin layer of coatings. A review by Ashfold *et. al.* discusses about this technique and its implications [83]. Laser induced breakdown spectroscopy (LIBS) is a tool to diagnose the elemental composition of materials by spectroscopically observing the ablation plume. The atomic transition lines present in the ablation plume and their relative strengths give out the information about the components present in the target. Rusak *et. al.* have discussed about this aspect of laser ablation, which has proven to be a tool for the analytical chemists and material physicists [4].

Following the same line Harilal *et. al.* underlined the effect that the presence of shockwave has in case of laser ablation in air ambient. It describes how the shock front acts as a barrier between the plume and the ambient oxygen and resists the oxidation process at the early instants of the plume formation [84]. Masuhara has described how the proteins and other molecule get crystalised due to the presence of shock. The authors discuss how the shockwave leads to abrupt increase in the concentration of species in the liquid locally and causes crystallisation [85]. Similarly the cavitation bubble and the cavitation process has been studied extensively, by means of models and experimentation [67, 85-87]. All these efforts made by the various research groups across the globe helped us develop a holistic view of the process of laser ablation not just as a tool but as a method, as well.

When the process of laser ablation is carried out by placing the target in a liquid media, the process is commonly known as laser ablation in liquid (LAL). LAL is the corner stone for the processes leading to the formation of the nanoparticle/nanostructure. Apart from that there are biological application of laser ablation where the interaction of the laser takes place with cells in the liquid ambient. From these points of view as well, LAL holds reasonable significance. The fundamental difference between laser ablation in air/gas and laser ablation in liquid is because of the formation of cavitation bubble. It comprises of the liquid vapour and the metal vapour. Once it forms, it expands because of the internal pressure till the pressure inside the bubble matches that of the ambient. After this the bubble starts getting compressed, which in turns heats up the interior of the bubble increasing the pressure and again the bubble starts expanding once the pressure at its interior becomes large enough. This process of bubble oscillation has been explored by means of models and shadowgraphic observations. Therefore, some of the research work related to the bubble has been discussed below, however a much detailed discussion on LAL has been made in the next section in the context of fabrication of nanoparticles, as it is relevant to the present work.

Modelling of the dynamics of laser ablation-induced bubble in water was successfully carried out by Akhatov *et. al.* [11]. A mathematical model was developed considering the expansion of the bubble to be spherically symmetric. The processes like evaporation and the condensation of the liquid on the bubble wall and the effects arising due to the gas and liquid dynamics, compressibility, heat and mass transfer effects were taken into account. It accounts also for the occurrence of supercritical conditions at collapse. The numerical results obtained for the collapse and the first rebound were is good agreement with the experimental observations. This work also gives a brief description of the shockwave resulting from the collapse of the bubble.

Soliman *et. al.* modified the Rayleigh-Plesset theory of the bubble dynamics by including the kinematic viscosity, surface tension and the effect of contact angle between the water, target surface and the bubble [89]. The modification using the kinematic viscosity and the surface tension were effective especially when the ablation is to be carried out in pressurised water. The pressure and temperature inside the bubble could be evaluated using this model. However the authors of the paper suggested that the evaluation of the anomalous thermodynamic parameters could help in more accurate implementation of the model.

Lazic *et. al.* were able to observe through the cavitation bubble, probably for the first time, as the heated vapour inside the bubble with refractive index close to 1 (less than the ambient liquid, water) causes strong defocussing of the incident probe beam [70]. They were able to observe at an instant of early expanding and late collapsing phase of the bubble when its refractive index was 1.23, which is relatively closer to that of water. With this work they were able to show that, inhomogeneous clustering of vapour bubble perturbs the incoming ablation laser beam and causes irregular ablation.

Tamura *et. al.* in their work published in 2015, unfolded the relation between the nascent cavitation bubble and nascent plumes plume for improving the efficiency of LIBS while it is conducted in liquid ambient [51]. They simultaneously observed the plume and bubble at the early phase of their development and reported that in case of shorter ablation pulse (30 ns) the size of nascent plume is larger compared to the bubble, however in this case the plume quenching is fast because of its contact with water. In contrary, in case of a longer ablation pulse (100 ns) the plume remains contained inside the bubble. They suggest that by tuning the interplay between the bubble and laser pulse reasonable strong LIBS signal may be obtained at later instants of bubble expansion.

Lim *et. al.* reported formation of complex bubble geometries like, elliptical toroidal etc. by tailoring the ablating laser beam using a spatial light modulator. They studied the time evolution of the bubble experimentally and tested the results with the help of simulations [90]. They reported various dynamic features like, the inversion of the major and minor axis for elliptical bubbles, the rotation of the shape for square bubbles, and the formation of a unidirectional jet for V-shaped bubbles in both, the experiments and the simulation. They demonstrated the formation of specific bubble shapes directly through the intensity distribution of a single laser focus and reported that ideally any bubble shape may be generated using this approach.

Although, bubble is not a major part of the present thesis, still the discussion above was necessary as the bubble is an unavoidable consequence of LAL. In case like ours where the laser ablation is carried out by 8 ns pulse at a frequency of 10 Hz, bubble does not impact the process of laser matter interaction directly, but if one resorts to high repetition rate of laser pulse, say, in kHz then the bubble lifetime becomes important. In such cases the presence of bubble hinders the path of the incoming laser pulses directly affecting the ablation efficiency.

2.2 Preparation of nanostructures

Methods for the preparation of nanostructures may be broadly classified into two major categories, namely, the chemical methods and physical methods. The approaches falling under the chemical-based category comprise of methods that involve chemical ways of reduction of metal salts that lead to formation of nanoparticles from various precursors [91]. The second major category include methods that use physical means like, ball milling, sputtering etc. for producing the nanostructures [40, 92]. In addition, there exists another mode of classification based on nanostructure preparation methods – top-down and bottom-up approaches. In the top-down approach, the bulk material is broken down to form nanoparticles whereas in the second approach i.e. bottom-up approach the smaller entities like atoms or molecules are made to come together to form structures with dimensions in the range of a few nanometers.

In the recent years, laser ablation has become one of the common methods for fabrication of the nanoparticles. This method is used widely to fabricate metallic and polymeric nanoparticles [1, 92-94]. This is a relatively greener method as it does not involve harsh chemicals at any stage of fabrication. Also this method is simpler owing to the absence of chemicals that are hard to get rid of, once the nanoparticles are formed. Laser ablation is carried out in air/gas/vacuum or liquid ambient based on the desired end result. When laser ablation is carried out in air/gas/vacuum it is mostly to let the ejected solid get deposited over a substrate and the method is known as pulsed laser deposition (PLD) [74, 83]. On the other hand, when the process of ablation is carried out in liquid the metal vapour cools down and forms nanoparticles [23, 31]. This process is known as laser ablation in liquid (LAL) or sometimes, pulsed laser ablation in liquid (PLAL).

LAL has been carried out in different media, which have different viscosities, densities, refractive indices etc. so as to control the size of the nanoparticles [96, 97]. Also, the chemical interaction of the ambient medium with the target material has been exploited to generate different sizes and compositions of the nanoparticles. These different methods generate different size and size-distribution of nanoparticles with different stoichiometry [98, 99]. Literature is available on nanoparticles suspensions being used as ablation targets whereby particles of different sizes and surface morphologies distinct than the target particles were obtained [99-102]. Efforts have also been made to develop the method - electric field assisted laser ablation in liquid (EFLAL), which enables one to fabricate nanoparticles of varied shapes and sizes by applying electric field across the ablation target [45, 46, 104]. Researchers have also shown that the parameters like laser wavelength, laser fluence and height of the liquid column affect the size and size-distribution of nanoparticles [105, 106].

The wide range of applicability of nanoparticles has fuelled the research on fabrication and characterisation of a variety of nanoparticles. Over last few decades the area of research has broadened from nanoparticles to nanostructures; encompassing not just spherical or nearly spherical nanoparticles but also a plethora of structures like, prisms, cages, spindles, wires etc. [18, 107, 108]. The variation in the shape, size or surface morphology of the nanostructures leads to a change in its physical properties and response to a specific physical, chemical or biological stimulus [108, 109]. This, in turn, makes the nanoparticles a promising candidates for a host of applications in different spheres of life. The applications range from simpler ones like paints and heat exchange fluids to more involved ones like drug delivery, catalysis and quantum computation [110, 111].This necessitates the gain of precise control over the shape and size of these nanostructures.

As discussed in the preceding chapter, the scope of the present work includes the effects of propagation and reflection (from the physical boundaries) of the laser produced plasma-induced shockwaves on the formation of nanostructures. The plausible role of the presence of physical barriers on either sides of the ablation site have been thoroughly explored in the light of available literature. It therefore becomes imperative to present a brief discussion on some of the works that are relevant to the present thesis and they have been discussed below.

Dolgaev *et. al.* reported formation of a variety of nanoparticles (Ti, Si, Au and Ag) in a variety of liquid media (H_2O, C_2H_5OH and $C_2H_4Cl_2$) [26]. A high repetition rate (15 kHz) Cu-vapour laser was used to ablate the various target materials and the size distribution of the nanoparticles were studied. The dependence of the size of nanoparticles on the laser wavelength and the laser fluence were also studied. The authors also proposed that by making use of the surface plasmon resonance of the metal nanoparticles the particle size distribution may be manipulated.

Compaginini *et. al.* reported production of Au sols in *n*-alkane solutions using the second harmonic of a Nd:YAG laser (532 nm, 5 ns pulse at 10 Hz) and fluences ranging from 1 to 200 J/cm2. They reported the shape and aspect ratio control of the particle by altering the chain length of the alkane host [31]. They reported formation of high aspect ratio particles using laser fluence higher than 5 J/cm^2 and varying the chain length of the *n*-alkane. In their studies they found that for the lightest alkane used, i.e. *n*-pentane they observed an aspect ratio of 6.5, whereas for higher chain lengths the aspect ratio decreased. They also stated that after a certain limit increment of the laser fluence simply increases the yield of nanoparticles instead of having any effect on shape and size.

Mahdieh *et. al.* investigated the effect of the height of liquid column, number of laser shots, and the effect of ambient media on the size of the nanoparticle formed by laser ablation [105, 106]. They carried out the experiments with Ti and Al in water, acetone and ethanol and found out that in acetone the particle mean size is the least and the distribution is narrower. Also, with increase in the laser fluence bigger size of the nanoparticles were obtained. They attributed these features mostly to the variation in the thermos-physical properties of the target materials and the interaction of laser with the target in different media being different. They also performed experiments with Al and Ti at different depths of distilled water. They found that the height of the water column substantially affects the size and the size distribution. The same experiments were then repeated with fixed laser heights but different number of laser pulses. It was observed that the irradiating with more number of laser pulses produced smaller particles with narrower size distribution.

Werner *et. al.* in 2012 presented the new findings on size control of gold and silver nanoparticles produced by LAL [103]. They argued that the polydispersity in the particles formed by LAL are majorly because of the uncontrolled heat dissipation caused by the vapour bubble formed during the ablation. They conducted the experiments under high pressure and achieved better control over size distribution. Their work laid stress on the size control by controlling ablation wavelength, pressure and fluence for a given media and material.

Shape and size control is not a new thing when it is to be done with the help of chemical means and methods. However, the recent advancements in size control is electric field assisted laser ablation (EFLAL). This technique promises a better control not only over size but also over shape, by directing the growth of nanostructures in one direction. A review article written by Zeng *et. al.* underlines some of these developments [18].

Work of Lin *et. al.* is remarkable in this direction [45, 104]. The group claims to have developed GeO_2 micro and nanostructures using EFLAL. The ablation of the target was set to take place in between two parallel plate electrodes with the ablation site equidistant from them. They have shown that when there is no electric field spherical nanoparticles are formed. At an applied electric field of ~14 V cubes are formed whereas at 32 V spindle-shaped structures were obtained. They, in another paper reported fabrication of CuO nanostructures by electric field assisted directional growth of CuO nanoparticles. The nanospindles produced here are of different aspect ratios based on the amount of electric field applied during the process of their fabrication. This kind of fabrication is stated to be capable of wavelength-selective absorption and are useful as biomedical means. The advantage with EFLAL is that the desired structure can be fabricated in one step by appropriately setting the electric field across the ablation site.

Recently in 2017, Sapkota *et. al.* reported size control of Sn nanoparticles by EFLAL [46]. They reported a reduction in size on application of electric field across the ablation site. They argued that due to the presence of electric field the probability of recombination of ion-electron is reduced leading to an increased probability of electron capture by nanodroplets, which in turn would lead to size deformation of these droplets. This deformation leads to breaking down of these droplets under the effect of thermal agitation.

Having discussed some of the works which contributed a lot to the evolution of the field of laser ablation, in the present thesis we focus to look at the effect of propagation of the shock in the medium as a whole. In the present literature, to the best of our knowledge, the whole field study of perturbation of the medium and plume density due to the laser-produced plasma-induced shockwave and its reflection from the physical barrier (placed close to the ablation site) has not been reported. Also, we proposed a novel method of fabrication of size-controlled nanoparticles by making use of our understanding of the phenomena of interaction of reflected shock with the plume.

2.3 Mach Zehnder interferometry

To understand the process of laser ablation in detail various observation tools, both, direct and indirect, have been used from time to time. Most of the work that has been carried out in the recent past, in this direction, have used spectrometers/spectrophotometers as the primary diagnostic tools [4, 5, 23, 67, 111-116]. Apart from these, researchers have also used Rayleigh scattering as a method to find particle size distribution and time evolution of size [116-118]. These methods have been tried and tested over a range of target materials and in different media. Integration of spectroscopy with scattering signals also makes a strong diagnostic tool for characterization of plasma, commonly known as laser-induced breakdown spectroscopy (LIBS) [17, 23, 115].

Geohegan *et. al.*, for example, investigated the propagation of yttrium plasma plume in the low pressure argon background. Here they demonstrated that the ion flux gets split into the fast and slow components. They used ICCD based measurements and spectroscopic techniques to observe the phenomena experimentally [120].

Researchers have established Mach-Zehnder interferometry as one of the best methods to find spatiotemporal variation of density. The primary reason behind this is, it’s differential nature. Mach-Zehnder interferometers always determine the differential change, i.e. change in the sample with respect to the background and thus improves SNR. MZI has invariably been used in particle density related measurements [121,122]. This technique has also been used to determine plasma densities [56,121].

Zhang *et. al.* investigated the laser produced plasma by using MZI and processing the obtained interferograms by appropriate algorithms [58]. They studied the Spatio-temporal evolution of the laser-produced plume and mapped the electron density at different time instants starting from the time of ablation. They assumed the plume to be cylindrically symmetric and hence were able to generate a 3-D profile of the plume.

Ye *et. al.* employed MZI to observe the electron density distribution in plasma experiments [123]. Instead of recording separate interferograms to observe the time resolved phenomena they suggested the multiframing approach. Here a rotating mirror framing camera was used to record the interferograms at different instants. The frame rates were as high as 2.9 MHz.

Breitling *et.al.* demonstrated that the interaction of metal vapour/plasma is different with the lasers of different wavelengths using MZI [124]. They described the regions of absorption and absorption mechanisms based on the RI field that was obtained from the interferograms. In this work they were able to demonstrate the distinctive behaviour of the shockwave with the different wavelengths. Also the electron density in the plume region was precisely estimated.

Kim *et. al.* were able to show the difference in the behaviour of the plasma plume and the shockwaves in a gas field medium and in a gas jet by employing MZI as a tool [125]. They were able to tell the difference using a fluid-based model.

The work by Chen *et. al.* dates back to 1985 wherein he suggested that the transient density measurements can be done using recorded interferograms. He used the method of digitally processing the interferograms generated with a Mach Zehnder Interferometer that captured the jet of He-Ar mixture coming out of a nozzle. This is probably one of the early works where automated method was used for analysing the interferograms to reduce manual effort.

Apart from 1-D and 2-D, 3-D mapping has also been carried out. Azambuja *et. al.* characterised the 3-D profile of high density pulsed gas jets with cylindrical and non-cylindrical shapes [122]. Here they used two MZIs in orthogonal configurations. They also suggested that similar configuration and methodology may be adopted for laser plasma related studies.

Researchers have implemented digital holography as well, to map the plasma density inside a discharge tube [126]. Time and again this technique has proven its effectiveness in determination of parameters that lead to a change in refractive index [128-130]. In the present work Mach Zehnder and shadowgraphy have been employed to capture the phenomena of shockwave and the evolution of charge in the plasma dominated region.

2.4 Objectives of the present work

The above studies have practical applications in the field of material processing, micro-machining etc. Apart from these, laser-ablation has been employed to produce supersonic beams of particles for atomic and molecular studies. In the field of medicine ablation of organic materials, bioceramics etc. LA plays an important role. Colloids containing metal nanostructures with a coolant fluid as the host medium promises the potential solution to the challenge of taking out heat efficiently. The present literature available in the field has established the fact that by changing the size and shape of the nanoparticles, the heat conduction efficiency may be manipulated. Also, it has been shown by a group of researchers that the size and shape of the nanoparticles may be controlled by changing laser fluence, laser wavelength, pulse duration and the properties of the ambient medium. In this direction, the present work explores the potential of the technique of laser ablation of metallic targets in liquids as one of the simpler, yet effective methods to control the size and size distribution of nanoparticles/nanostructures. The technique is primarily based on the dependence of the thermalisation time of the plasma plume on the characteristics and/or dynamics of the propagation of laser produced plasma-induced shockwaves in media of different densities. Under such circumstances, developing a detailed understanding of the phenomena of propagation of laser produced plasma-induced shockwaves in the medium becomes important. In this context, the present thesis primarily focusses on non-intrusive diagnostics of the phenomena of shockwave propagation in the medium and its plausible impact on parameters such as, mass density (of the medium), electronic charge density (of the plume) etc. using one of the refractive index-based imaging techniques namely laser interferometry. A Mach Zehnder interferometer coupled with an ICCD camera has been employed to record the transients associated with the process. Potential applications of the primary findings of the experimental studies in the area of fabrication of the nanostructures have also been discussed.

Chapter 3: Apparatus and Instrumentation

The work reported in the present thesis is primarily experimental in nature and employs one of the non-intrusive diagnostic techniques, namely, laser interferometry, for investigating the phenomena of laser produced plasma-induced shockwaves. Factors such as stringent requirements of aligning the two arms of the interferometer, precise control over the ablation of the target material, fast and real time imaging of the entire process etc. contributed towards increasing the inherent complexities involved in the experimental work. The present chapter describes the complete experimental facility employed for developing an understanding of the phenomena of shockwave. Full view photographs of the experimental setup (laser interferometer and the ablation chamber) have been shown in Figure 3.1. The present chapter describes the various components of the complete experimental facility that includes; 1) optical layout of the laser-based interferometric setup, 2) ablation setup and 3) the related instrumentation employed to image phenomena like high speed camera, filters etc. The chapter also brings out the detailed experimental procedure along with the precautions that are needed to be taken for conducting these experiments.

Figure 3.1(a) shows the photograph of the Mach Zehnder interferometer (MZI) that was set up to observe the phase change occurring due to the process of propagation of the shockwave and plasma plume in the medium (air and/or liquid). As is seen in the image, the setup comprises of the spatial frequency filter assembly to clean the probe beam and the interferometer itself. The interferometer was illuminated by a He-Ne laser (*Research Electro-Optic Inc.*) and diode pumped solid state (DPSS) laser (*Coherent Inc.*) for two different experiments. Figure 3.1(b) and (c) show the photograph of ablation stage and glass chamber (ablation chamber) used for ablation, respectively. The ablation chamber has been separately discussed in another section of this chapter.

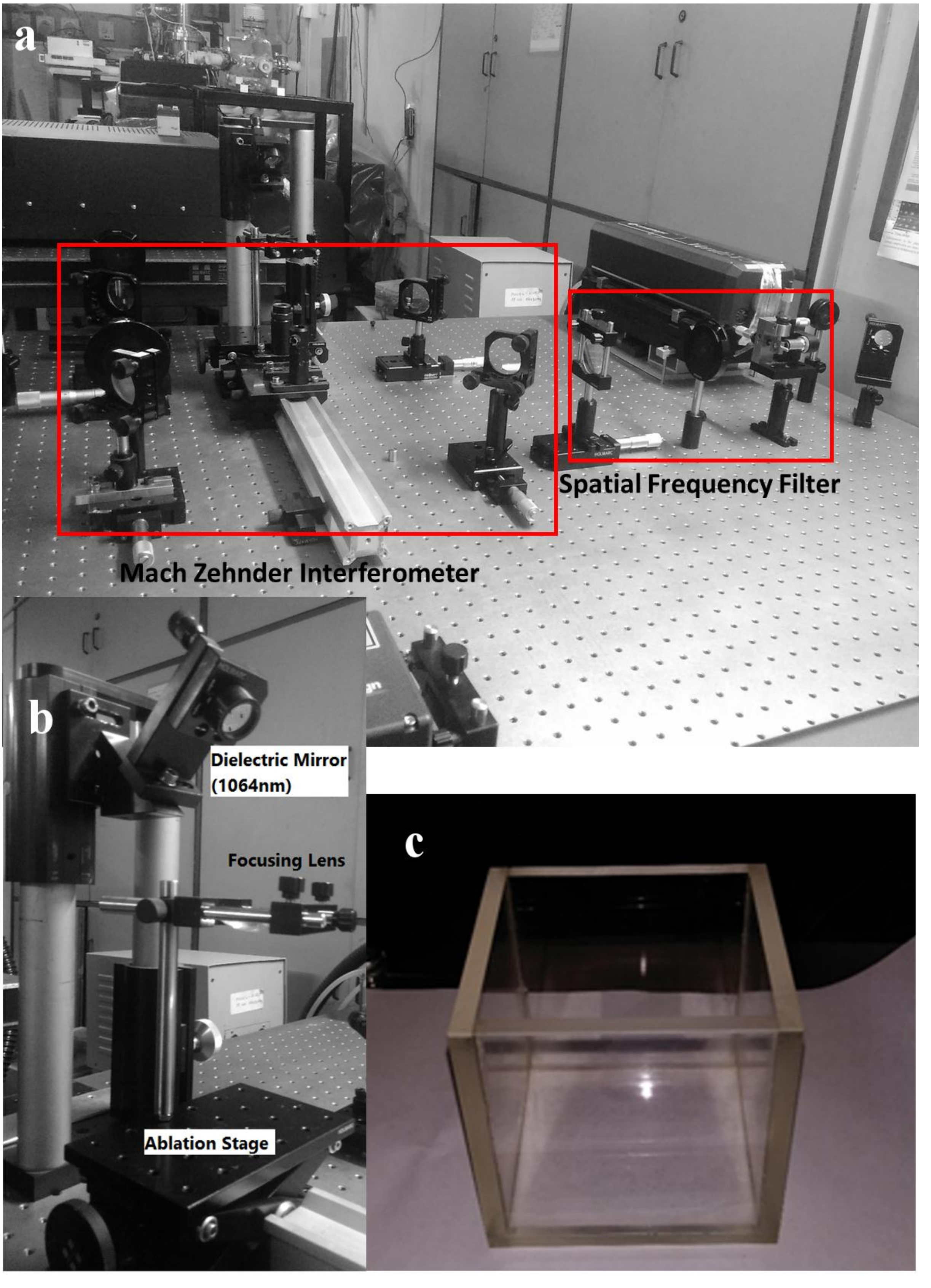

Figure 3.1: Full view images of the experimental setup, a) Mach Zehnder interferometer, b) ablation stage with focusing system and c) ablation chamber

3.1. Mach-Zehnder interferometer

A schematic diagram of the MZI and the complete experimental setup has been shown in Figure 3.2. The schematic diagram has been explained in the following paragraph. The schematic diagram clearly shows the major components of the MZI, and they are the mirrors, beam splitters, band pass filters and the spatial frequency filter. The details of these components have been discussed later in different subsections of this section.

As shown in Figure 3.2, mirrors M1 and M2 have been used for steering and for initial alignment of the laser beam. The original laser beam is close to 2 mm in diameter. A beam expander assembly (*Thorlabs*), comprising of lenses L-1 and L-2 with a pin hole (P) in between, has been used to expand the light beam. The distance between the aperture and the lens is adjustable. The expanded and diverging light beam, as it emerges from the variable aperture, has been collimated into a 20 mm diameter beam using a collimating lens (L2). This collimated beam now acts as the probe beam for the Mach Zehnder interferometer. The first beam splitter (BS-1) splits the light beam into the two arms of the interferometer; the test arm (BS-1 to M-3 to BS-2), which houses the ablation cell and the reference arm (BS-1 to M-4 to BS-2). The optical components of the interferometer (e.g. beam splitters, mirrors (M-1 and M-2) etc. are of high optical grade (BK 7, Flatness: $\lambda/10$). The movable stop has been placed on the reference arm so as to enable the same system to capture the shadowgraph images. When the stop is ON, the light from the reference arm does not reach the beam splitter BS-2 and therefore the interference does not take place. In this case, the only beam available is the beam through the sample arm, which is used for capturing the shadowgraph of the ablation process. When the stop is removed the interference occurs and the interferograms are recorded. The laser ablation setup has been discussed separately in the next section.

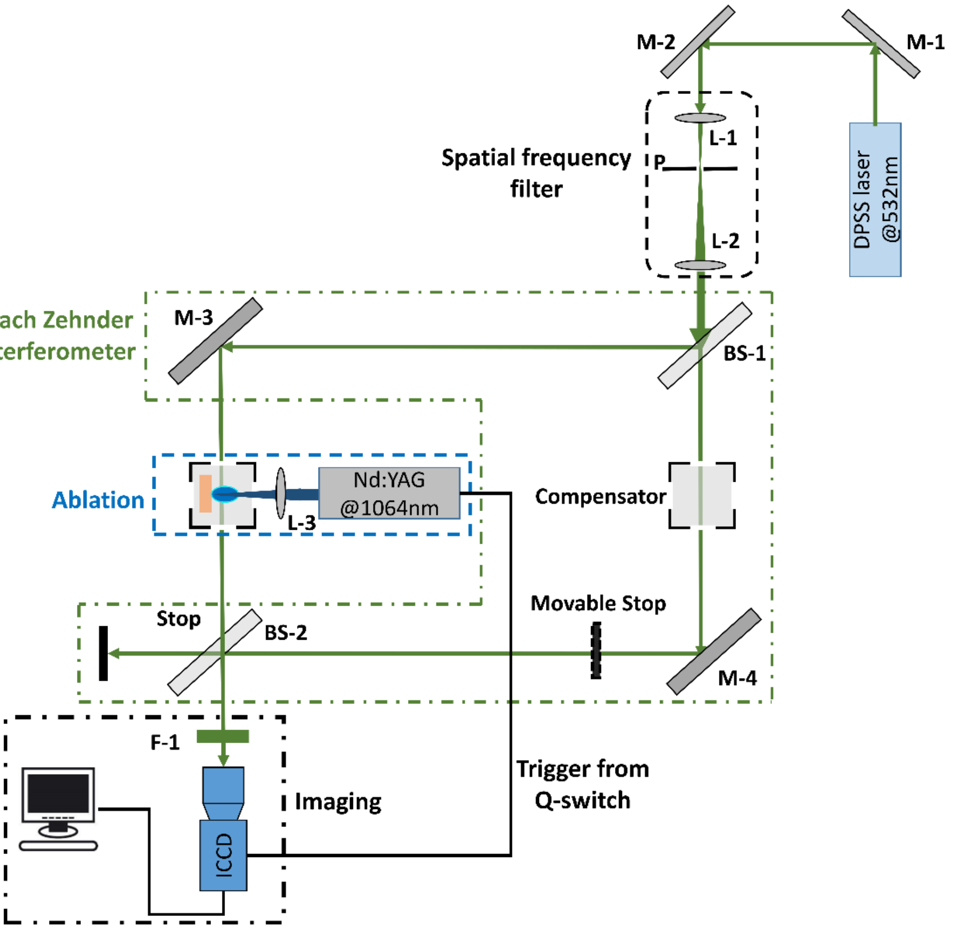

Figure 3.2: Schematic drawing of the complete experimental set-up employed for the ablation study.

3.1.1 He-Ne laser

He-Ne Laser (Research Electro-Optic Inc.) was used for setting up the MZI. The beam was having horizontal polarization with 35mW power and 632.8nm wavelength. The laser was highly stable with excellent pointing stability. This laser was used to observe the shock phenomena in air ambient. The specifications relevant from the point of view of the experiment have been tabulated below.

3.1.2 Diode pumped solid state (DPSS) laser

A diode pumped solid state laser (Verdi V-5 from Coherent Inc.) with central wavelength 532nm has been used for MZI with liquid media. The laser was operated at output power of 200 mW and 20% of the output power was used for the experiment. The parameters that are crucial from the point of view of our experiments have been listed in Table 3.2.

Table 3.1: Specifications of He: Ne Laser

Output power (max)	35 mW
Wavelength	633 nm
Spot size	1.22 mm (± 10%)
Beam divergence	< 0.66 mrad
Mode	TEM_{00} (>99%)
Noise (30 Hz – 10 MHz)	< 1% RMS
Polarisation	Linear (>500:1)
Longitudinal mode spacing	163 MHz
Long term beam drift	< 0.05 mrad

Table 3.2: Specifications of Coherent Verdi V-5

Output power (max)	5 W
Wavelength	532 nm
Spot size	2.25 mm (± 10%)
Beam divergence	< 0.5 mrad
Power stability	± 1%
Noise	< 0.02% RMS
Polarisation	Vertical (> 100:1)
Linewidth	< 5 MHz RMS
Pointing stability	< 2 µrad/^{0}C

3.1.3 Optical components

Apart from the above mentioned instruments, optical elements like mirrors and line – filters were used for the purpose of experimentation. For 532 nm probe laser the mirrors used were BB2-E02 (THORLABS) with surface quality of λ/10. The other important details have been given in Table 3.3.

Table 3.3: Specifications of broadband mirrors

Material	Fused silica
Flatness	λ/10
Quality	10-5 scratch-dig
Parallelism	≤ 3 arcmin
Clear aperture	> 85%
Reflectance	> 98% at 45^0 angle of incidence @ 532 nm

The mirrors used for manoeuvring the Nd: YAG laser beam (@1064 nm) were NB1-K12 procured from THORLBS. These mirrors were coated such that they have high reflectivity at 1064 nm (~ 99%) and 532 nm (> 98%). These have high damage threshold of 5 J/cm^2 and 8 J/cm^2 at 1064 nm and 532 nm, respectively for 10 Hz repetition rate and 10 ns duration pulses. The laser-ablation of metal target results in the formation of plasma plume which has emissions ranging over a very broad range of spectrum (including the entire visible spectrum). To avoid stray radiation falling on the camera and degradation of the image quality a band pass filters were used which were centred at 632.8 nm and 532 nm and had a linewidth of 1 nm ± 0.2 nm. The filters used for 632.8 nm and 532 nm were FL632.8-1 and FL532-1, respectively. Both the filters were procured from THORLABS. The two filters FL632.8-1 and FL532-1 have transmission wavelength centred at 632.8±0.2 nm and 532±0.2 nm, respectively and have a transmission of 50% and 40% respectively.

3.2. Laser ablation setup

The ablation setup has been shown schematically in Figure 3.3. The major components of the setup have been labelled. The picture of the real setup with focussing lens and stage has been shown in Figure 3.1b. The setup has been briefly described in the following paragraph. The description of mirrors has already been given in the preceding section.

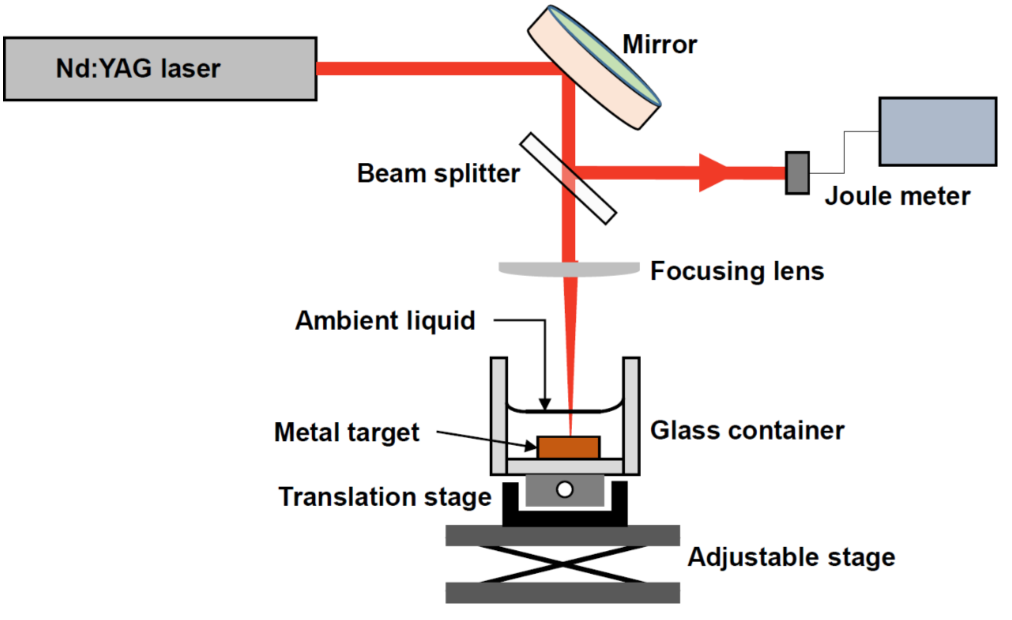

Figure 3.3: Schematic diagram of the laser ablation setup

The fundamental wavelength (1064 nm) of Nd: YAG laser (Quantel Q-smart 850), with a pulse duration of 6 ns has been used as the ablation beam. The ablation beam has been focused using a plano-convex lens (f = 175 mm) and is made to hit the target surface at normal incidence. The laser fluence that have been set for different experiments have been appropriately mentioned in Section 3.5. A small fraction of the beam was split and let to fall on an optical energy meter to ensure that the laser fluence is constant during the course of the experiments. The crucial components of the setup have been described as subsections of this section.

3.2.1 Ablation chamber

Two identical ablation chambers were made. Each of them was made up of BK-7 glass of flatness λ/10. The thickness of the glass is 5mm and the dimensions of the chamber are 50 mm × 50 mm × 60 mm. The glass chamber has been shown in Figure 3.1c. The parallelism is ≤ 5 arcmin. The size of the chamber has been so chosen to avoid any effect of the reflected shock (back from the walls of the container) in the field of view, over the period of observation. In case the dimension of the chamber had been smaller the reflected shock would have been seen within the interval of a few microseconds starting from the time of ablation. Also, this bigger size ensures that a 10 mm water height will be enough volume to ensure that there will not be appreciable change in the density of the medium due to the release of a few micrograms of nanoparticles. This enabled us to perform the experiments of ablation in liquid for 20-25 shots without changing the liquid.

3.2.2 Nd: YAG Laser

Quantel (Q-smart 850) Nd: YAG laser was used for the purpose of ablation. It has a repetition rate of 10 Hz and peak energy 800mJ with 5ns pulse width (FWHM). It was used to ablate the Cu and Ti metal plate kept in chamber filled with water. In the present experiments the laser was operated in single shot mode. The delay between the Q-switch trigger pulse and flash lamp output was used for controlling the laser energy. The laser source has the facility to generate 2nd and 3rd harmonics wavelength i.e. 532nm and 355 nm. The specifications that were of importance from the point of view pf our experiments have been given in Table 3.4 (*http://www.quantel-laser.com/en/products/item/q-smart-850-mj-.html*). All of these have been measured at 1064 nm.

Table 3.4: Specifications of Quantel Q-smart 850 (Nd:YAG laser)

10 Hz	
Pulsed energy (max)	850 mJ
Energy stability	± 2%
Power drift	± 3%
Pulse duration	6 ns
Pointing stability	< 40 μrad
Jitter	± 0.5 ns
Fucusability	≤ 2 times the diffraction limit
Linewidth	≤ 0.7 cm^{-1}
Divergence	< 0.5 mrad

Polarisation	Horizontal (> 80%)

3.3. Intensified Charge-Coupled Device (ICCD) Camera

The laser produced plasma and its associated phenomenon is highly transient in nature. The laser induced phenomena, like plasma formation, shockwave propagation and cavity expansion take place over the time scale of nanoseconds to micro seconds. Therefore, for the time resolved study of the above phenomena, very fast time response is needed to record the experimental data. Intensified charge couple devices (ICCD) are capable to record and analyse ultra-fast events with very high accuracy. ICCD camera consists of three major parts, image intensifier, coupling lenses and CCD chip. Coupling or imaging lens of the camera is an assembly of optical lenses used to collect the light and make images of objects on CCD. Charge coupled device (CCD) chip is used to store or record the images. It is an integrated circuit made onto a silicon surface forming light sensitive elements called pixels. Photons incident on this surface generate charge that can be read by electronics and turned into a digital copy of the light patterns falling on the device. Image intensifier is most important component of ICCD and its brief description are given below.

3.3.1 The image intensifier

The image intensifier is the most crucial system component of an intensified CCD high speed camera. The main function of the image intensifier is the multiplication of the incident photons, i.e. the amplification of the light signal. This enables the ICCD camera to take images at extremely low light conditions and/or at extremely short exposure times in nanoseconds order, when the integral of the photon flux over the exposure time is very small. The image intensifier is built with three independent components, namely, photocathode, multi-channel plate and phosphor screen.

Photocathode: The light signal incident on the photocathode of the image intensifier. The photocathode converts the incoming photons to photo electrons. The specific material composition of the photocathode enables to cover different spectral ranges. Multiple photo cathodes cover the spectral range from UV, VIS to IR. The photocathode sensitivity is one of the important properties of ICCD camera to choose the most suiting photocathode according to the application.

Multi-channel plate[1]: Multi-Channel Plate multiplies the incoming electrons from the photocathode. A multi-channel plate is made from highly resistive material having regular array of small tube, known as multi-channels. Each multi-channel acts as continuous-dynode which multiplies the incident electrons under the presence of a strong electric field. The typical multiplication factor of a double MCP is 10^6. The schematic diagram has been shown

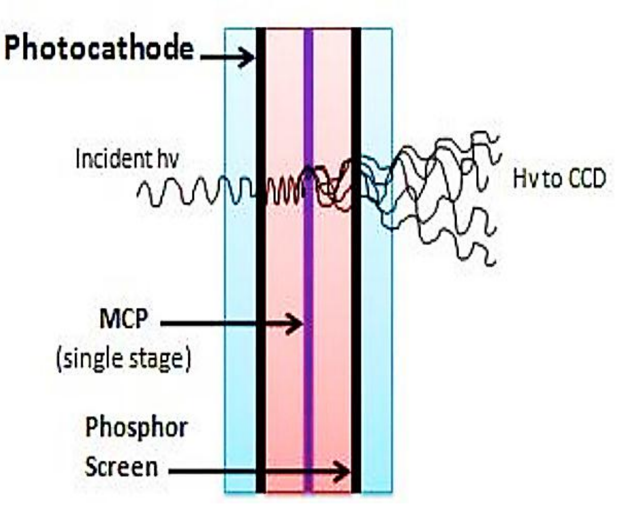

Figure 3.4: Schematic diagram of the process of photon multiplication in ICCD

in Figure 3.4[2].

Phosphor screen[3]: The phosphor screen emits photons as the accelerated electrons hit the material. The phosphor screen of image intensifiers converts the electron avalanche from the micro channel plate back into photons. Typical conversion factors of the used phosphor screens are between 20 and 200 photons per electron, depending on the phosphor type and the kinetic energy of the electrons, i.e. the acceleration voltage. In order to increase the number of photons emitted in the direction towards the CCD sensor, the backside of the phosphor is coated with an aluminium layer that reflects photons towards the proper direction, as shown in the enlarged detail in Figure 3.5[4].

[1] http://stanfordcomputeroptics.com/technology/image-intensifier/multi-channel-plate.html
[2] The image has been taken from the webpage of Stanford Computer Optics Inc.
[3] http://stanfordcomputeroptics.com/technology/image-intensifier/phosphor-screen.html
[4] The image has been taken from the webpage of Stanford Computer Optics Inc.

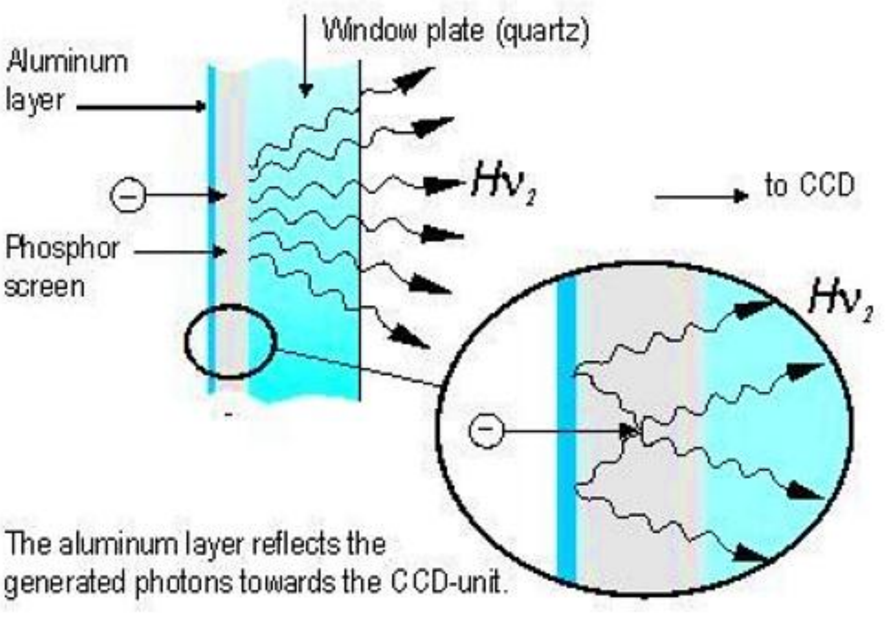

Figure 3.5: Schematic diagram of phosphor screen

3.3.2 Fast gating system[5]

The principle of high speed gating has been shown schematically in Figure 3.6[6]. There are three voltages applied to the image intensifier as shown in the drawing. The voltage between photocathode and multi-channel plate enables gating operation of the image intensifier. If the voltage between photocathode and multichannel plate is negative, the photoelectrons from the photocathode are accelerated towards the multi-channel plate. This means that the shutter is open. If the voltage is positive, the photoelectrons are kept at the

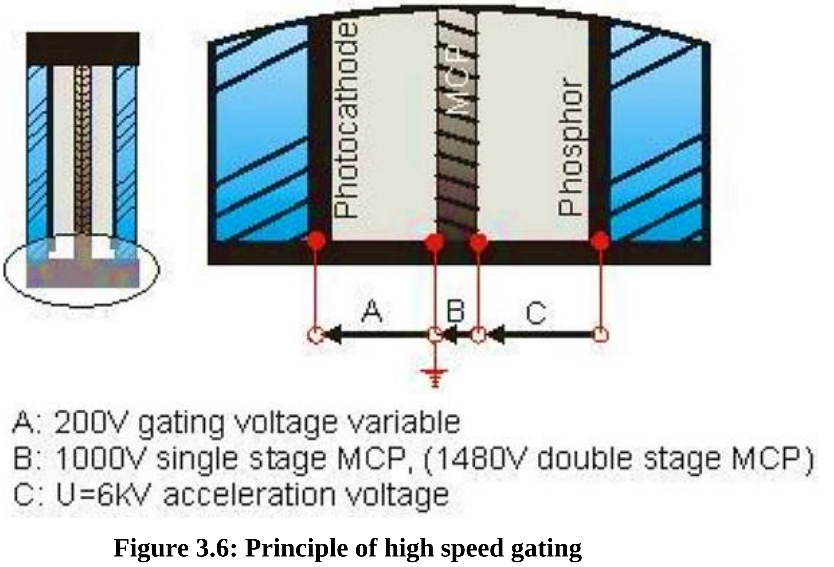

Figure 3.6: Principle of high speed gating

[5] http://stanfordcomputeroptics.com/technology/image-intensifier.html
[6] The image has been taken from the webpage of Stanford Computer Optics Inc.

photocathode, thus the shutter is closed. This operation mode of the image intensifier is called gated mode and the voltage is called gating voltage.

A unique advantage of the gated ICCD camera over all other kinds of cameras is its ability of ultrafast gating. Shutter speeds with exposure times of the order of few nanoseconds (ns) are possible and are mostly used in the laser produced plasma experiments. In the present experiment, an intensified charge coupled device (ICCD) camera (4Picos, Stanford Computer Optics, Inc.) having variable gain and gate width is used to record the images shock and cavitation bubble. This ICCD offers gating times of down to 200 picoseconds (ps). The specific values of the parameters that were used for our experiments have been mentioned in the subsequent chapters appropriately.

3.4. Target material

Target material has a very crucial role to play in the set of experiments that are being discussed in this thesis. Apart from the purity and surface quality of the material, the geometry is also important. Along with the flat (open) target plates, two other geometries of the target have also been taken into consideration. The schematic diagram of the target plates have been shown in Figure 3.7. In one of the cases two aluminium walls have been fitted on either side of the ablation spot and in the other case an aluminium plate was set above the target in a way that it was parallel to the top surface of the target. The targets materials used for the experiments were 99.9% pure copper and titanium plates.

For each set of experiments, the target was thoroughly washed with acetone and rinsed with DI water to avoid any impurity due to the target surface contamination. Also, it was made sure that target surface was properly polished and flattened by mechanical means to avoid any errors that may arise due to the macroscopic surface irregularities. The target plates were mounted on a precision linear translation stage so that the target plates can be moved after every few shots to avoid any anomaly arising due to the formation of crater on the surface because of repeated ablation on a single site. Apart from these, there were specific details related to each set of experiments that were performed in different ambient (air/liquid) that are being discussed in the next section.

3.5 Experimental methodology

Three different experiments have been performed and are being included in this thesis. The experiments were designed and conducted to observe the shockwave generation, propagation and reflection (only in the experiment with physical boundaries) in air/liquid ambient and to investigate the presence of physical boundaries (that result in the reflected shockwave) on the size of the nanoparticles produced due to ablation. The following subsections deal with the means and methods that were resorted to for conducting these experiments. The experiments related to observation of shockwaves employed MZI as the diagnostic tool whereas in case of nanoparticle production, the characterisation was done using scanning electron microscopy (SEM). The ablation setup and the MZI have been discussed in the previous sections of this chapter and therefore only the details of the target material, target geometry and experiment-specific parameters are being presented here.

3.5.1 Ablation in air ambient to observe shockwave propagation and its effects

The ablation was carried out on 99.9% pure copper targets with the fundamental wavelength (1064 nm) of an Nd: YAG laser. The laser beam was focussed to a spot-size of 0.5mm on the target surface. All the experiments were performed keeping the laser fluence constant at 19J/cm^2. The ablation laser was set in a way that the beam hit the target surface at right angle. The schematic drawing of the target plates have been shown in Figure 3.7. For the purpose of observation of shock in open i.e. without any confinement, the target was placed as shown in Figure 3.7a. However, for studies on the effect of lateral and longitudinal confinement vertical walls and top plate were used in conjunction with the target. Figures 3.7b and 3.7c show the arrangements made to observe the effect of lateral and longitudinal confinement of shock in the medium, respectively. The walls and top plate were made up of aluminium sheets (1mm thickness). A hole was drilled at the center of the top plate (Figure 3.7c), which was big enough to let the laser beam pass through it (5mm), to observe the vertical confinement. The separation between the walls in case of lateral confinement is 13.5mm and the height of the top plate with respect to the target surface is 10mm.

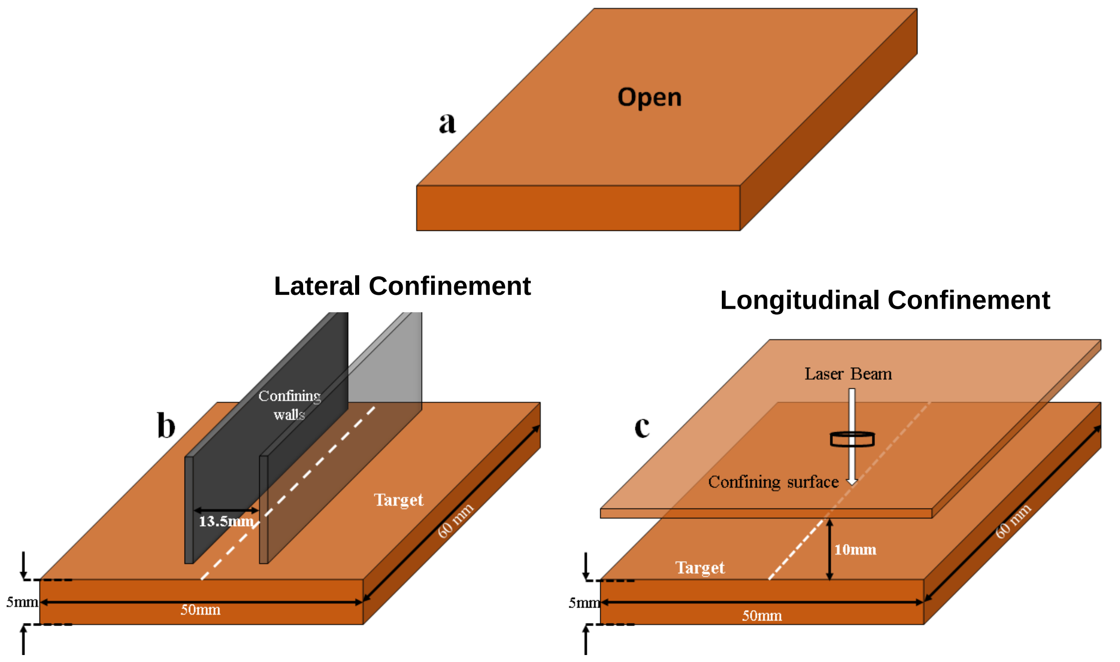

Figure 3.7: (a) Plane target (b) target with vertical walls (for lateral confinement of shock) and (c) target with horizontal confinement (top) plate (for longitudinal confinement of shock)

The targets were mounted on precision linear translation stages (20µm/rotation) to ensure smooth movement. The target was shifted after every shot to ensure that a new point is available for ablation and the effects of crater are not there. Also, in case of lateral confinement the ablation point was made to lie equidistant from the two walls.

Here the Mach Zehnder interferometer (MZI) was set up using a He-Ne laser (Research Electro-Optic Inc.) operating at 632.8 nm, as has been discussed in Section 3.1.1. The beam was expanded and the noise was filtered using a spatial frequency filtering assembly coupled with a beam expander setup. The final diameter of the collimated beam that was used for interferometry was 25 mm. The fringe-shifts occurring due to the perturbation in the medium due to the propagation of the shock wave resulting from ablation of metal was recorded using a fast gated ICCD camera (4 picos from Stanford Computer Optics Inc.). It was synchronized with the laser Q-switch output and desired time delay was generated using the in-built mechanism of the camera. The exposure was set to 100ns[7]. The camera was interfaced with a PC using a frame-grabber card. The proprietary software provided by the Stanford Computer Optics Inc. was used to operate the camera and record the images. A calibration of the ICCD was needed to correlate pixels with real physical

[7] Here, it is important to mention that for the process of observation of laser plume or charge dynamics desired integration time is of the order of a few ns. However, in our case the processes that have been observed (shock propagation) occur over a time scale of µs, and hence, an integration time of 100 ns gives good accuracy.

dimension, which was done by a grid of known dimension. As discussed above a movable stop has been placed on the reference arm of the MZI, so that the reference beam could be blocked as and when needed so as to perform shadowgraphy with only the beam passing through the sample on.

3.5.2 Ablation in liquid ambient to observe shockwave propagation and its effects

Ablation of a copper target (99.9% purity), mechanically polished and chemically cleaned, was performed by the fundamental (1064nm) of an Nd: YAG laser (Quantel Q-smart 850) with a pulse duration of 6 ns[8]. The spot size was maintained at 0.5mm at the target surface. Laser fluence was set to 11 J/cm^2 and ablation was performed in a cubical glass chamber (with open top), the walls of which are made up of optical quality glass (BK7) with surface flatness of the order of $\lambda/10$. All the experiments were set-up with target immersed in liquid and the height of the liquid column was maintained constant at 25mm. To perform ablation in different liquid media, ethylene glycol (reagent grade) was used in different proportions with DI water to achieve 25% and 50% ethylene glycol aqueous solutions (w/w). It is worth mentioning here that, in general, the phenomenon of laser ablation in liquids (LAL) produces nanoparticles, which in turn may lead to an increase in the density of the liquid medium after a relatively large number of ablation shots. However, in the present work, the possible influence of this effect has been taken care of by using an ablation cell of sufficiently large dimensions (50 mm × 50 mm × 60 mm) with the liquid column height of at least 25 mm in the experiments, thereby avoiding any significant changes in the concentration of the liquid medium due to a single shot. Furthermore, fresh liquid after every twenty shots has been used in the experiments, which also ensures that there is no significant accumulation of nanoparticles in the liquid medium.

A chamber (indicated as compensator in the figure) of the same dimensions and material as the ablation chamber and containing the same quantity of experimental liquid has been used as a compensator to equate the optical path lengths of the two arms of the interferometer under reference conditions. The MZI here was illuminated with a 532 nm laser beam from a DPSS laser as discussed in Section 3.1.2. The laser power reaching the beam

[8]It is to be mentioned here that the visible range of wavelength could have also been employed in the experiments. However, the present set of experiments make use of the fundamental wavelength (1064 nm) for ensuring sufficiently high power density after accounting for the losses due to attenuation through the medium. This becomes important as the primary focus of the present study is to investigate the effect of shock propagation in media of different densities. In this context, the application of fundamental wavelength (1064 nm) ensures enough power density to clearly observe the effects of the propagating shock waves in the given liquid medium.

splitter BS-1 was set to 40 mW. The beam size was fixed at 20 mm by putting a beam expander and spatial frequency filter.The shift in the fringes that occurred due to the changes in RI resulting from the propagation of shock, was recorded using a fast gated ICCD camera (4picos from Stanford Computer Optics Inc.) with an integration time of 25 ns[9]. An interference-based line filter F-1 (centered at 532±0.2 nm with a linewidth of 1nm) has been placed before the camera to allow only the 532 nm beam to pass through it. The ICCD camera has been synchronised with the laser Q-switched output, and the in-built timing generator of the camera has been used to generate the required time delay. The exposure was set equal to 25ns. The camera has been interfaced with PC using the proprietary frame grabber software provided by Stanford Computer Optics Inc. The ICCD has been calibrated using a grid of known dimension to correlate the pixel size with real physical dimensions in the field of view. A movable stop has been placed in the reference arm of the MZI, so as to let the only beam passing through the sample arm fall on the ICCD to record the shadowgraph images.

3.5.3 Investigation of the effects of physical boundary on the size of nanoparticles

The effects of the reflection of laser produced plasma-induced shockwave (due to the presence of physical boundary) on the medium density and the plume lifetime has been thoroughly investigated by conducting experiments in the air ambient. In this experiment the focus is on studying the effects of the presence of physical boundaries on either side of the ablation site on the size and size distribution of the nanoparticles that were formed due to the process of LAL. To understand the effect of the confining boundaries, four sets of experiments have been performed. In this direction, two different target materials and two different ambient liquids were chosen. Water and isopropyl alcohol (IPA) have been chosen as the ambient liquids. The reason for selection of IPA and water as the two liquid media has been based on the fact that their viscosities and densities are significantly different from each other and hence significant contrast in the effect of confinement may be expected. At the same time, the refractive indices of the two liquids differ slightly and hence the transmission and reflection from the liquid target interface do not differ significantly for a chosen target material. It enables us to assume that the laser fluence is constant for a specific target material

[9]While the pulse duration of the laser employed for ablation is 6 ns, the shock wave phenomenon has been observed over a time scale of microseconds. In this arrangement, the camera observes just one instant of shock and treats it as static over the integration time. As would be discussed in the subsequent sections, the shock wave propagation has been interpreted in the form of propagation of the deformation of the interference fringe patterns in the field of view. Thus, the fringe deformation has been observed at much later time instants after the pulse has died out.

in different ambient fluids. Two sets of experiments have been performed with copper and titanium targets (with and without confining walls) in water ambient and two other sets of experiments have been performed with the same targets but with IPA as the ambient medium. In each case, the height of the liquid column was maintained at 10 mm with reference to the top surface of the target surface. Ablation of the target surface has been achieved by firing the laser beam at 5Hz for 30 minutes (9000 shots). The laser fluence was maintained at 11 J/cm^2. This time interval has been chosen so as to make sure that there are not too many nanoparticles in the suspension so as to avoid any possibility of agglomeration. On the other hand, the number is high enough that is required for characterizing the produced particles for size distribution using SEM.

Copper and titanium plates (99.9% purity) with dimensions of 25 mm × 25 mm × 2 mm have been used as the target plates. Before the start of the experiments, the surfaces of the target plates were polished and thoroughly rinsed in acetone to avoid impurities due to oxide formation. Two different target geometries have been used for both the target materials. The schematics of these two configurations of target plates have earlier been shown in Figure 3.7 (a) and 3.7(b). It is important to mention here that, the separation between the walls in case of air based experiments was 13.5 mm, whereas in case of liquid based experiments the separation was 10 mm. The ablation was carried out in such a way that the point of ablation remains equidistant from both the confining walls. The Al walls were put on the target surface to reflect back the laser-induced shockwaves towards the ablation site (plasma plume). The effects of placing these barriers have been discussed in Chapter 5 (Section 5.3).

The LAL experiments have been performed in a custom made glass cuvette with open top, as discussed in Section 3.2.1. The chosen dimensions of the cuvette made sure that the total time that the shock waves (generated due to the ablation of the metal) take in travelling from the point of ablation to the walls of the container and back again to the ablation point (after getting reflected from the container walls) is significantly greater than the thermalisation time of the plasma produced during the process. This condition needs to be satisfied to avoid any plausible effect(s) of the reflected shockwave on the plasma plume, with the flat plate target geometry, i.e. in the case where there are no ablation boundaries. If this condition is not met, *viz*. in the case of a smaller-sized container, then the reflected shockwave will affect the process of thermalisation of the plasma. Hence, the process of formation of nanoparticles will get influenced and one will not be able to achieve what may be termed as LAL of a flat target without any confinement. The ablation chamber has been kept on a translation stage (20 μm precision) for the previously discussed reasons.

Chapter 4: Data Reduction

4.1 Analysis of interferograms

An interferometer uses two coherent beams of light travelling in two sections namely, reference and the object sections which interfere with each other causing alternating bands of constructive and destructive interference patterns called as fringe patterns. The light travelling in the object section passes through the object which has a different phase details than the reference section. Since the fringe patterns are formed as a result of the path integrated phase produced by the light travelling in the object beam it contains the path integrated data of the physical phenomenon inside the object namely changes in mass density, charge density etc. Each of the constructive (bright) or destructive (dark) bands present in the Interferogram represents the locus of constant phase difference. Mathematically the alternating dark and bright fringes in the interferogram can be represented by the following relation,

$$I(x,y) = A(x,y) + B(x,y)\cos[2\pi\vec{f}\vec{r} + \Delta\varphi(x,y,t)] \tag{4.1}$$

A wavelet is a specifically designed pulse function used to analyse the signal locally. A complex 2D mother wavelet is assumed with which a family of wavelet in the shape of the mother wavelet is produced by dilation, translation as well as rotation of the mother wavelet. By definition a Morlet wavelet is a plain wave modulated by a Gaussian function,

$$\Psi(x) = e^{i\omega_0 x} e^{\left(\frac{-1}{2\sigma^2}|x|^2\right)} \tag{4.2}$$

Here ω_0 is the amplitude factor and σ is the half width at half maxima of the Gaussian wave. A family of wavelets is produced by performing various operations on the mother wavelet. These Operations are governed by the parameters namely, scales (dilation parameter) and angles (rotation parameter). For optimum processing speed, the scales and angles are determined by the relations that are described in the J. Ma et al. such that it satisfies the admissibility condition [130–132]. For our analysis we used $\sigma = 0.5$ and $\omega_0 = 5.336$ such a way that admissibility condition is satisfied. Discrete angles and scales are calculated by the relation shown in Equation 4.3. After applying the continuous wavelet transform, using the set of wavelet coefficients an angle map describing local orientation of the fringes and scale map describing the scales of the fringes has to be constructed. A ridge detection scheme described in Equation 4.4 is used to determine the angle map and the scale map. The phase at the ridges can be retrieved by Equation 4.5. Since cosines are positive in both the first and the fourth quadrant, a sign ambiguity is inherent in the calculation of the wrapped phase directly from the ridge detection for a complex interferogram. To counter the sign ambiguity, the wavelet analysis is carried out for discrete angles in $\theta \in [0, \pi]$.

$$\Delta\theta = 2\sin^{-1}\frac{\sqrt{2}}{4\pi\sigma},$$
$$s_i = q^{i-1}s_l,\ s_l = \lambda_l\left(1+\frac{\sqrt{2}}{4\pi\sigma}\right),\ q = \frac{2\pi+\frac{\sqrt{2}}{2\sigma}}{2\pi-\frac{\sqrt{2}}{2\sigma}} \tag{4.3}$$

$$W(x,y)_{ridge} = W(\theta_{ridge}, s_{ridge}, x, y),$$
$$Where,\ (\theta_{ridge}, s_{ridge}) = argmax\{|W(x,y)|\}\ \forall\ \theta \in [0,\pi), s \in S \tag{4.4}$$

$$\varphi = \tan^{-1}\frac{imag(W(x,y)_{ridge})}{real(W(x,y)_{ridge})} \tag{4.5}$$

Analysis of complex fringe pattern also requires a sign determination procedure for the determination of the sign of the wrapped phase. A 2D wavelet analysis uses the continuity in the orientation of the fringes to determine the sign of the wrapped phase. To determine the continuity in the orientation angle the direct difference in the angle between 2 adjacent pixels taken and the continuity is checked. The correction scheme for both the correction in the angle as well the phase is given by Equation 4.6.

$$[\theta_i, \varphi_i] = \begin{cases} (\theta_i, \varphi_i), & if\ |\Delta\theta - \pi| > \Delta\theta \\ (\theta_i, \varphi_i), & if\ |\Delta\theta - \pi| > |\Delta\theta - 2\pi| \\ (\theta_i + \pi, 2\pi - \varphi_i), & else \end{cases} \tag{4.6}$$

Where, $\Delta\theta = \theta_i - \theta_{i-1}$

For efficient determination of sign, a pixel scanning strategy which uses the magnitude of the ridges found as the relaiblity/quality map is used. Before finding the unwrapped phase values using quality guided unwrapping, a windowed fourier filter is used to remove the local discontinuities and smooth the local variations [133–135]. The pixel by pixel phase difference obtained is predominantly because of the path difference produced by the refractive index changes in the object. Since the observed plasma plumes are axisymmetric in nature the path the light beam travels along each cross section of the image is found to be varying starting from 2R (axisymmetric central line) to 0 (periphery of the plume) where 'R' is the maximum radial extent of plume. The estimation of the refractive index map in such cases of varying path length requires the use of Abel inversion and the relation between the refractive index and the phase difference between the two arms of the interferometer for the case of axisymmeteric field is given by Equation 4.7.

$$n(r,y) - n_\infty = \frac{-\lambda}{2\pi^2}\left(\int_r^\infty \frac{d\Delta\varphi(x,y)}{dx}(x^2 - r^2)^{-\frac{1}{2}}dx\right) \tag{4.7}$$

Abel inversion when applied on to the projected path difference determined from the obtained phase shift as reconstructed from the recorded interferometeric images provides a direct estimate of the refractive index map. The Abel inversion of the data set has been realized using modified fourier hankel algorithm and the discritized version of the algorithm is given by Equation 4.8 [136]. The modified fourier hankel algorithm has an inherent advantage over other abel inversion algorithms as it eliminates the discontinuity at the axisymmetric central axis. It also enables the smoothening of noisy data. For the case of the analysis of the interferogram obtained experimentally, the smoothening parameter $\alpha = 0.1$ and the interpolation paramter $\eta = 0.001$ is fixed.

$$n - n_\infty = \frac{\alpha^2\pi}{2NR}\sum_{j=-\frac{N}{2}}^{\frac{N}{2}} \varepsilon(x_j) \sum_{k=1}^{k=[\frac{N\eta}{\alpha}]} kJ_0\left(\frac{\alpha ik\pi}{N}\right)\cos\left(\frac{\alpha jk\pi}{N}\right) \tag{4.8}$$

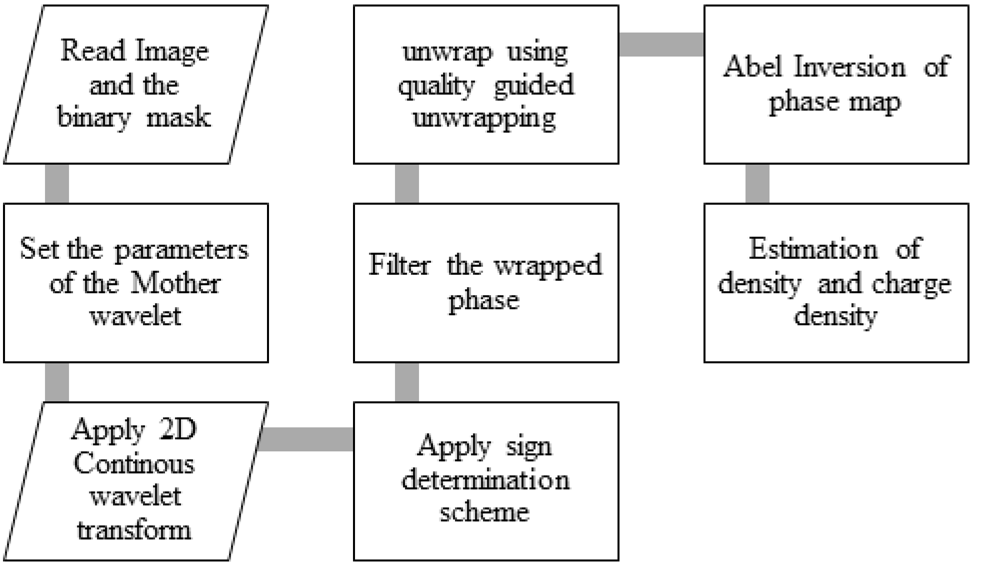

Figure 4.1: Description of the algorithm for analysis of complex interferogram using 2D continuous wavelet transform

4.2 Analysis of synthetic data with various noise levels

This section describes the effect of increasing noise levels and relative insensitivity of the analysis algorithm employed for demodulation of the noisy synthetic interferograms. The effect of noise on the demodulation is quantified by using root mean square (RMS) error (ϵ) of the obtained phase distribution.

$$\Delta\varphi(x,y) = ae^{\frac{(x-x')^2+(y-y')^2}{b^2}} \tag{4.9}$$

A MATLAB based code has been developed and tested on synthetic data which is generated by using a Gaussian phase distribution as shown by Equation 4.9. Various levels of noise have been added to the interferograms and the obtained interferograms are shown in Figure 4.2. It can be seen that increasing noise level in the interferogram reduces the contrast between the fringes and the background due to which the distinguishing features (sinusoidal variation in the fringe intensity) are lost. This analysis not only provides the estimate of the error for various noise level also it tests the ability of the continuous wavelet analysis for low contrast fringes. The demodulated fringes are filtered using 2D windowed Fourier filter to

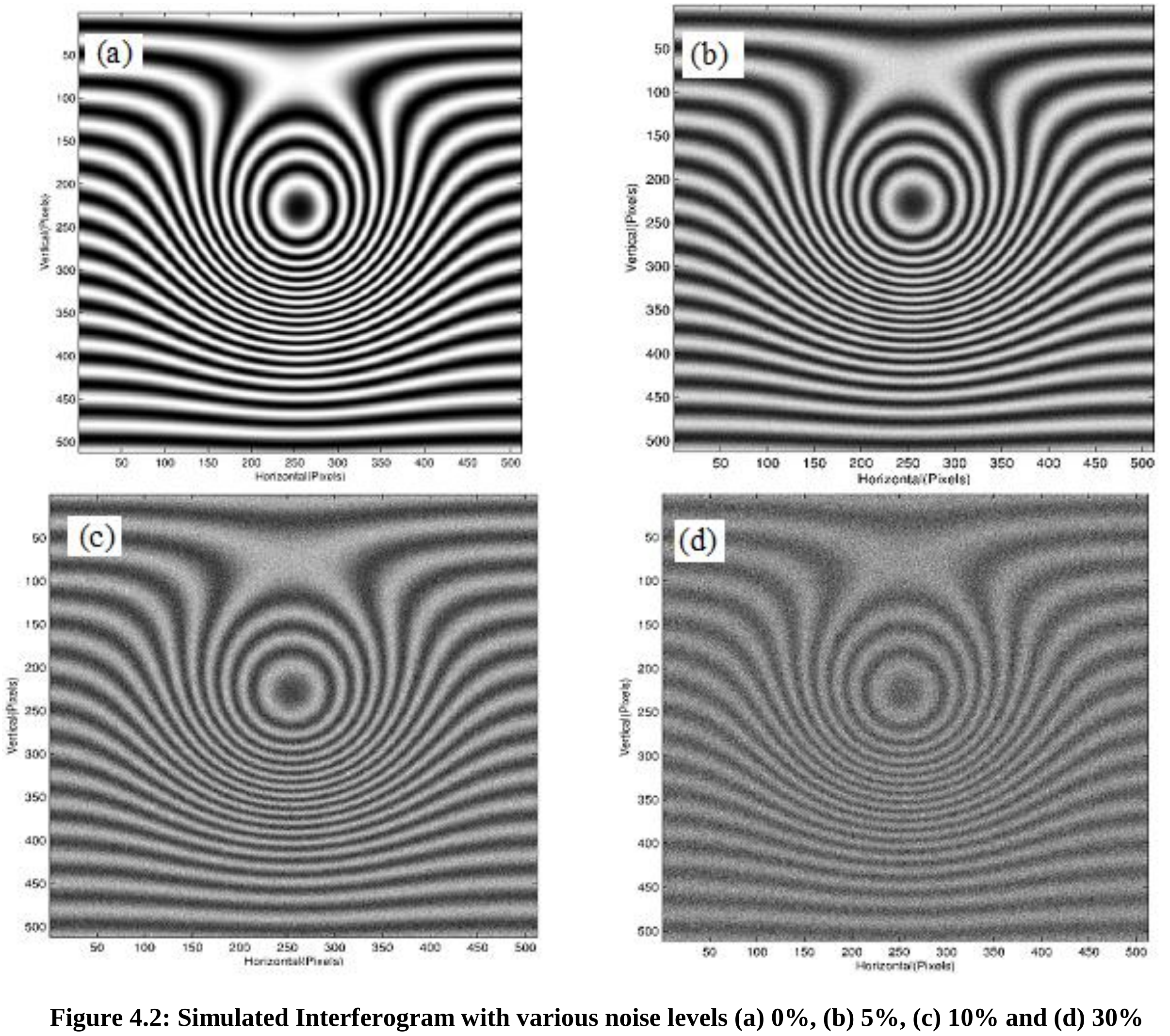

Figure 4.2: Simulated Interferogram with various noise levels (a) 0%, (b) 5%, (c) 10% and (d) 30%

remove the local breaks in the fringes.

Figure 4.3 shows the effect of WFF on the wrapped phase produced after sign determination. As we can see, the presence of local discontinuities near saddle point creates local discontinuities in the determination of sign. These local discontinuities are filtered and the filtered wrapped phase map is produced. After filtering the wrapped phase map is unwrapped using quality guided phase unwrapping with the quality normalized interferogram as the quality. The RMS error is calculated for the simulated data using the unwrapped phase map and the actual Gaussian phase map using the relation given by equation (4.10),

$$\epsilon = \sqrt{\frac{\sum_{i=0}^{n}(\varphi^2 - \varphi_a^2)}{n}} \tag{4.10}$$

Where, ε is RMS error, φ is the unwrapped phase values and φ_a is the actual phase in the interferogram.

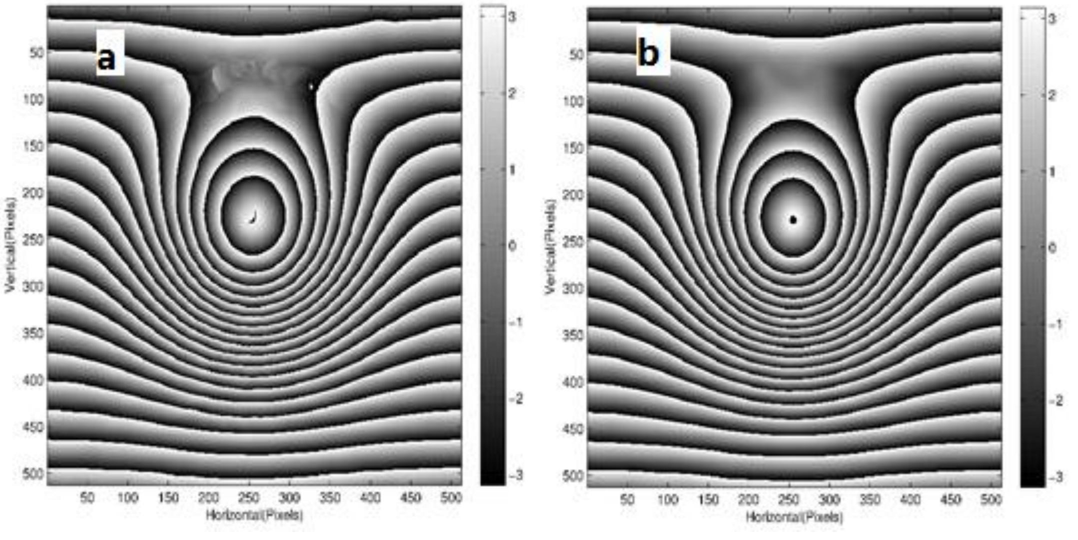

Figure 4.3: Effect of filtering on wrapped phase for 30% Noise level. (a) unfiltered and (b) filtered wrapped phase

Table 4.1 illustrates the insensitivity of the 2D wavelet analysis to noise clearly. As we can see the increase in noise level although affects the actual wrapped phase calculation, the tandem use of 2D windowed Fourier filter along with the 2D continuous wavelet analysis makes the unwrapping more accurate by filtering out the unwanted breaks near the saddle point in the wavelet analysis. This gives a more accurate and continuous wrapped phase calculation which reduces the error in the calculation of unwrapped phase map.

Table 4.1: RMS error for various Noise level between 2D CWT

Noise level (%)	RMS error
0	0.0069
5	0.0070
15	0.0072
30	0.0072

4.3 Retrieving the Refractive Index Values from the Interferograms

In view of the axi-symmetric nature of the shock wave generated due to laser ablation of the metal surface and the associated refractive index field, principles of Abel inversion have been employed for the reconstruction of the refractive index values from the phase distribution as estimated using the method described in the Section 4.1. The Abel inversion has been carried out using the modified Fourier-Hankel algorithm [136, 137]. Following this approach, the relative changes in the refractive indices can be mathematically expressed as;

$$n - n_{\infty} = \frac{-1}{\pi} \int_{r}^{r_0} \frac{d\left(\frac{\Delta\varphi\lambda}{2\pi}\right)}{dy} \frac{dy}{\sqrt{y^2 - r^2}} \qquad (4.11)$$

Here $\Delta\varphi$ is the spatial distribution of the phase differences as extracted from the recorded interferometric images, n_{∞} is the reference refractive index and λ is the wavelength of the coherent source employed in the present set of experiments (λ= 632.8 nm, He-Ne laser). Having determined the refractive index distribution, the medium density has then been estimated using the following relation;

$$\frac{n^2 - 1}{n^2 + 2} = \frac{\alpha\rho}{3} \qquad (4.12)$$

Here α is the molecular polarizability and ρ is the number density of the entities (atoms/molecules) constituting the medium. Further ρ is related to the mass density ρ_m by the relation[138, 139],

$$\rho_m = \frac{m}{N_A}\rho \qquad (4.13)$$

m is the molar mass and N_A is the Avogadro number

From Equations 4.12 and 4.13 we get a relation between $\rho_m$and the refractive index of the medium,

$$\rho_m = \frac{3m}{N_A \alpha} \frac{n^2 - 1}{n^2 + 2} \tag{4.14}$$

The same relation reduces to $n = 1 + C\rho_m$ in case of mediums that have RI close to 1, where C is a constant known as Gladstone-Dale constant and changes from one medium to another and with wavelength of light[140].

In case of the experiments performed in air ambient, the calculation of mass density from the RI data has been carried out using Equation 4.14. The value of molecular polarizability has been taken to be $\alpha = 2.118 \times 10^{-23} cm^3$as reported in the literature[141]. The density thus obtained and added to the background density of air at 30 degree C ($\rho_b = 1.16 \times 10^{-3} g/cm^3$) gives the true density of the medium. We have presented the effect of shock in terms of the ratio of this modified density to the background density (ρ_b).

In the case of the experiments that were conducted in liquid ambient, the density of the Ethylene Glycol (EG) has been taken from the standard data sheet available in the literature and the mass was calculated for 25% and 50%(w/w) aqueous solution.The density of the solutions with different proportions of EG was also calculated using this data. The densities for 25% and 50% (w/w) aqueous solutions of EG were found to be 1.0203 g/cm^3 and 1.0446 g/cm^3, respectively. The density of water is known to be 0.9971 g/cm^3 at STP. The RI data for different compositions of aqueous EG solution is available in literature [142]. Fogg *et. al.* reported that the variation of RI with mass fraction of EG in aqueous solution follows a linear trend. Thus, RI for the two concentrations of interest (25% w/w and 50% w/w) were obtained from the linear fit of the data reported by Fogg *et. al*. The estimated values of RI were 1.357793 and 1.382765, for 25% and 50% aqueous solutions of EG, respectively. The RI for water is known to be 1.3312. These RI data have been used for further calculations.

Equation 4.14 may be re-written as;

$$\alpha = \frac{3m}{N_A \rho_m} \frac{n^2 - 1}{n^2 + 2} \tag{4.14 a}$$

As α is not known for different concentrations of EG, it was first evaluated from Equation 4.14a for the known values of ρ_m and n for the different concentrations. The value of α thus obtained was used for calculating the mass density corresponding to the different values of n.

To calculate the charge density in the region having plasma we have used the relation [58],

$$n = 1 - \frac{e_0^2}{8\pi^2 \epsilon_0 m_e c^2} \lambda^2 N_e \tag{4.15}$$

Here, n is the refractive index, ϵ_0 is the permittivity of the free space, c is the speed of light in free space, m_e is the mass of an electron and e_0 is the electronic charge.

4.4 Errors and uncertainty analysis

Errors in any optical-based measurement technique, e.g. interferometry as employed in the present work, arise due to several factors which primarily include slight misalignment of the optical components, optical aberrations, noise generated at various stages of the experimental run time, quantitative analysis of the recorded optical images (e.g. estimation of phase values from the interferometric images) etc. Of all these factors, the errors associated with slight misalignment of the interferometric system have been minimized to the maximum possible extent by carefully aligning the two arms of the interferometer. In view of the fact that the experiments reported in the present work have been performed in wedge fringe setting mode of the interferometer, under reference conditions, it was ensured that the wedge fringes are reasonably straight and parallel to each other. While quantifying the interferometric images, the maximum error associated with phase estimation was estimated to be ≈ 5% and the error in shot-to-shot repeatability (due to the variation in laser power and minute changes in ambient temperature and humidity) was found to be close to ≈ 1%. Taking into account these individual errors, the maximum possible error in the estimation of the absolute values of mass density and electron density have been estimated to be ≈ 10.04% and ≈ 5.09% respectively. Further details of error analysis in the context of interferometry-based measurements may be seen elsewhere [136–138, 144, 145].

Chapter 5: Results and Discussion

In this chapter the focus is on drawing physically appreciable inferences from the refractive index (RI) maps obtained by analysing the recorded interferograms. The RI maps generated by processing the interferograms have been analysed to get the whole field mass density and charge (primarily electron) density in the field of view. Time evolution of the shockfront in the media of different densities have been studied and the effects of interaction of the shock with physical boundaries has been investigated. The implications of these investigations have been tested by performing experiments with different target materials and in different liquid media. A detailed discussions has been presented in the following sections.

5.1 Time resolved interferometry study of the plasma plume induced shockwave in confined geometry

The origin of shock in case of laser ablation with nanosecond laser pulses is well known and has been extensively explored in the past by various research groups. Both, theoretical models as well as experimental observations are well documented and widely available in the literature [54, 74]. The generation and propagation of the shockwave due to the expanding plasma plume has been studied and a detailed discussion on the effect of interaction of the shockwave with the physical barriers has been presented.

The interferometry images (interferograms) have been recorded to investigate the dynamics of the laser-plasma induced shockwaves in different geometrical configuration and their interaction with expanding plasma plume. In the present section detailed discussion has been done on the observations (interferograms). In order to quantify the present observations, refractive index (RI) maps have been generated by processing these interferograms and finally the change in RI with time has been converted into the electron density profile of the plasma and density perturbation of the medium (air). The discussions have been made under three sections; free propagation of shock in air, shockwave between laterally as well as vertically confining walls.

5.1.1. Free propagation of shock in air

The interaction of high power laser pulse with a metal target results in the formation of plasma consisting of neutrals, ions and electrons. Typically, in the case of 8 or 10ns pulse there are two phases – the first is for 2-3ns when the plasma is formed and the second phase is when the pulse heats up the plasma for the rest of the duration. The initial plasma is characterised by high pressure, temperature and density and expands adiabatically, pushing through the ambient fluid (gas or liquid in our case). Due to the sudden compression of the ambient medium and hence transfer of kinetic energy from the expanding plume to the ambient, a shockwave is generated [74]. The thin layer of compressed gas propagating ahead in supersonic speed is known as the shockfront. The densities on the head and tail of the shockfront are higher and lower than the ambient density, respectively. The density gradients have been measured experimentally and have been well documented in the available literature [47]. The propagating shockwave affects the dynamics of the plume and this effect is prominent in the case of confined geometries [74].

At the initial instants, the shock and the plasma plume propagate with almost the same velocity and only after a few hundred nanoseconds (typically, $t > 200\,ns$) the distinct hemispherical shockfront is seen to be propagating leaving behind the emissive plume [71]. However, this shock is not exactly the same as the one that sets at very early time instants ($t < 50\,ns$), which causes the shock induced density jump and is within the plume [57]. The shockfront is hemispherical in shape at the onset and is well approximated by the point blast model proposed by Taylor and Sedov [145]. One of the conditions necessary for this model to hold good is that the mass of the ambient gas within the shockfront M_a should be much higher than the ablated mass in the plume M_p. The ablated mass calculated in the present experiments (with air as ambient) was close to 0.3μg per laser shot, as calculated based on the scaling laws [77]. This is much smaller as compared to the mass of the gas in the shockfront. The position of the top of the hemispherical top of the shockfront is related to the time by the relation [71];

$$R(t) = \phi_0 \left(\frac{E_s}{\rho_b}\right)^{0.2} t^{0.4} \tag{5.1}$$

Here, ρ_b is the background medium density, E_s is the energy driving the shock, ϕ_0 is a constant that depends on the ratio of the specific heat of the background gas and t is the time instant with respect to the initiation of the ablation. It has been established theoretically with the help of different models that 10-15% of the energy deposited on the target material by the laser pulse releases post ablation and drives the shockfront [146]. In the calculations in the present thesis, the position of the shockfront has been fitted with time using the equation of the form $R(t) = At^n + B$. Since, laser intensity and background gas have been maintained same throughout the experiments, so the term $\phi_0 \left(\frac{E_s}{\rho_b}\right)^{0.2}$ may be treated as a constant.

The parameters of the propagating shock are dependent on the velocity of the expanding plume V_p, the Mach number M, the background gas temperature (T_b) and the background gas density (ρ_b). The plume expansion velocity can be calculated from the position of the head of the emissive plume which is visible at earlier instants. The shock velocity (V_s), shock temperature (T_s) and the density at the shockfront (ρ_s) are given as [145],

$$V_s \approx \frac{\gamma+1}{2} V_p \tag{5.2}$$

$$T_s \approx \frac{2\gamma}{\gamma+1}\left(\frac{\gamma-1}{\gamma+1}M^2+1\right)T_b \tag{5.3}$$

$$\rho_s \approx \left(\frac{\gamma+1}{\gamma-1}\right)\rho_b \tag{5.4}$$

Here γ is the ratio of specific heats of the background gas.

The reflection of shock from physical barriers has also been studied thoroughly by many research groups across the globe and the dependence of reflected shock parameters on the incident shock parameters have been established. The parameters, density at shockfront (ρ), velocity of reflected pressure (P) and the temperature at the shockfront (T) are given as,

$$\frac{T_r}{T_i} \approx \frac{3\gamma-1}{\gamma} \tag{5.5}$$

$$\frac{\rho_r}{\rho_i} = \frac{\gamma}{\gamma-1} \tag{5.6}$$

$$\frac{P_r}{P_i} = \frac{3\gamma-1}{\gamma-1} \tag{5.7}$$

Here the subscripts *r* and *i* represent the reflected and incident shock parameter respectively. However, the above equations hold good for normal shock reflection (longitudinal confinement). In the present study the shockfront is incident on the target at an angle (in case of lateral confinement) and hence the calculation of reflected shock parameters in this case have been carried out using the relations that are different than above. These have been discussed in Section 5.1.2.

To observe the characteristic propagation of shock front in atmospheric pressure, shadowgraph images were recorded. The shadowgraph images have been shown in Figure 5.1. The hemispherical shockfront is clearly seen in the images. Also, the propagation of the shockfront is visible as the size of the hemisphere is increasing as the time is progressing. As expected, it may be seen that the strength of shock is decreasing with the advancement of time, as the shockfront is tending to merge with the background.

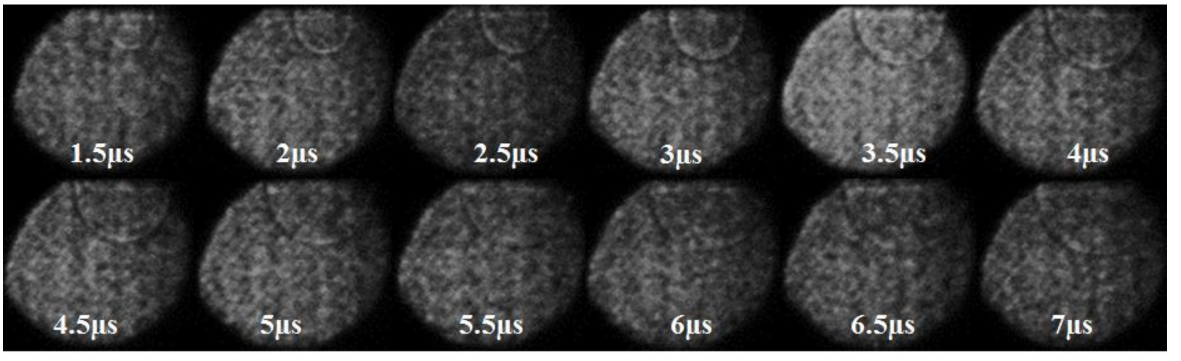

Figure 5.1: Shadowgraph images of the propagating shockfront

The position of the shock front versus time curve was plotted and was found to be of the form, $At^n + B$, with $A = 262.45 \pm 6.21$, $n = 0.48$ and $B = 5.83 \pm 0.015$, which is in accordance with the Taylor Sedov model. The velocity was calculated by using the relation, $v_{avg}(t) = \frac{1}{t}\int_{t_1}^{t_2} nAt^{n-1}dt$, with $t = t_2 - t_1$. From the position of the shockfront versus time curve, the shock velocity at atmospheric pressure was found to be ~862 m/s. The

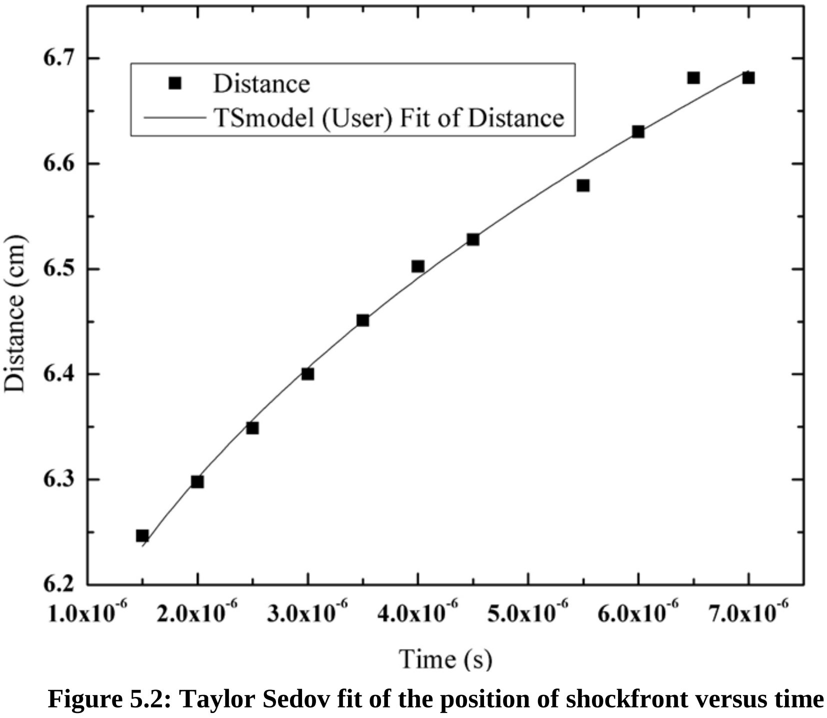

Figure 5.2: Taylor Sedov fit of the position of shockfront versus time plot

Taylor Sedov fit has been shown in Figure 5.2. All the pixel dimensions have been converted to physical distances using the calibration factor of 230 μm/pixel.

For more investigation of the plasma plume and subsequent shockwave, sequence of interferograms has been recorded at different instants of time as shown in the left panel of Figure 5.3. Here, only the representative interferograms have been shown keeping sufficient time interval between them for clear representation of the evolution of the shock front. Appreciable bending of the interference fringes is observed at the central region of the interferogram, which may primarily be attributed to the strong variation in the RI field due to the plasma. It becomes evident that the fringes at the center of the image just above the ablation point were curved in the beginning and with time they tend to become straight. The change of the curvature of the fringes with time is to be correlated with the change in the plasma parameter. Strong opposite shifts at the edge of the fringes (due to compressed and

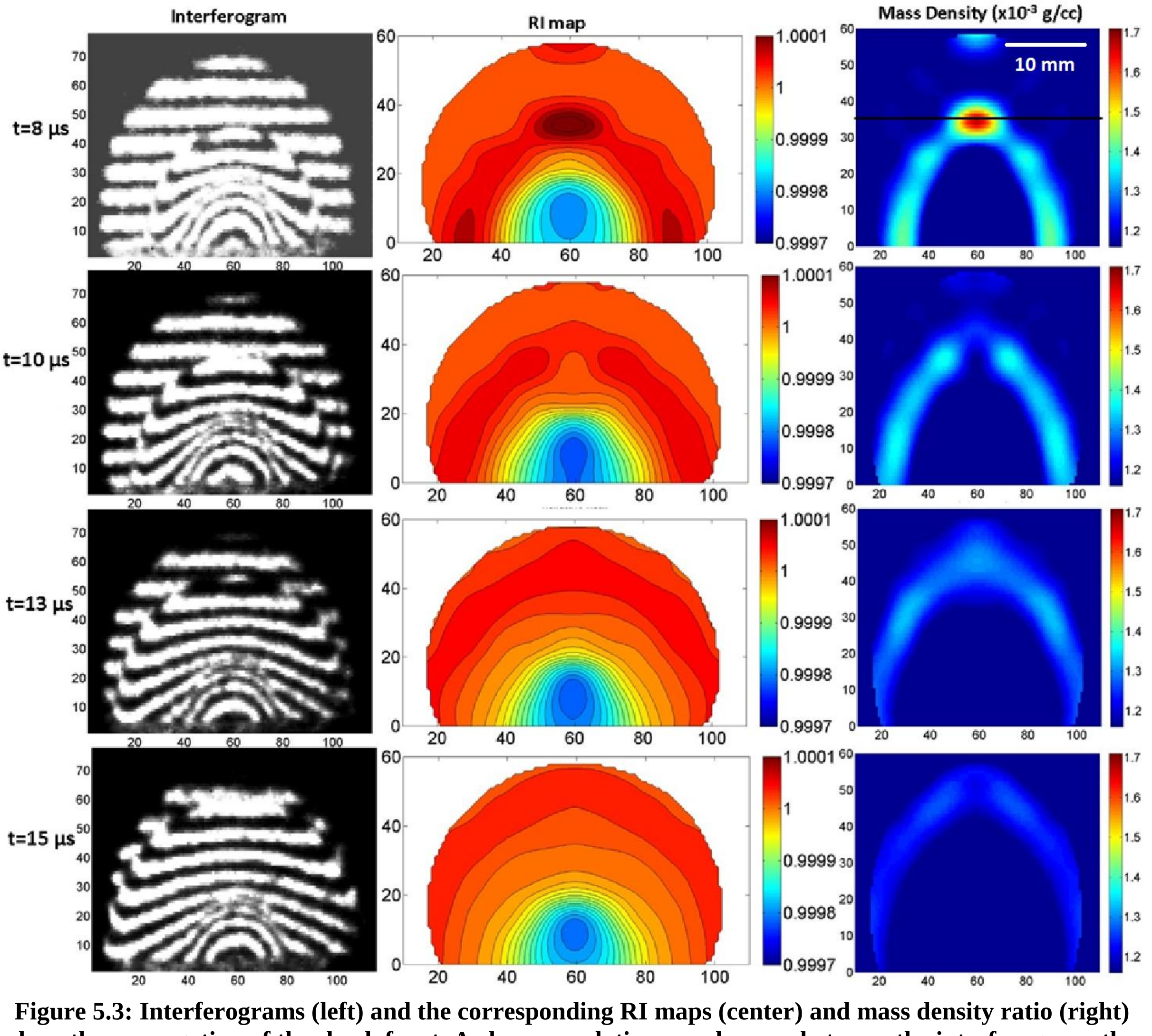

Figure 5.3: Interferograms (left) and the corresponding RI maps (center) and mass density ratio (right) show the propagation of the shock front. A clear correlation may be seen between the interferogram, the corresponding RI maps and mass density maps. The x- and y-axis represent the pixels.

rarefied media on the two sides of the shock front) clearly define the propagating semi-circular shock front boundary.

The quantitative analysis of the recorded interferograms has been performed following the data reduction methodology discussed in Chapter 4. The interferograms have been processed for determining the refractive index field distribution in the field of view and also the 2-dimensional distribution of the associated medium mass density. The time sequence of the respective refractive index fields have been shown in the second column of Figure 5.3.

In the RI maps, there are two distinct regions; one having RI higher than or equal to that of air and the other having RI less than that of the air. The increase in the RI of certain regions above the background value (RI >1) is to be attributed to the compression of the air under the influence of propagating shockwave. The locus of the points of maximum RI (semi-circular in shape) is the boundary of the shock front. In order to calculate the relative density of the medium, we consider only the region where RI is greater than 1. It is to be noted that, in any discussion relating the mass density of the medium, the plasma dominated region (RI<1) has not been included. This region has been separately depicted in Figure 5.5.

The mass density has been calculated corresponding to the RI map, as discussed through Equation 4.14 and has been shown in the third column of Figure 5.3. It may be seen that with the passage of time the density of the medium at the shock front falls down. For instance at $t = 8\ \mu s$, the maximum density achieved at the shock front is ~1.6mg/cm^3, which is nearly 1.4 times the background density, but at 15 μs, the density at the shock front is 1.05 times that of the background. It is seen that with time the high density region moves towards the edge of the shock-front. This becomes evident in the density map corresponding to t=15μs, where the central part of the shock-front may be seen merging with the background but the region to the left and right of it still have appreciably higher density than the background which is roughly 1.05 times the background air density. This is because of the fact that, the central part of the shock, owing to its higher velocity (shock velocity is highest along the propagation direction), compresses the medium more than the edges of the shock do. Therefore, it loses energy faster as compared to the edges.

For better clarity on understanding, the evolution of density perturbation, across the expansion axis, has been analysed. In Figure 5.3, the horizontal line drawn on the density map corresponding to t=8 μs represents the line along which the density variation has been studied. This line is 8 mm above the target surface. The variations of the relative change in the density of the medium (ρ/ρ_0) as a function of the lateral dimension for various time instants have been shown in Figure 5.4. It is to be seen that, as the time evolves, the ratio of

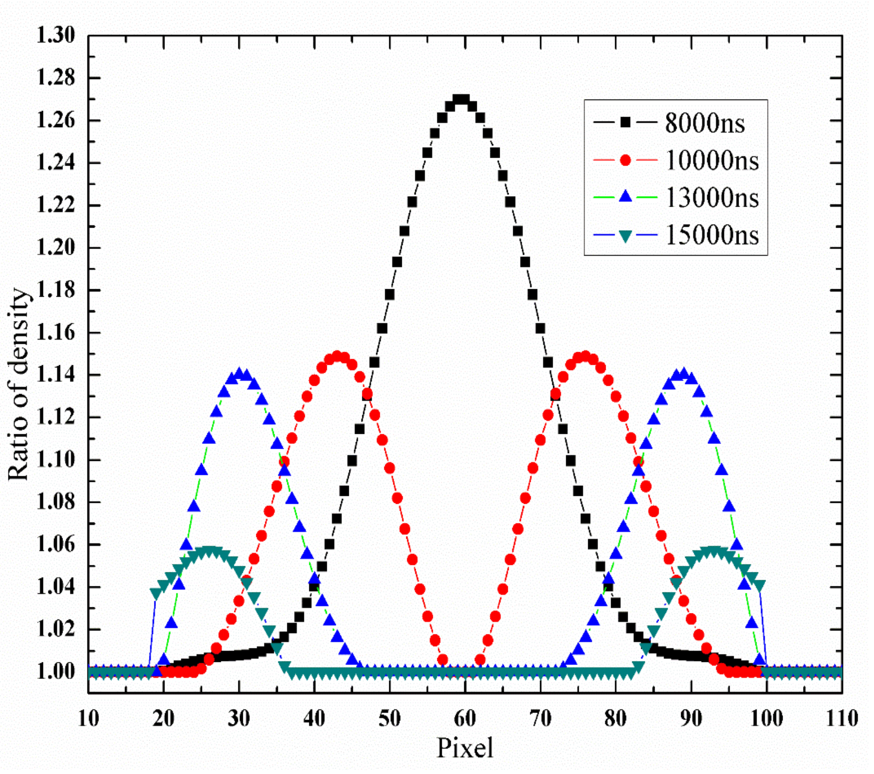

Figure 5.4: The density of the medium at a plane above the target surface and perpendicular to the direction of laser. It is very clear that with passage of time the region of maximum density is moving away from the center and the amount by which the density differs from the background is also decreasing, marking the weakening of the shock.

density keeps reducing. Moreover, the spatial location corresponding to the maximum change in the density is seen to be shifting away from the center, towards the edge of the shock.

As stated earlier, the region where the RI is lower than unity is mainly dominated by the plasma plume, as shown in Figure 5.3 (second column). Therefore, this region of RI map may be used to estimate the 2-dimensional charge (mainly the electronic charge) density distribution of the plasma plume using Equation 4.15. Temporal evolution of the electron density distribution inside the plasma plume has been shown in Figure 5.5. At any given instant the maximum charge density is observed to be at the central region and shows a gradual reduction as one moves away from that region. No appreciable change in the electron density distribution with time is visible. This is because, the time-interval over which the observations have been made, the plasma plume has already reached stagnancy at the atmospheric pressure. It is interesting to note that, the high electron density persists for a longer time. The reason behind this is that, at ambient pressure, plume is confined in a small volume, which increases the collisional processes inside the plume. The increase in the collisional processes is responsible for the prolonged lifetime of the charge density.

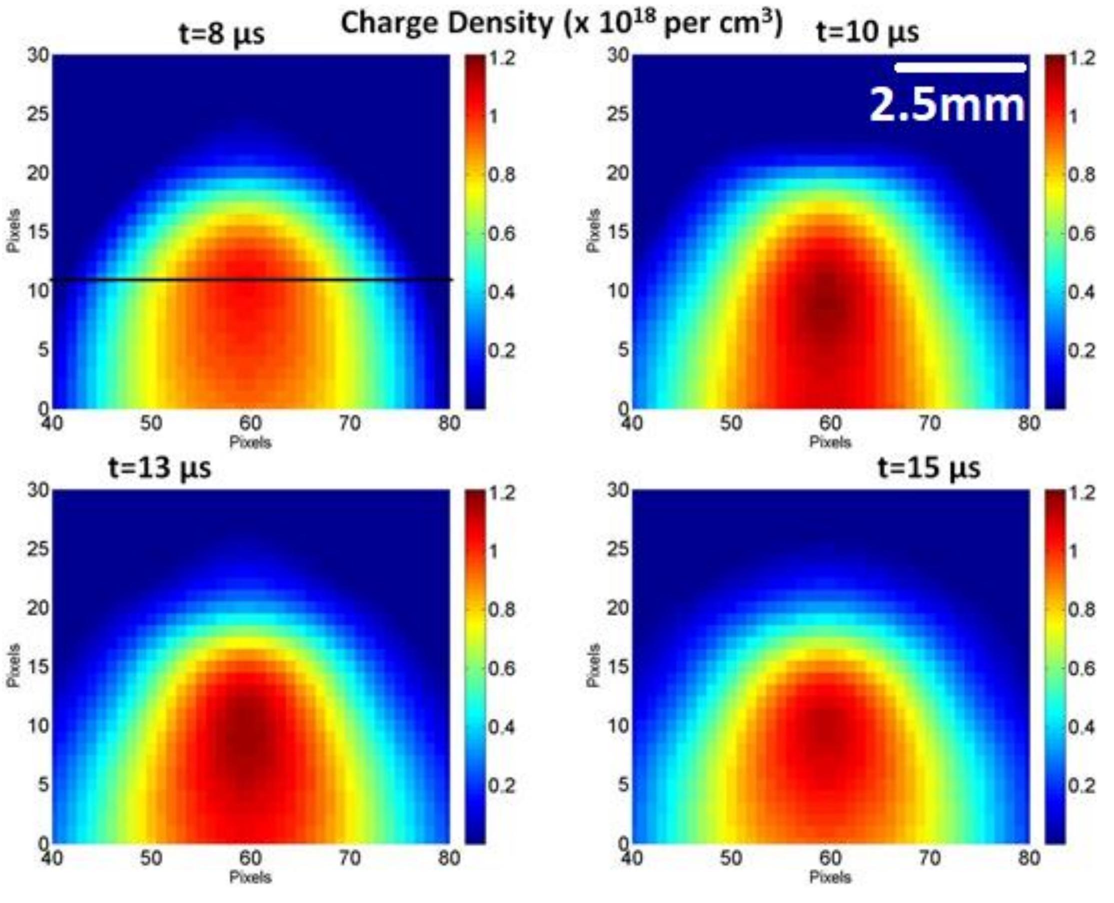

Figure 5.5: The electron density distribution inside the shock region, just above the target surface.

5.1.2. Propagation of shock in air with lateral confinement

When the shock front encounters a physical barrier, it gets reflected and affects the medium as well as the plasma parameters between the two confining surfaces. In order to see the effect of confinement, two parallel metal plates (13.5 mm apart) have been placed symmetrically along the shock propagation direction, as shown in Figure 3.7(b). The observations have been interpreted in terms of RI, medium density and the charge density inside the plume, as was done in the previous case. Figure 5.6 shows the recorded interferogram images (left), the corresponding RI maps (center) and the resultant mass density distribution (right) at different instants of time.

The effect of confinement is not seen till t=10μs as there is no reflected shock front. The fringe deformation is almost identical to that observed in the previous case. However, as the time progresses, for instance at t=15μs, the onset of shock-wall interaction is to be clearly observed in the interferogram shown in Figure 5.6. A clear deformation of the fringe pattern is observed on the confining walls. This deformation is caused due to the shock that is reflected back into the medium, thereby compressing it inward. This leads to the sharp changes in the RI of the medium in the vicinity of the confining walls. Furthermore, with

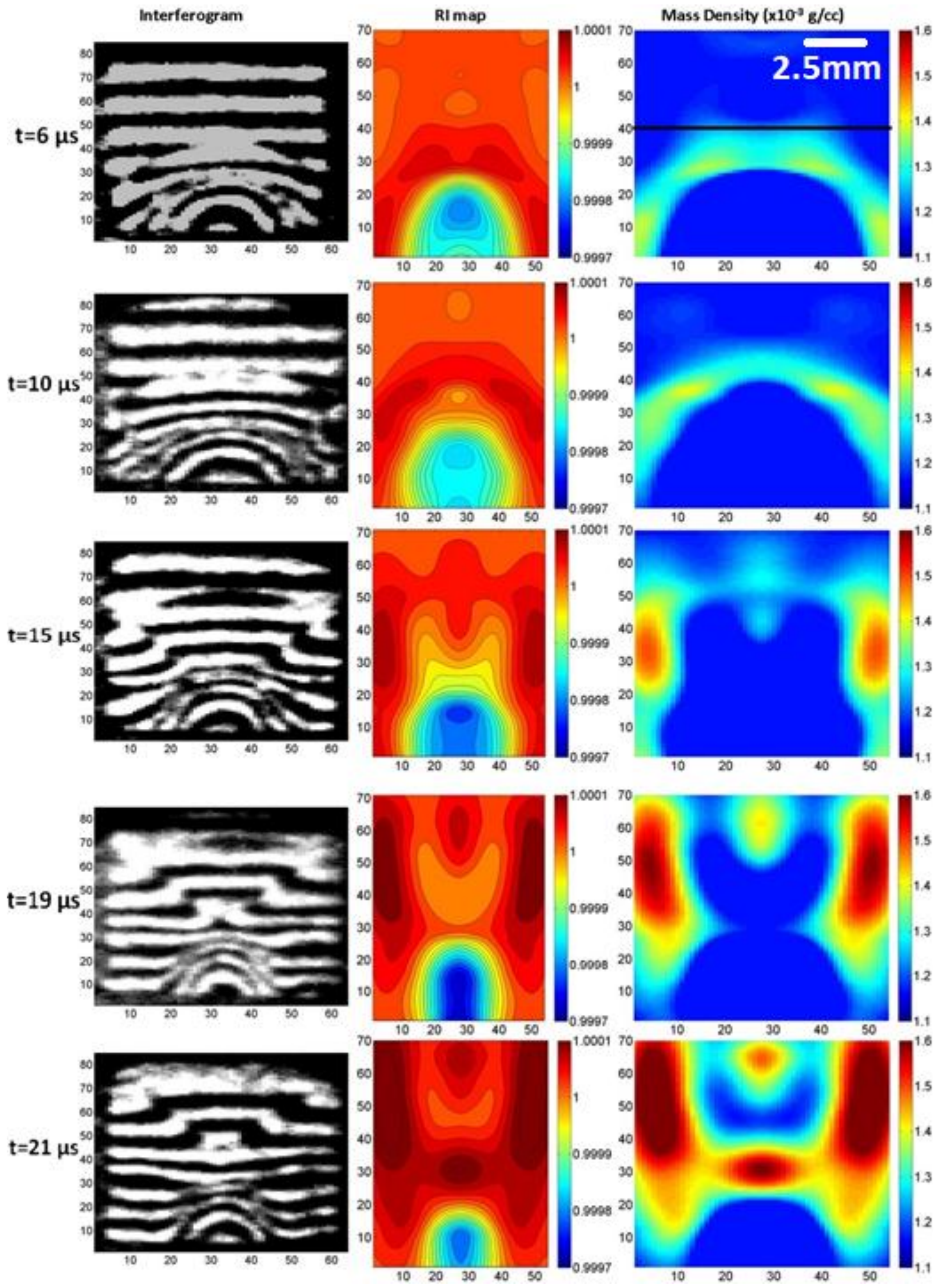

Figure 5.6: RI maps (top) and corresponding interferograms (bottom) for the medium confined between two vertical walls. The effect of shockwave confined between the two walls may be clearly observed at instants later than 10 μs

reference to Figure 5.6, during the later time instants (t=19 and 21 μs), the reflected shock has started dominating after having subdued the effect of initial shock.

This effect is clearly seen in the RI map, which has been shown in the second column of Figure 5.6. Up to 10μs, the higher RI regions are seen to be localized within the spatial extent of the primary shock front. However, as the time progresses to $t = 15\ \mu s$, a high density region can be seen to be taking shape near the confining walls. It, in turn, signifies that the reflected shock has started compressing the medium laterally. At the later instants of time, the high density region attached to the two side walls grows in size and keeps compressing the medium in between. For example, comparing the RI maps shown for $t = 19$ μs and $21\mu s$, one can see that the shock has now created a region of high RI connecting the two walls. It is interesting to note that at $t = 19\ \mu s$ and $21\ \mu s$, the reflected shock is stronger than the primary shock, which is also observed in the interferogram images. The curvature of the fringes close to the walls (corresponding to the reflected shock front) is more than that seen at the onset of the initial shockwave in the medium. Similar observation is highlighted in the corresponding RI map wherein the region of higher RI occupies much more area in between the two walls as compared to that it occupied during the initial instants.

The whole field density distribution of the medium has also been determined for this case as shown in the third column of Figure 5.6. Again, the plasma plume region has not been considered for these calculations. Good correlation is observed between the RI map and the whole field mass density distribution. It is to be seen that the mass density at the shock front diminishes with time, and for instants after $t = 10\mu s$, the high density region starts building up close to the walls. The density maps corresponding to $t = 15\mu s$ and $19\mu s$ reveal an increase in the density up to ~1.5mg/cm^3. The values of maximum density at these two time instants are 1.28 ($t = 15\mu s$) and 1.37 ($t = 19\mu s$) times the background densities. It is also quite evident that this high density region is moving inward. Finally at $t = 21\mu s$, the compression is seen to be grown enough to have created a high density region at the center. The regions close to the two walls have a density of ~1.69mg/cm^3, which is 1.5 times higher than the background density. Also it is interesting to note that this value is higher than the density rise that is seen for t=6μs, which was ~1.18 times the background density. These observations reveal that due to the presence of confinement walls, the effect of shock not just gets prolonged but also remains strong enough.

For better clarity on understanding, the evolution of density perturbation, across the expansion axis has been analysed. In Figure 5.6, the horizontal line drawn on the density map corresponding to $t = 6\ \mu s$ represents the line along which the density variation has been studied. This line is 9.2 mm above the target surface. The variations of the relative change in the density of medium ρ/ρ_0 as a function of the lateral dimension for various time instants have been shown in Figure 5.7. It is to be seen that, as the time evolves, the ratio of density keeps reducing in the region of primary shock front. Two peaks are to be seen in each of the plots, which are symmetrically located on either sides of the ablation point. Once the effect of confinement surfaces (at $t = 15\mu s$), the magnitude of the two peaks are seen to be increasing

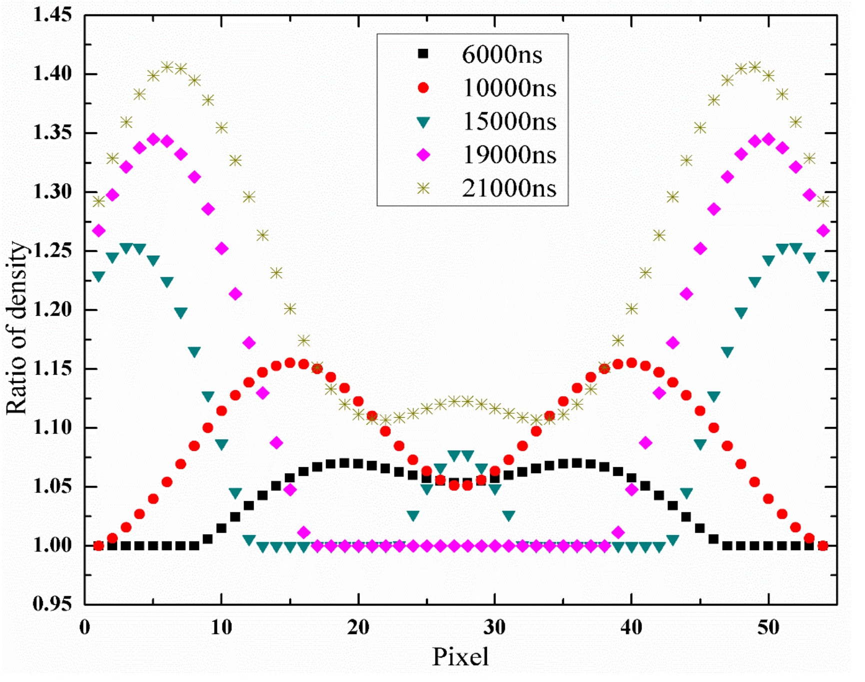

Figure 5.7: Plot of the ratio of density of the shock region to the background density at different instants of time at a plane which is 9.2 mm above the target surface. The ratio versus position has been plotted between the two walls.

and reaching a maxima at $t = 21\mu s$. Contrary to the previous case where the shift was found to be moving towards the edge, here they are seen to be moving inward with the evolution of time, which is expected because the reflected shock front is moving inwards building the compression causing the increment in the mass density.

The mass density distribution in the presence of the confinement wall (third column of Figure 5.6), could be explained as follows. The propagating primary shock front advances in the medium and reaches to the confining boundary and gets reflected back in the medium. With the evolution of time, the point of shock-wall interaction is seen to be moving in upward direction. In this scenario, the reflected shock front that originated at an earlier instant would advance more in the medium compared to its counterpart that started off later in time. In order to get the direction of the reflected shockwave, the spherical shockwave has been approximated as the plane shock front for short extents of space and instants of time. Therefore in the present case, the tangents of the spherical shockwaves represent the direction of plane shock fronts at the point of interaction, as shown schematically in Figure 5.8.

For the calculated shock velocity, the Mach number (M) comes out be 2.61. With this speed the shock would take ~8 μs to make the first contact with the boundary which is 6.75mm apart from the point of ablation. With these considerations, the angle of incidence of the shock front (β) has been calculated, as shown in the schematic in Figure 5.8 and as discussed in the previous paragraph. The value of β at t=8μs comes out to be ~29^0. The angle of reflection of shock (δ) has been measured using the formula, $tan\delta = tan\beta([cos^2\beta -$

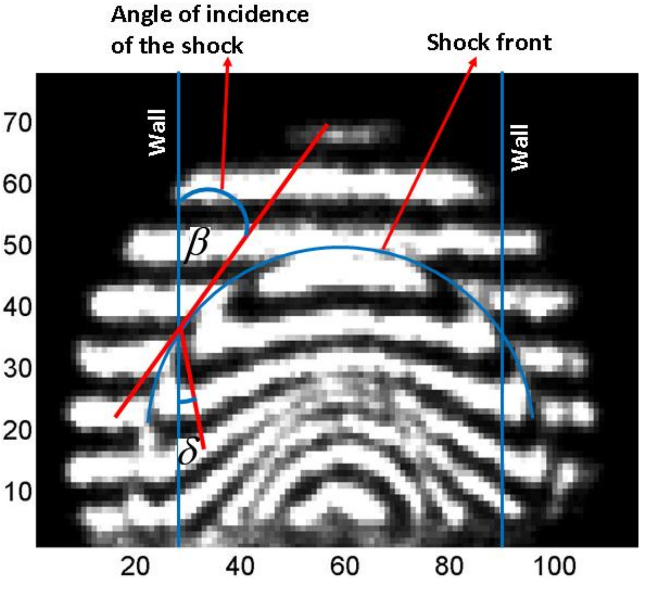

Figure 5.8: The scheme for finding the shock angle for the primary shock. The interferogram shows the shock front at 10μs when no confinement is there. The circle is approximate fit of the shock front. The angle the tangent makes with the wall is the shock angle.

$cot^2\beta]/[1 + \frac{1}{2}M^2(\gamma + cos2\beta)]$, where γ (=1.4) is the ratio of specific capacities for air [147]. The angle δ comes out to be 7.9^0 in our case. Also, the density at the shock front comes out to be ~1.4 times the background density in case of free propagation which is again in close agreement with the observed value 1.26. The ratio of densities was calculated by using the relation, $\rho_2/\rho_1 = (\gamma + 1)M^2sin^2\beta/[2 + (\gamma - 1)M^2sin^2\beta]$.

Apart from the perturbation of the medium density, reflected shockwave significantly changes the electron density distribution of the plasma plume as well. Figure 5.9 shows the two dimensional distribution of the electronic charge density for the plasma region (where RI < 1) The time evolution of the charge distribution shown in Figure 5.9 reveals that the electronic charge in the plasma region is getting reduced with time up to 10 μs, where the shock reflection is not significant. Strong lateral confinement of the charge density profile is observed for the time delay greater than or equal to 15 μs, where the medium density is getting perturbed by the shock reflected by the confining walls. Cross sectional extent of the charge density profile shrinks sharply and overall profile becomes narrower resulting into increment in the overall electron density as compared to the observed electron density in absence of the reflected shock. Further, it is interesting to note that the charge density as well as its axial and lateral dimensions are reduced at relatively higher time instants, t=21μs. This could be understood as follows: at higher time delay, the reflected shock fronts from the either sides approach towards the central region. This creates the high density region in front

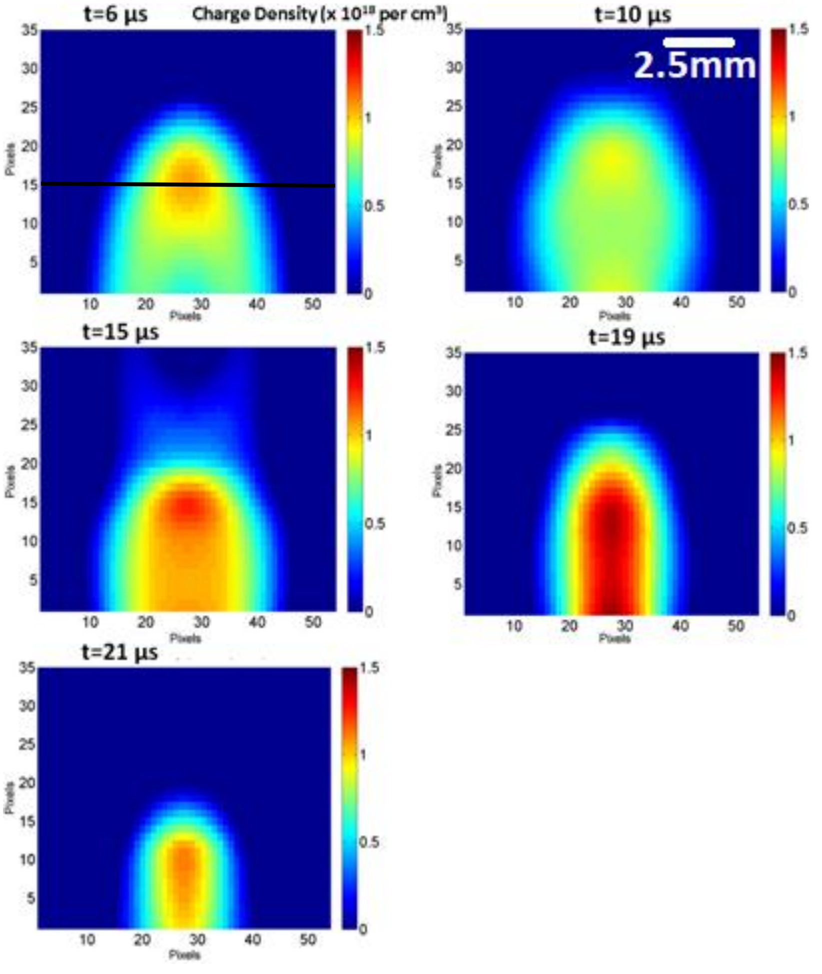

Figure 5.9: The electron density distribution map inside the shock region, just above the target surface.

of the plasma plume as well. Thus, we can say that at higher time delay, the plasma plume is surrounded by the compressed medium, which in turn arrests the expansion of the plasma plume. In the region of strong confinement, the thermalisation processes of the plasma plume is expected to expedite because of the recombination process. This could be the reason behind the reduction of the electron density at higher time delay.

In order to present the charge density distribution along a horizontal plane a section at the height of 3.7mm from the target surface has been plotted and shown in Figure 5.10. For reference, this plane has been schematically shown in the form of a horizontal line in Figure 5.9 for $t = 6\mu s$. The plots in Figure 5.10 also reveal that a high charge density region starts evolving at $t = 15\mu s$ (the onset of the effect of reflected shock) and rises till 19μs and the region gets squeezed at 21μs. This is in agreement with the observations that have been

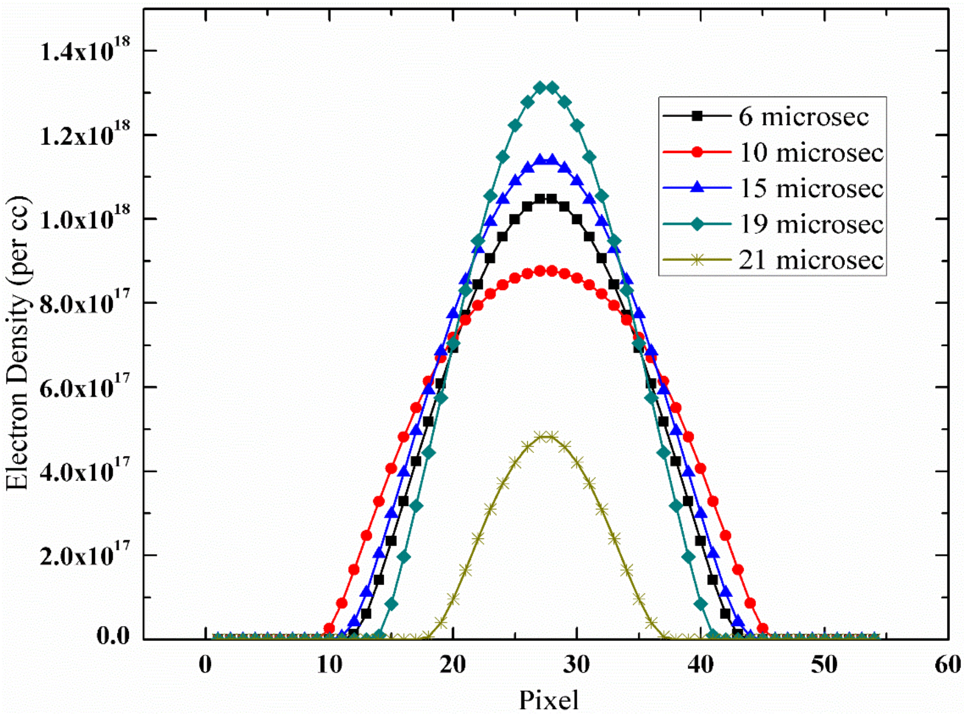

Figure 5.10: Electron density distribution on a plane 3.7 mm above the target surface.

described in the preceding paragraph.

5.1.3. Propagation of shock in air with longitudinal confinement

Continuing in the similar line, the studies relating to the reflection of shockwaves have been carried out with longitudinal confinement geometry. In order to see the effects a metal plate was placed at a height of 10 mm from the target surface, as shown in Figure 3.7(c). The observations have been interpreted in terms of RI, medium density and the charge density inside the plasma plume. The results have been summarised in Figure 5.11 in which the first, second and the third column have the interferogram images, the RI-maps and the 2-dimensional mass density distributions, respectively.

Up to $t = 15\mu s$, the propagation of the primary shock was observed and it was similar to the case of propagation of shock in absence of confinement. At later time instants ($t = 25\mu s$ and $28\mu s$), the effect of reflected shock may be seen in the interferogram images where the fringes are seen to be bending, close to the edges of the fringe systems in the vicinity of the top plate. Although the deformation is not as sharp as it was observed in the case of lateral confinement, yet it is evident from the comparison of the interferogram images corresponding to $t = 19\mu s$ (where the shock front has surpassed the field of view) to that at $t = 25\mu s$ (where the effect of shock-plate interaction starts showing up, close to the edges from the top). These observations become more significant in the RI-maps shown in the

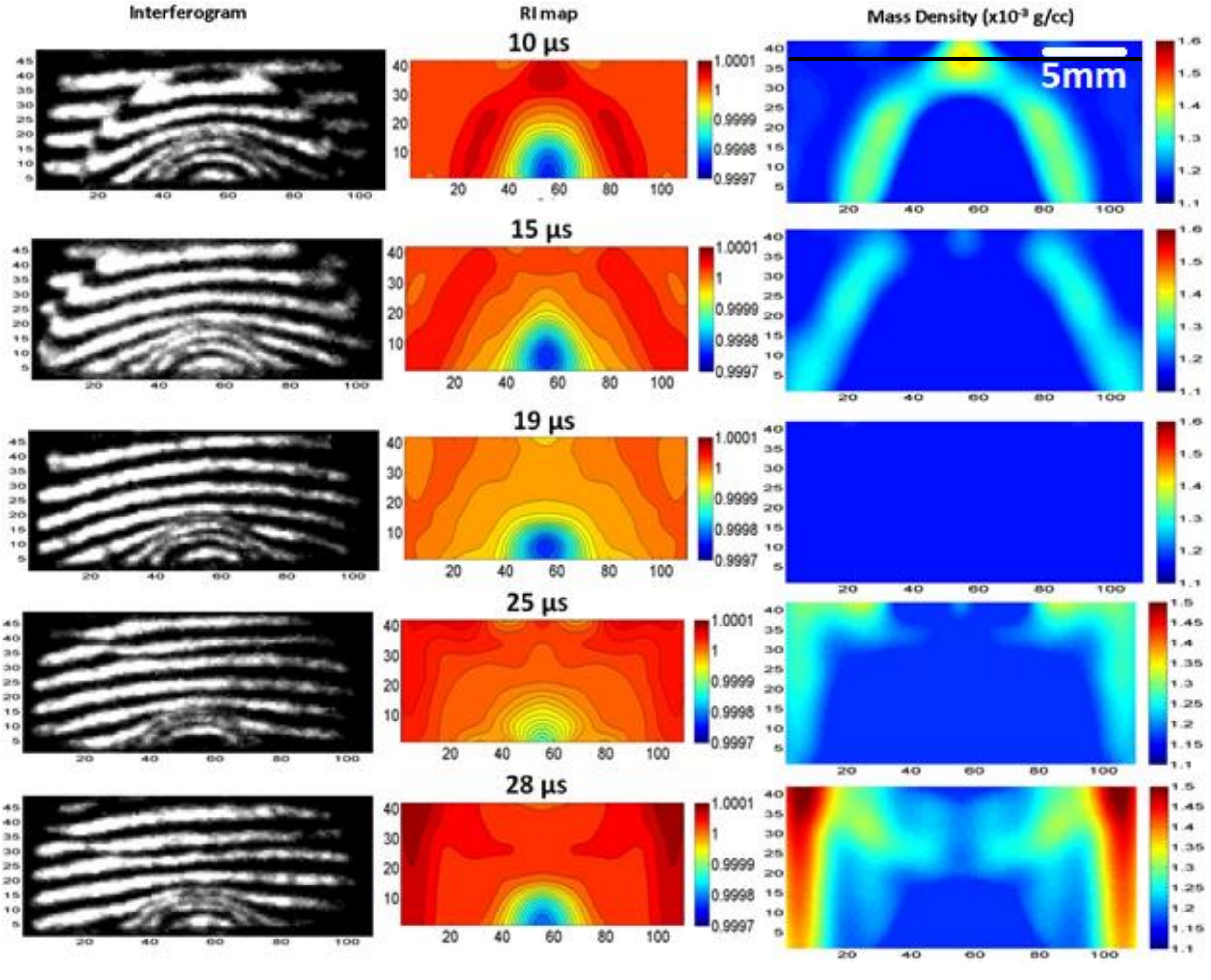

Figure 5.11: Interferograms (left) and corresponding RI maps (right) for the medium confined between the target surface and a horizontal top plate.

second column of Figure 5.11. The RI-maps corresponding to the instants $t = 15\mu s$ shows the weakening of the primary shock. At $t = 25\mu s$ clear signature of the reflected shock is to be observed.

The whole field density distribution for this case has also been determined and has been shown in the third column of Figure 5.11. At $t = 10\mu s$ and $15\ \mu s$, the strength of density perturbation has gone down. At $t = 25\mu s$ and $28\mu s$, the density build-up takes place and it starts evolving from the two sides of the top confining plate. The shock-front is found to be evolving from the two sides of the top plate and not from the center. The absence of the effect of reflected shock front at the central region is because of the presence of a hole that was made to let the ablating laser beam pass through (as shown in Figure 3.7 (c)). Here the maximum density reached at the shock-front in case of the primary shock is ~1.16 times the background density but in case of reflected shock it is ~1.26 times the background density.

The evolution of density perturbation, across the expansion axis, has been analysed for a better insight. In Figure 5.11, the horizontal line drawn on the density map corresponding to $t = 10$ μs represents the line along which the density variation has been studied. This line is 7.4 mm above the target surface. The variations of the relative change in the density of medium ρ/ρ_0 as a function of the lateral dimension for various time instants have been shown in Figure 5.12. Two peaks corresponding to the maximum value of the density ratio shift apart with respect to the point of ablation (center point of the target surface) and move closer to the edges of the target surface. For $t = 19\mu s$ no density variation compared to the background medium is to be observed, as the density ratio approaches unity.

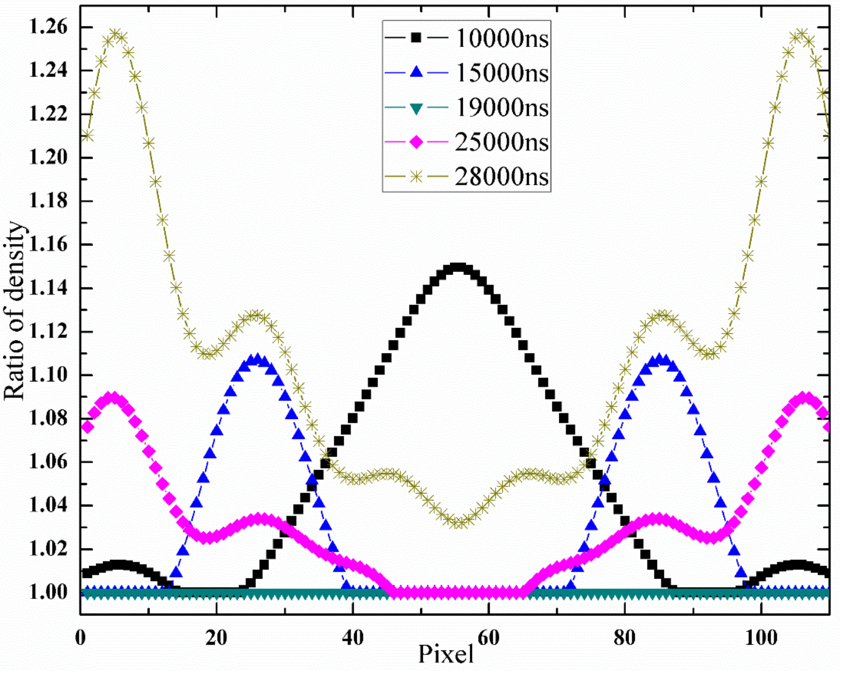

Figure 5.12: The density distribution on a plane parallel to the target surface and at a height of ~7.4mm from the same.

However, during the final stages of the phenomenon i.e. at $t = 25\ \mu s$ and 28 μs, the region of relatively higher mass density can be seen building up near the edges of the confining top surface. This in turn points towards the build-up of compression that pushes the medium back towards the target surface and hence a clear effect of shock can be seen.

Figure 5.13 shows the temporal evolution of electron density distribution in case of confinement from the top. From the charge distributions shown, the higher charge density region can be seen to remain more or less stagnant and does not evolve much with time. However, at the later instants of time ($t = 25\mu s$ and $28\mu s$), due to the reflected shock the region containing the charged particles starts shrinking. In case of reflection, as seen in the present case and the previous case, the recombination process certainly gets affected. The

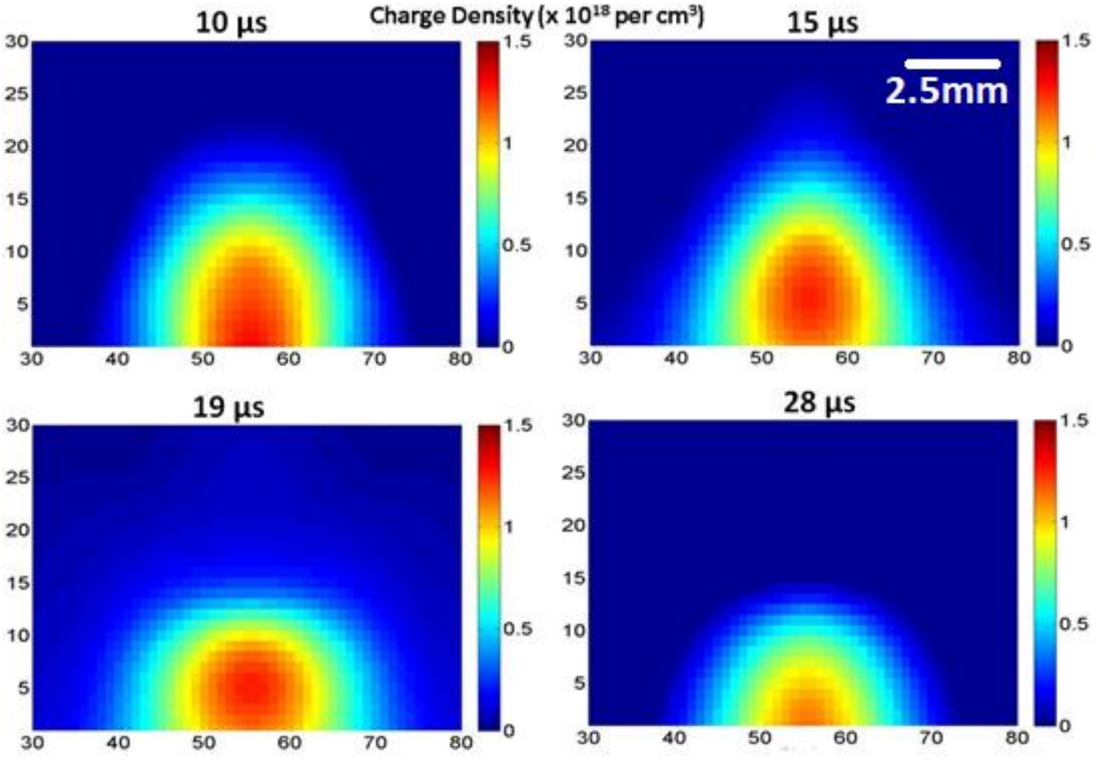

Figure 5.13: Evolution of electron density with time in case of shock propagation with a top plate confining the shock

overall behaviour of the charged region is now primarily governed by two competing mechanisms; the natural recombination and the compression of the medium due to the reflected shock. In contrast to the case of confinement with walls (lateral confinement), the impact of the reflected shock on the evolution of charge density distribution is not that significant when the confining surface is longitudinally placed above the target surface.

A one to one comparison of the three cases (propagation in air without confinement, lateral confinement and longitudinal confinement) considered in the present experimental study has been made through Figure 5.14. The interferogram images recorded at t=15μs and the corresponding mass and electronic charge densities as quantitatively determined from the interferogram images have been shown. In qualitative sense, the extent of fringe deformations observed in the three cases is quite different. Strong fringe deformations due to the reflected shock are clearly evident in the case of lateral confinement. On the other hand, such effects are not to be seen in the absence of physical confinement or in case of longitudinal confinement. In the mass density map, it is to be seen that, in the absence of confining

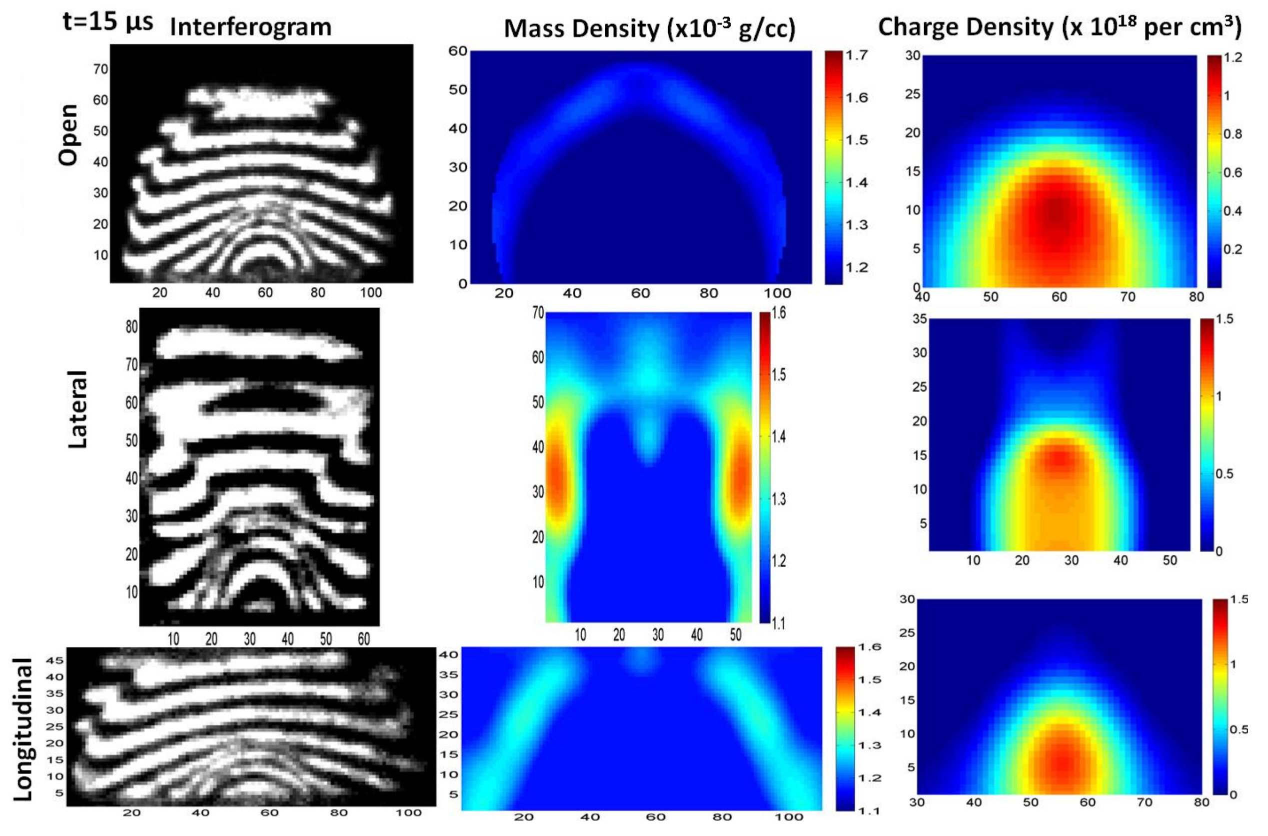

Figure 5.14: Comparison of the shock fronts at a given instant of time under different conditions, that is, free propagation, lateral and vertical confinements (from top to bottom)

surfaces the shock advances with the passage of time and the shock front weakens, similar observations have been made for longitudinal confinement; but in case of lateral confinement a region of higher mass density is seen to be evolving close to both of the confining surfaces. Looking at the charge density distributions, it becomes clear that in absence of any confining boundary, the charge distribution is spread and the maximum density is found to be at the center. In case of lateral confinement the spread of the charge density is less and a denser region is seen to be formed at the center for the same amount of laser fluence. In contrast to these two cases, in the case of vertical confinement the charge distribution has spread and has shrunk considerably, while the maximum charge density is still to be observed at the center of the distribution. From here it is to be inferred that the reflected shock in the medium strongly governs the mass density of the medium and the charge density in the plume.

5.2 Time resolved interferometric study of the plasma plume induced shockwave in liquid media

The density perturbations play a crucial role in the implementation of LAL in applied research. Therefore, a detailed quantitative analysis of the whole field mass and electronic charge density perturbation is necessary. As an attempt to develop this understanding, this section is concerned with the experimental investigation of the effects of propagation of laser-induced shock wave in liquid media of different densities. Experiments have been performed with water and aqueous solutions of ethylene glycol (EG) with two different concentrations. Using interferometric technique, the refractive index (RI) variations over the field of view have been captured. Detailed quantitative information of the mass density distribution and the effect of medium density on electronic charge density in the plume region has been obtained by using these RI distributions. The transient evolution of the shock and its effects on the medium have been discussed in detail.

The sequence of the interferograms at different time delays have been recorded to observe the dynamics of the shock and the plasma plume that resulted from laser ablation of metal substrate immersed in the liquid media. For quantitative understanding, the interferograms have been converted into refractive index (RI) maps and the change in RI with respect to the background has been converted to the charge density and density perturbations of the medium. The concerned data reduction methodology has already been discussed in detail in the previous chapter. The complete study has been presented in two sections, namely, laser ablation of copper in water and laser ablation of copper in aqueous solutions of ethylene glycol (EG). Two different proportions of EG have been considered; 25% (w/w) and 50% (w/w) aqueous solutions of EG.

5.2.1 Laser ablation of copper in water

The characteristic propagation of the shockwave in the medium was captured by recording the shadowgraph images at different instants of time. Position of the shock front versus time curve was plotted and the curve was fitted to Taylor Sedov model, $r(t) = At^n$, with $n = 0.86$ and $A = 378.14 \pm 2.67$. The average velocity was determined from this fitted curve as, $v_{avg}(t) = \frac{1}{t}\int_{t_1}^{t_2} nAt^{n-1}dt$, with $t = t_2 - t_1$ and was found to be equal to ~1743 m/s. The position of the shock front versus time curve and the corresponding Taylor Sedov fit has been shown in Figure 5.15.

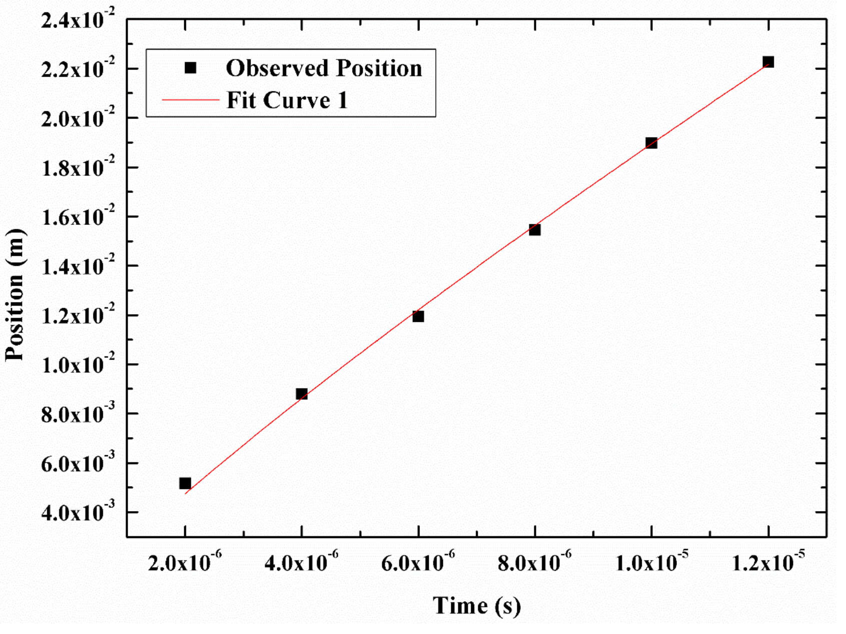

Figure 5.15: Plot of the position of shock front versus time derived from the shadowgraph images. The corresponding Taylor Sedov fit has been shown and the fit parameters have been tabulated.

Further investigations on shock wave and the plasma plume were carried out by analysing the interferograms recorded at different instants of time. The time-lapsed interferograms have been shown in the left column of Figure 5.16. Labels a, b, c, d and e correspond to the time instants of $t = 2, 4, 6, 8$ and $10\ \mu s$ respectively. It is to be mentioned here that only the representative interferograms have been shown that are evenly spaced in time, so that the evolution of the shock can be clearly depicted. It is evident from the interferogram shown in Figure 5.16(a) that just above the ablation point, the fringes are significantly deformed. This bending of the otherwise straight and parallel fringe patterns is due to the strong variation in the RI of the medium in this region, which is attributed to the presence of the plasma plume. As the same region is seen in the subsequent interferograms, the corresponding fringes seem to get straightened because of the changes in plasma parameters with the passage of time. Close to the edges of the deformed fringe pattern, strong opposite shifts are observed (due to the compressed and rarefied media on either sides of the shock front), which clearly define the propagating semi-circular shock front boundary.

The recorded interferograms have been analysed using the methodology discussed in the previous section and the RI map (whole field refractive index distribution) corresponding to every spatial location of the interferogram has been generated. The time sequence of the RI maps corresponding to each interferometric image has been shown in the second column of Figure 5.16. Two distinct regions are seen in the RI map; one having RI greater than or equal

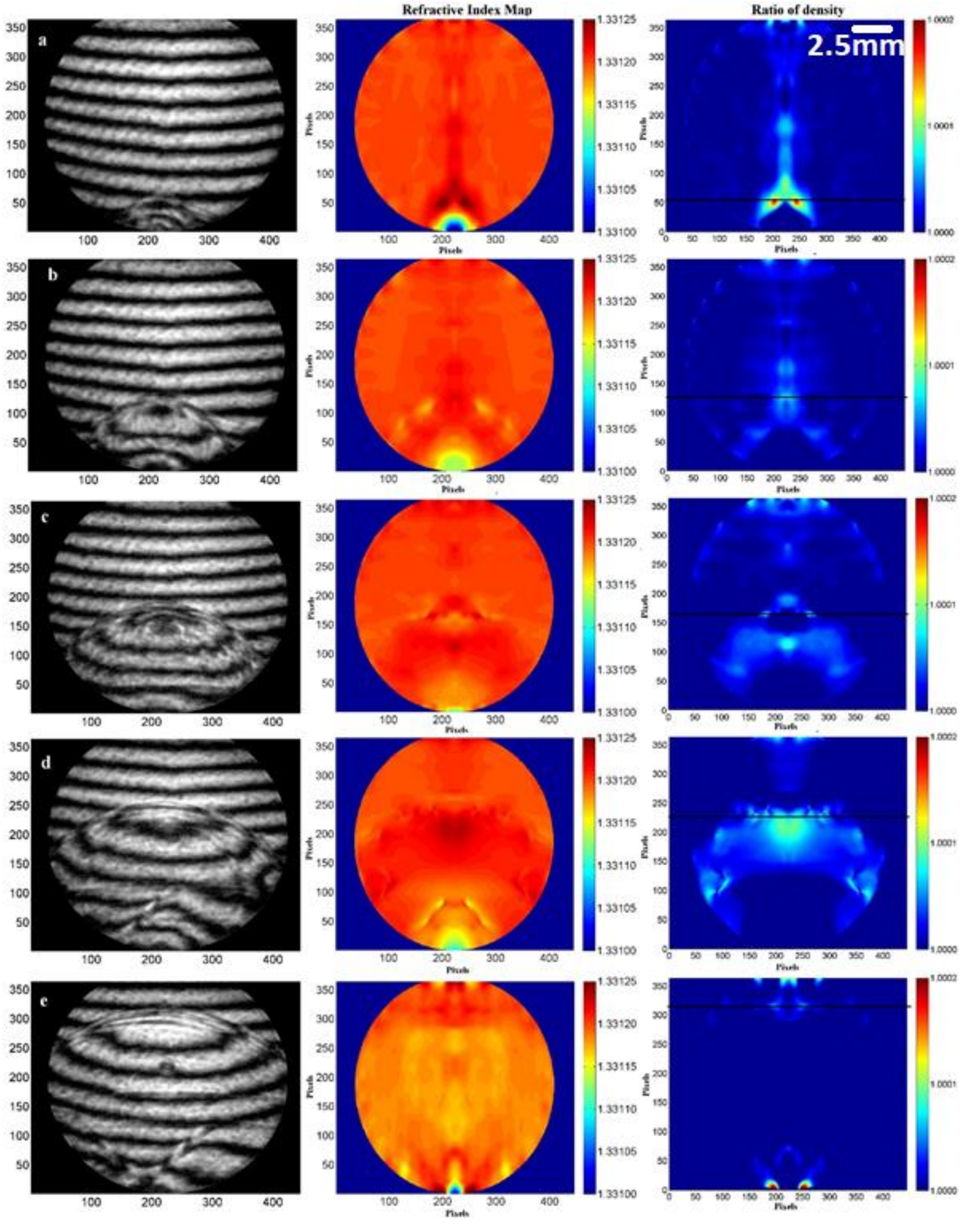

Figure 5.16: The interferograms (left). RI maps (center) and the ratio of mass densities (right). The labels *a, b, c, d* and *e* correspond to 2, 4, 6, 8 and 10 µs, respectively. In the images shown, one pixel corresponds to a physical dimension of 55 µm.

to that of water ($n_w = 1.3312$) and the other having RI less than that of water. The observed increase in the RI values in some regions with respect to the background (RI of water) is to be attributed to the compression of the medium under the influence of the propagating shock wave. The locus of the points of highest values of RI, which describes a semicircle, is to be identified as the boundary of the shock front in the medium. The density of such regions in all the RI maps has been calculated and the ratio of the calculated density to the background density of water ($\rho_w = 0.9971\ \mathrm{g/cm^3}$) has been shown in the third (the rightmost) column of Figure 5.16. For calculation of mass density of the medium, only the regions having RI greater than or equal to that of water have been considered. Regions having RI less than that of water appear in the initial time instants and are primarily dominated by the plasma plume. At later instants of time, however, the cavitation occurs and the bubble is formed, which scatters most of the light and is seen to be forming a dark region closer to the target surface. While interpreting the interferograms, this fact has been considered and hence only the interferometric images corresponding to $t = 2$ and 4 μs have been considered to determine the charge density in the plume. A comparative study of all the three cases has been presented later.

The mass density calculations have been carried out by making use of Lorentz-Lorenz relation (Equation 4.14 and 4.14a). It can be seen in the third column of the Figure 5.16 that the density at the shock front shows a decreasing trend with time. Since the bulk modulus of water is quite high (2.2 GPa), a significant compression of the medium is not expected. The densities of the medium at $t = 2\ \mu s$and $t = 10\ \mu s$ are 1.00017 times and 1.00004 times the background density, respectively. Although these density variations are not very high, yet these may be seen in quantitative terms in the mass density maps of Figure 5.16. Also, it is to be seen that the region of maximum compression is moving away from the centre as the time advances. This may be correlated with the higher axial velocity of the shock front in comparison to its off-axial component. This, in turn, means that the central part of the shock compresses the medium more as compared to the edges and hence loses energy faster. A close observation of Figure 5.16(c) and 5.16(d) reveals that there is a wider region over which the perturbation is prevailing, instead of just the shock front. This is because of the fact that there are waves getting reflected from inside the target and these waves are also contributing to the perturbation. Hence, the RI maps and/or the mass density maps shown in the figure basically represent the resultant of all the wave fronts (primary and reflected). A detailed discussion on this phenomenon has been presented later in a different section (Section 5.2.3).

For better clarity on understanding the temporal evolution of the shock front, the density variation across the expansion axis has been analysed. The black horizontal lines drawn in the density ratio maps in Figure 5.16 correspond to the horizontal sections across which the density variations have been studied. At $t = 2\ \mu s$, this line is 2.75mm above the point of ablation. Similarly, in all the other images, the density variation across the mass density map has been studied at the shock front. These variations have been plotted as a function of lateral dimension and have been shown in Figure 5.17. The density variation is the maximum at the initial time and then it keeps decreasing thereafter. Also, the lateral spread of the shock increases and, as expected, the shock energy is found to be spreading outward with time. The dip in the plot corresponding to $t = 2\ \mu s$ may be because of the abrupt change in RI values locally due to the breakdown of water caused by the laser beam. This effect is also reflected in the corresponding RI and mass density maps shown in Figure 5.16. At later instants of time, the shock gets reflected from the water-air interface and comes back in the medium. However, these reflected shock waves have not been studied in the present work.

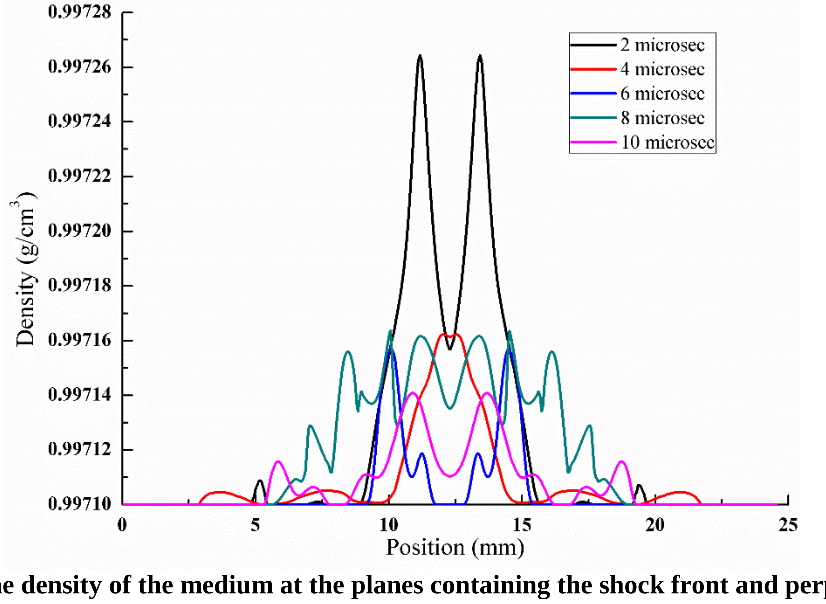

Figure 5.17: The density of the medium at the planes containing the shock front and perpendicular to the direction of ablating laser beam (*x* = 12.5 mm represents the ablation site).

5.2.2. Laser ablation of copper in aqueous solution of ethylene glycol

Ethylene glycol (EG) has been one of the most commonly employed heat transfer fluids. Unlike water, EG is more viscous and dense and has extensively been used as the host fluid for preparing metallic nanoparticle suspensions, commonly known as nanofluids [64, 148, 149]. Among the various methods available for preparing such nanofluids, ablation of the bulk metal in the host fluid itself i.e. the aqueous solution of EG has been one of the direct approaches. In view of the fact that this method involves laser ablation in liquids, it becomes imperative to develop an understanding of the phenomenon of the laser plasma-induced shock wave propagation in such solutions. In this context, the LAL experiments have been performed in aqueous solutions of EG of two different densities in the present work. Comparisons have been made in terms of the density perturbations in the EG medium with water as the reference fluid. As stated above, the aqueous solutions of EG with two different proportions, 25% (w/w) and 50% (w/w), have been prepared and the characteristic propagation of shockwave was observed by recording shadowgraph images. The velocities of shockwave have been found to be ~1914 m/s for 25% EG solution and ~1986 m/s for 50% EG solution.

Interferometric images corresponding to different instants of time have been recorded to observe the shock propagation through the medium in both the cases. The recorded interferograms have been analyzed using the data reduction methodology discussed in the previous section and the corresponding RI maps and mass density distributions have been obtained. The interferograms for both the concentrations of EG have been shown side by side in Figure 5.18 to have a clear comparative view. The interferograms shown here are again the representative images, like in the previous case, to give a clear qualitative understanding of the evolution of the shock front. The labels, a, b, c and d correspond to time instants of $t = 2, 4, 6$ and $8\,\mu s$ respectively. In the images shown, the horizontal axis represents the lateral dimension on the target surface with ablation site at the centre. As indicated in the figure caption, one pixel size corresponds to a physical dimension of 55 μm. It may be seen from the interferograms that the shock front is propagating slightly faster in 50% EG solution, which is in accordance with the difference in the speeds of the shockwave in the two cases, as presented above. The oppositely oriented bends in the fringes closer to the edge of the fringe pattern is because of the compression and the rarefaction of the medium ahead and behind the shock front, respectively. As earlier seen in the case of water, here also, the locus of points with maximum bending of fringes (the regions with maximum change in RI) describes a semicircle, which is the boundary of the forward moving shock front.

The mass density maps (corresponding to the interferograms shown in Figure 5.18) for two different concentrations of EG have been shown in Figure 5.19. The physical dimensions along the *x* and *y* directions of the maps shown are the same as that mentioned in

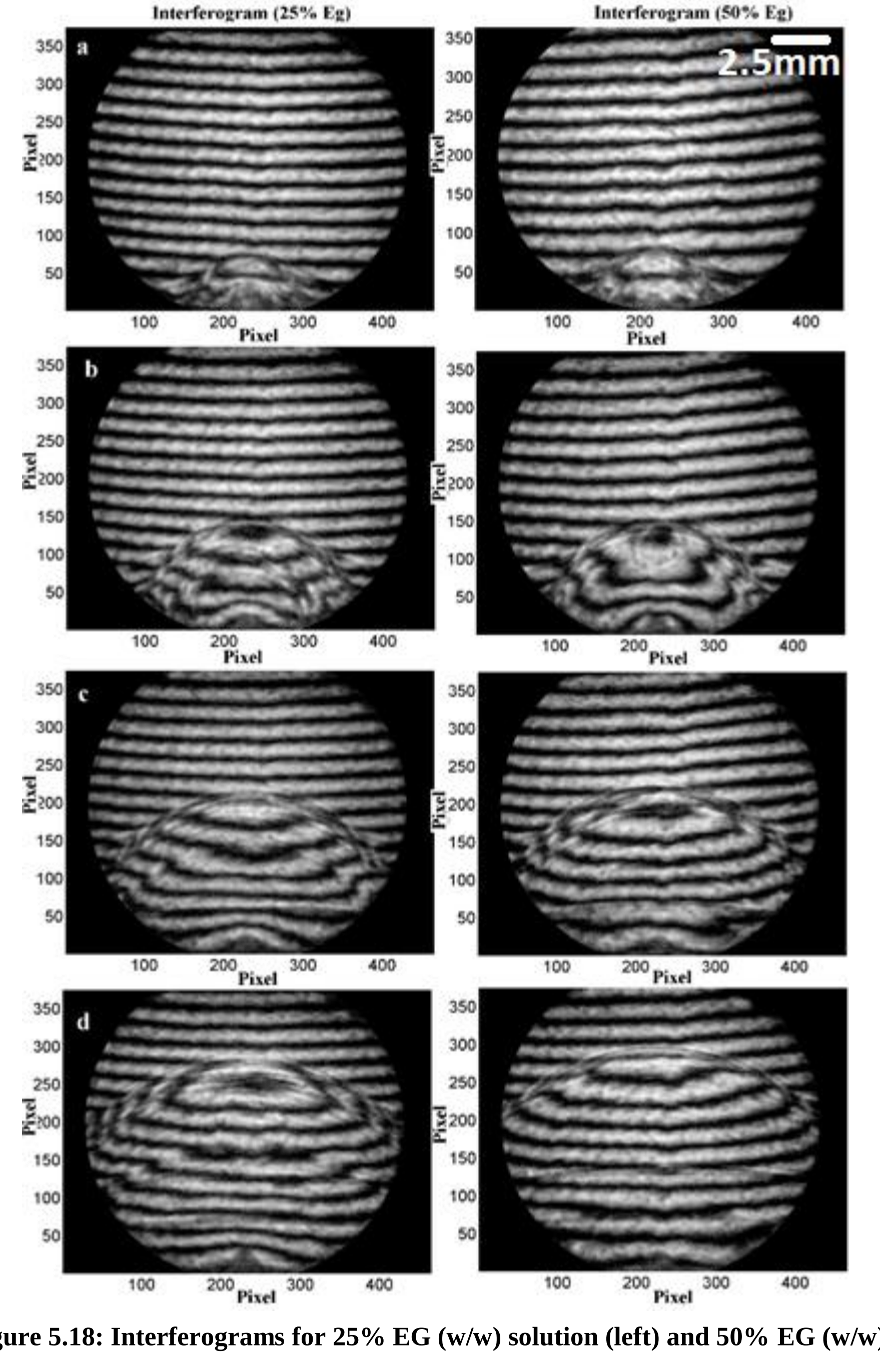

Figure 5.18: Interferograms for 25% EG (w/w) solution (left) and 50% EG (w/w) solution (right). The labels a, b, c and d correspond to 2, 4, 6 and 8 μs respectively. In the images shown, one pixel corresponds to a physical dimension of 55 μm.

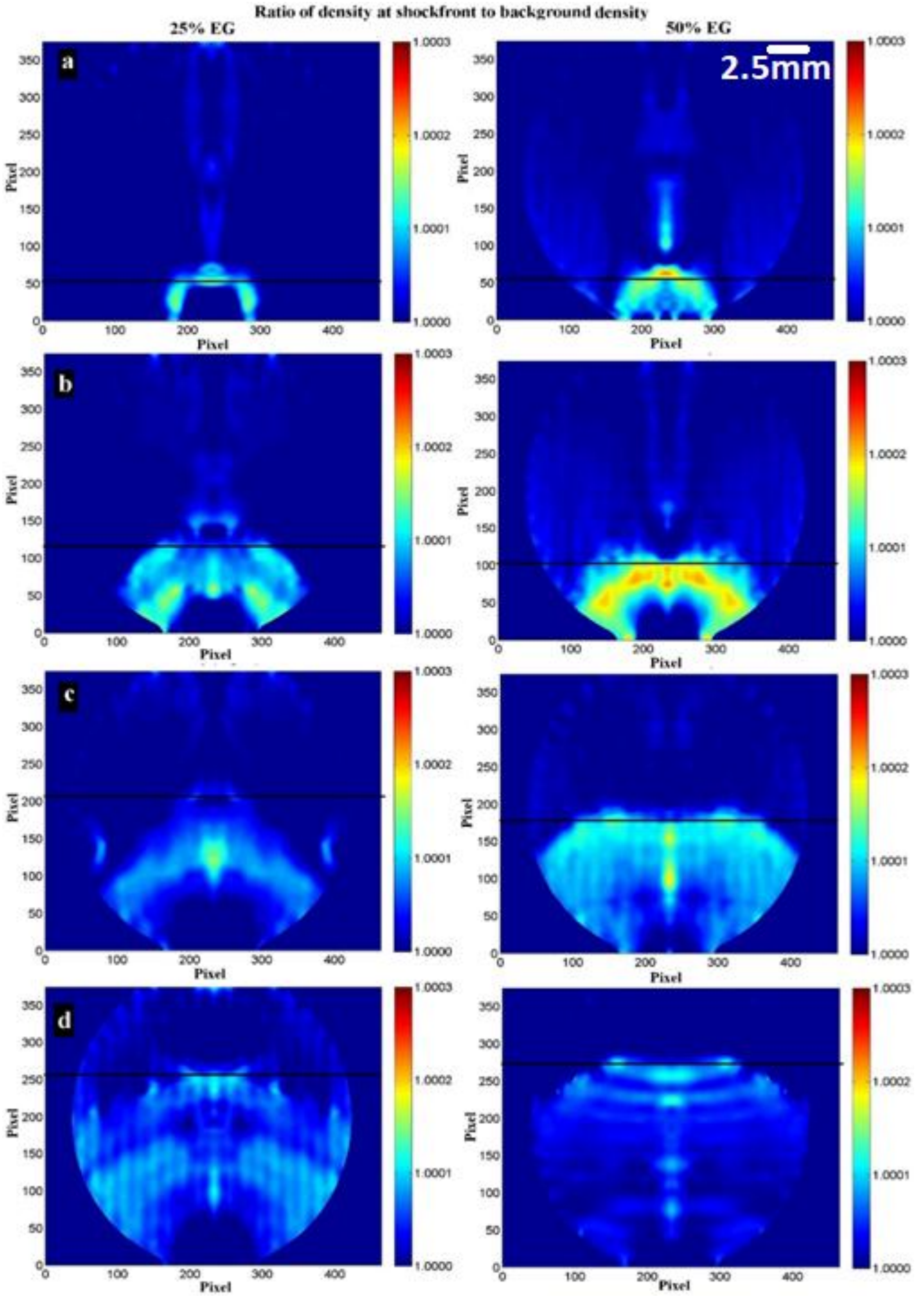

Figure 5.19: The ratio of the density of the medium to the background (unperturbed) density at the planes containing the shock front and perpendicular to the direction of ablating laser beam. Left panel is for 25% EG solution and the right panel is for 50% EG solution. One pixel corresponds to a physical dimension of 55 µm.

Figure 5.18. The shock front is clearly visible in these images as the region of high density. These high-density regions are seen to be propagating ahead with the passage of time. Also, it is seen that with the passage of time, the region over which the density is perturbed, increases. For an in-depth analysis of the temporal evolution of the shock front, the density

variations across the expansion axis along a given horizontal section have been plotted. This horizontal section has been so chosen that it passes through the region of maximum density perturbation. So, the horizontal section also advances with the passage of time. The plots have been shown in Figures 5.20 and 5.21 for 25% and 50% EG solutions, respectively. It is clearly seen from these figures that with the passage of time, the density at the shock front decreases and the energy gets spread out in the lateral direction, i.e. the region of impact is moving radially outward, like in the case of water.

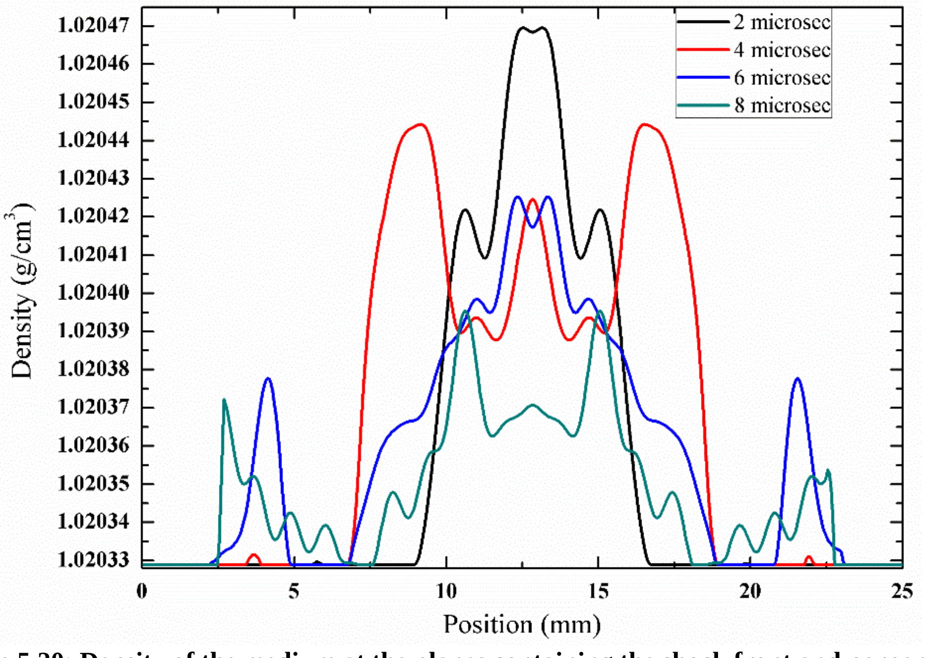

Figure 5.20: Density of the medium at the planes containing the shock front and perpendicular to the direction of ablating laser beam for 25% EG solution. Lateral position *x* = 12.5 mm represents the ablation site.

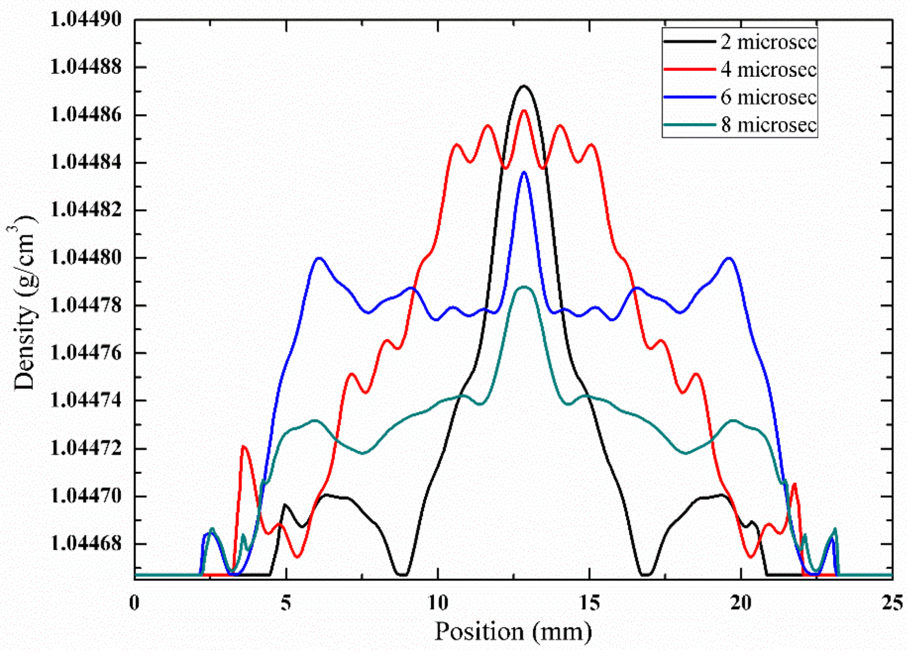

Figure 5.21: Density of the medium at the planes containing the shock front and perpendicular to the direction of ablating laser beam for 50% EG solution. Lateral position x = 12.5 mm represents the ablation site.

5.2.3. Multiple wavefronts in the medium

Unlike the case of gaseous medium, shock-induced mass density perturbations in liquid medium are spread over much wider region as seen in the experimental results discussed in the previous section. This observation is to be attributed to the multiple wave fronts that successively keep surfacing in the field of view after the formation of the primary shock front. As the laser pulse hits the target, rapid expansion of plasma plume leads to the formation of primary shock wave. At the same time, the laser pulse also initiates a stress wave that starts travelling in the target material, a phenomenon which has also been reported

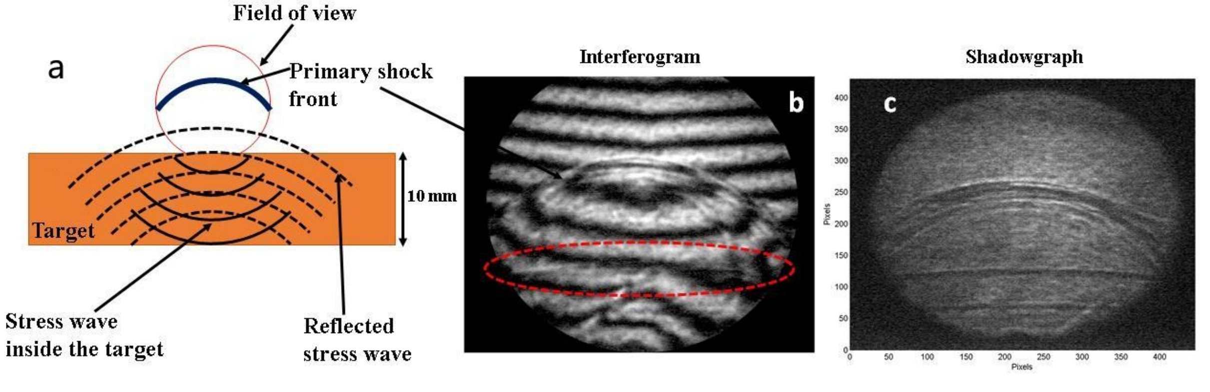

Figure 5.22: (a) schematic representation of the reflection of the stress wave (b) Interferogram image from water at 8 μs and (c) corresponding shadowgraph image

by several groups in the past, both experimentally as well as through numerical investigations [25, 81]. The stress wave inside the target gets reflected and transmitted at the target-medium interface, as shown schematically in Figure 5.22(a). Consequent upon the difference in the acoustic impedance of the two media, a process of successive reflection and transmission takes place leading to the emergence of multiple nearly flat wave fronts in the ambient medium.

The acoustic impedance for a medium is defined as $z_i = \rho_i v_i$, where ρ is the density of the medium and v is the velocity of sound in the medium. The suffix $i = 1 \; or \; 2$ which respectively denote the media on which the wave is incident and the media on the other side of the interface (in which the wave is transmitted or from which the wave is reflected). Owing to the fact that the reflected stress wave contains much lesser energy as compared to the primary shockwave, it is relatively weaker in strength. Therefore it is not very prominent in the recorded interferogram, as may be seen in Figure 5.22(b). This may also be understood by the fact that the amount of energy that will be transmitted to water ambient from the target surface will be approximately 13.4% (the relation between reflection coefficient R and the acoustic impedance z is, R= $(z_1\text{-}z_2/z_1+z_2)^2$) of the energy of the stress wave. To clearly observe these reflected waves, shadowgraph images were recorded under the same experimental conditions. A representative shadowgraph image has been shown in Figure 5.22(c) where the primary and reflected shock waves are clearly visible. In order to observe the evolution of these reflected waves, the shadowgraph images for water as the ambient environment (from $t = 2\;\mu s$ to $t = 12\;\mu s$) have been recorded and a few representative images have been shown in Figure 5.23.The primary shock front and the first reflected stress wave have been labeled in the images corresponding to $t = 5\;\mu s$ and $6\;\mu s$ (Figure 5.23) for clear understanding. The white arrows in the later instants depict the first one of the many advancing reflected stress waves. Also there are V-shaped waves present in the medium at the time instants of $t = 5$ and $6\;\mu s$ on the two sides of the evolving hemispherical shock. Similar observations have also been reported in the past [82, 150]. The velocity of these waves depends on the acoustic impedances of the target and the surrounding medium.

In order to confirm that the flat wave fronts that are visible are indeed the reflected stress waves in the medium, we have correlated the separation between the two consecutive flat wave fronts with the travel time of the sound wave in the target material. Given that the target material is copper, the velocity of sound is known to be 4600m/s and the average speed of shock in water is 1711m/s (as calculated from the shadowgraphs in the previous section). The temporal separation between the two consecutive reflected stress wave fronts calculated using these values is in very good agreement with the time taken by the stress wave to travel a round trip inside the target. This has also been confirmed by taking a target of different thickness. Therefore, it is reasonable to consider that the wider region under perturbation, as seen in the RI and also the mass density maps, is a resultant of the cumulative effect of the primary shock wave and the successively reflected stress waves. The position of the first reflected wavefront versus time plot gives the velocity of this front, which is equal to 1727m/s. This is consistent with the speed of shock wave in water that has been found and discussed in Section 5.2.1 earlier. Similar observations have been made with 25% (w/w) and 50% (w/w) solution of EG in water. Position-time graphs have been plotted for the first reflected shock front for all the cases and have been shown in Figure 5.24. Here the speed of the reflected waves comes out to be ~1856 m/s and 1925 m/s respectively for 25% and 50% EG solutions which is in close agreement with the values obtained from the data, reported in the previous section (Section 5.2.2).

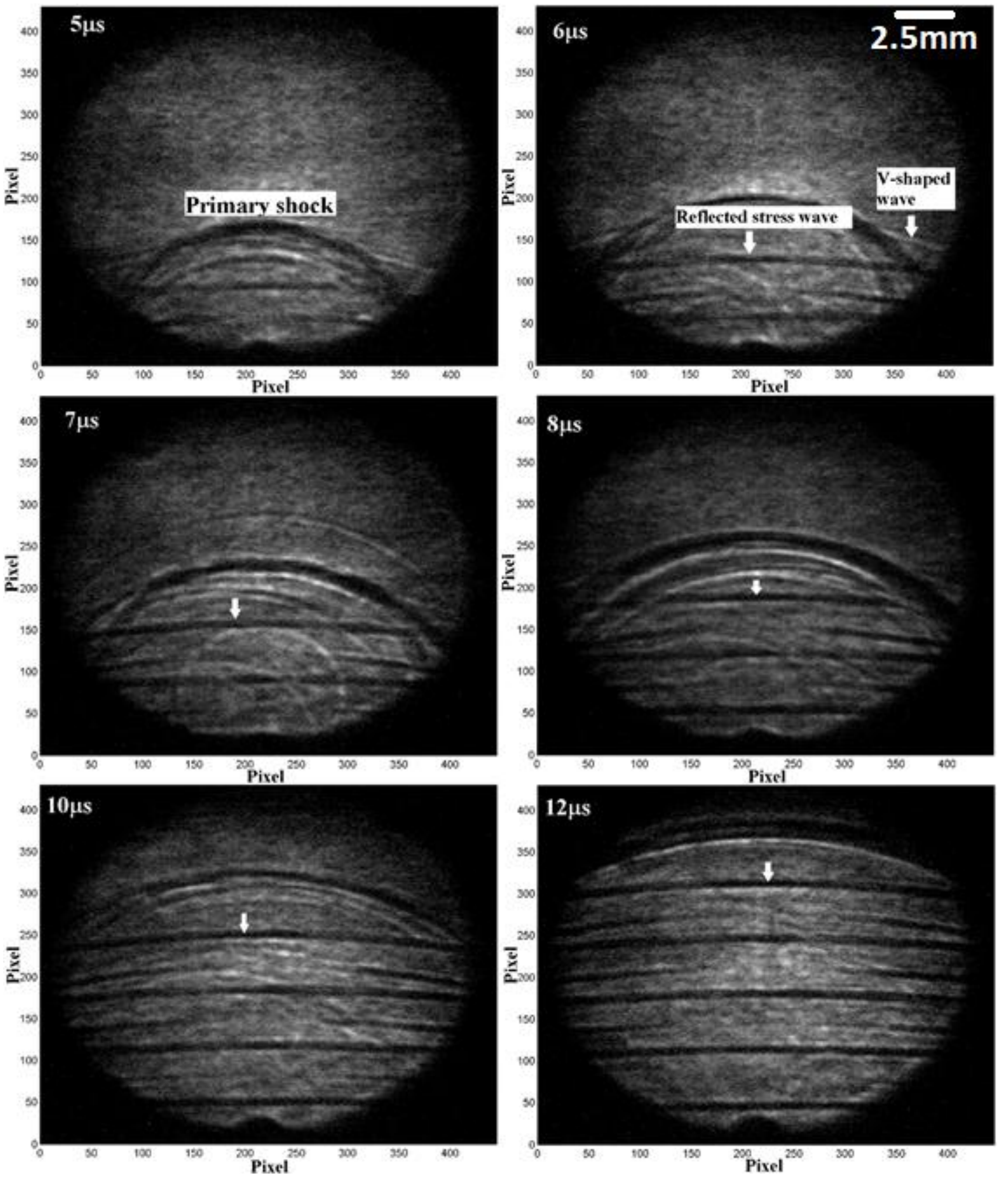

Figure 5.23: Shadowgraph images depicting primary and successively reflected shock fronts. One pixel corresponds to a physical dimension of 55 μm.

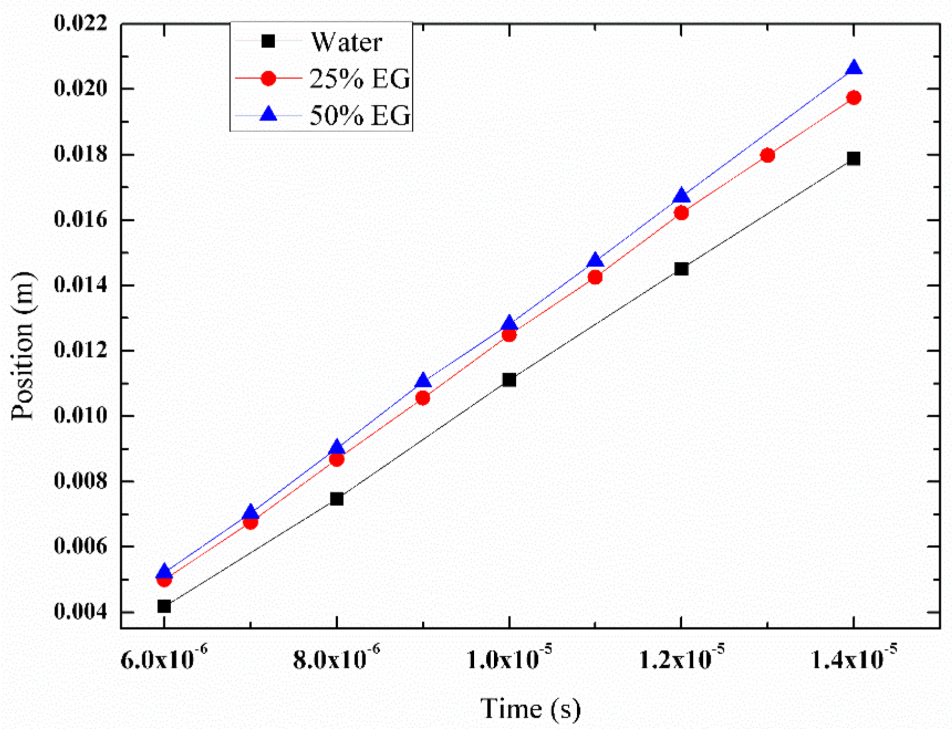

Figure 5.24: Position versus time graph for the first reflected shock front for water and aqueous solution of 25% and 50% EG.

5.2.4 Charge density in the plume

As discussed in Section 5.2.1, the regions which are just above the target surface and close to the point of ablation are dominated by the presence of plasma. The plasma comprises of both, positively charged ions as well as the electrons. In addition, there are some neutral particles as well. Both, the ions as well as the electrons contribute towards the change of refractive index. However, the relative contribution of electrons towards the changes in the refractive index field is significantly higher as compared to that of the ionic contribution [55, 58]. Therefore, the effective changes in the refractive index field (a net lowering of refractive index) are observed primarily due to the electronic charge in the regions close to the target surface (just above the point of ablation). This electronic charge density in this plasma plume region has been calculated from the corresponding RI values, which are essentially less than that of the ambient. This idea works well with gasses, but in the case of liquid, the metal and water vapor resulting from the ablation form a bubble, commonly known as the cavitation bubble, and it surrounds the plasma region. This bubble leads to significant amount of light scattering, leading to practically very less or no light passing through it. In the case of water, it was seen that the formation of bubble starts at around $t = 8\,\mu s$, but in the case of more viscous liquids it was observed at the time instants as early as $t = 4\,\mu s$. Therefore, it becomes difficult to observe the effects of charge once the bubble is formed. The dimension of the bubble is within a few mm for the temporal range over which the data has been recorded. This bubble gives the perception of a dark fringe which is misleading and hence may lead to the wrong estimate of charge density. Thus, here the discussions pertaining to the charge density distribution have been made only for $t = 2\ \mu s$ and $4\ \mu s$. For qualitative understanding, the representative charge density maps for water and 25%(w/w) EG have been shown in Figure 5.25 for two different instants of time.

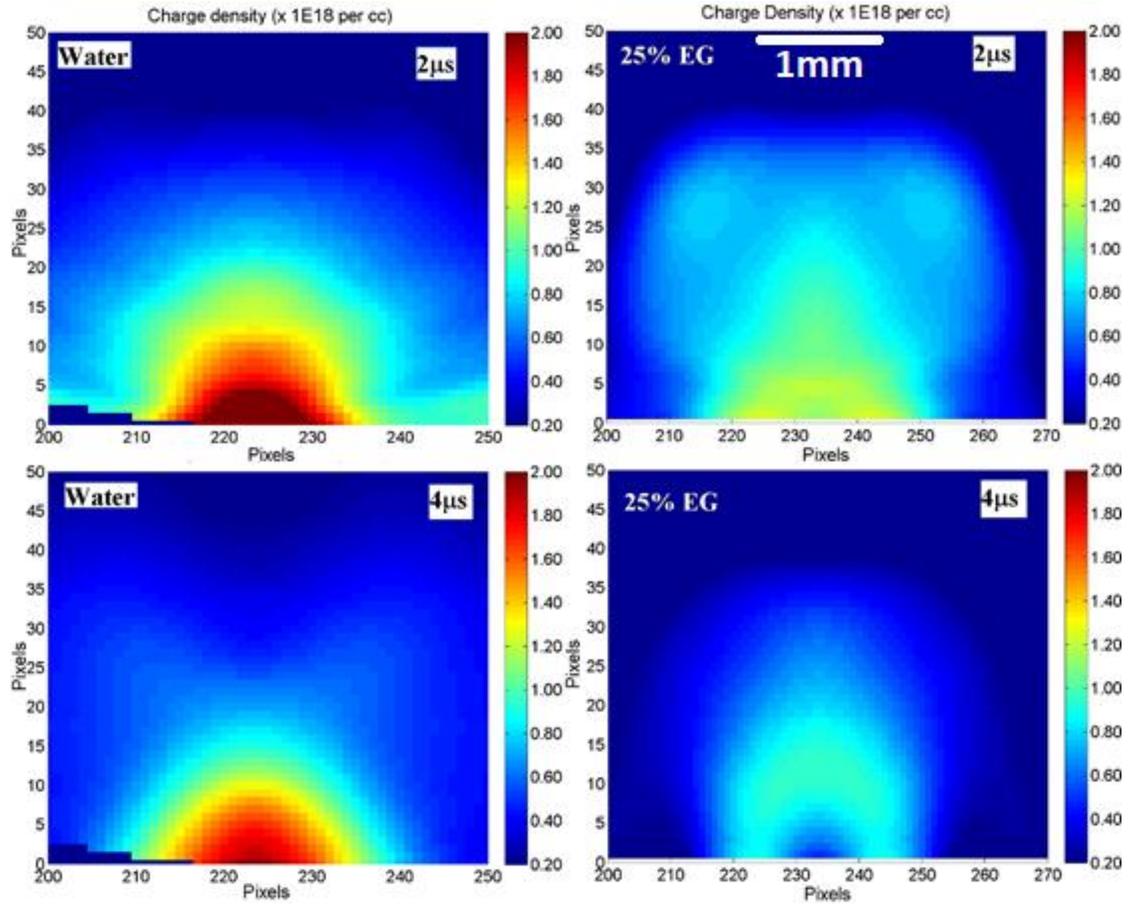

Figure 5.25: Charge density map in the plume region at 2μs and 4μs for water and aqueous solution of 25% EG. In the maps shown, one pixel corresponds to a physical dimension of 55 μm.

With reference to the data shown in Figure 5.25, a comparison of the charge density maps retrieved at two different time instants for water (left column) shows a significant reduction in the charge density of the plume over a period of 2 μs. Similar observations are also to be made from the charge density maps shown for 25% EG aqueous solutions (right column). These trends are expected since the charge in the plume region gets quenched with time and the plasma thermalizes. On the other hand, at any given time instant, $t = 4\ \mu s$ (say) the charge density in the plume for 25% EG solution is comparatively lower than that seen for the case of water (as may be seen in the top row of Figure 5.25). This trend of charge density is also seen in the maps corresponding to the time instant of $t = 4\ \mu s$ as well (bottom row). These differences in the charge density maps of the two liquids observed at any given time instant are to be attributed to the fact that in a medium of higher density, the plume thermalizes faster due to the increased number of collisions. Thus, for the same material and the same laser fluence, the charge density dies out faster in the medium with relatively higher density (the EG aqueous solution in the present case). Furthermore, the electron charge density maps shown in Figure 5.25 clearly reveal a decreasing trend in the charge density as one moves away from the target surface as well as with the passage of time. Similar trend is also to be seen along the radial direction wherein the charge density can be seen to be rapidly falling at any given instant of time.

For better clarity on the quantitative aspects, a comparison has been made between the charge distributions in the three media. The electronic charge density (determined following the assumption that the laser-produced plasma is not completely ionized) has been plotted as a function of the lateral dimension at a plane that has the maximum charge density (~0.55 mm above the ablation site). These plots have been shown in Figure 5.26. It is clearly seen from Figure 5.26 that at higher values of the density of the medium, the charge density is low in the plume region for the same instant of time. The observed reduction in the charge density with increase in the density of the medium may be attributed to the higher rates of collision of charges in the plume region because of the stronger confinement effects. This eventually leads to rapid thermalisation of plasma. Also, the charge density, for any liquid (water and/or EG solution), decreases with time, as is expected in the case of plume expansion.

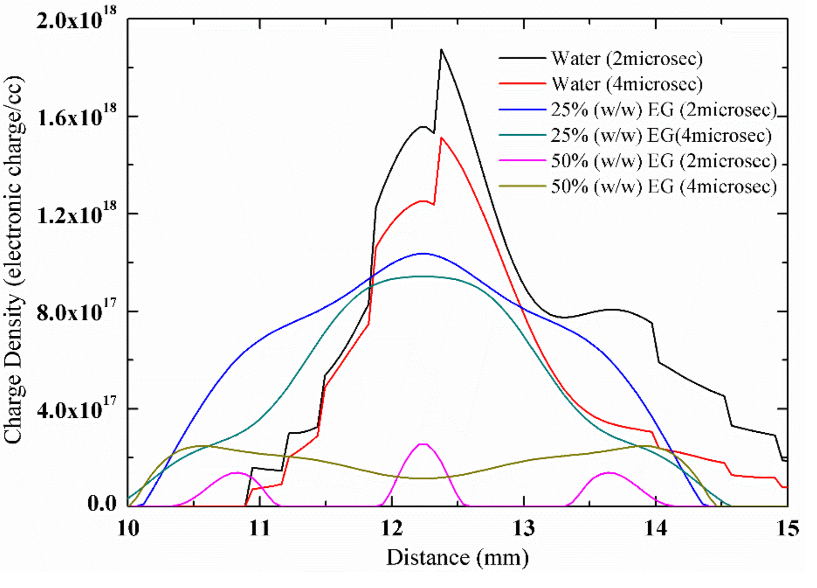

Figure 5.26: Charge density distribution as a function of lateral dimension in the plume region at 2μs and 4μs for water and aqueous solutions of 25% and 50% EG. x = 12.5 mm represents the ablation site.

Importance of the observations made on the basis of the interferometry-based experiments, as discussed above, can be understood by considering the fact that a range of theoretical studies present in literature suggest that the phenomenon of laser ablation in liquid (LAL) leads to the formation of metal vapor and subsequent condensation of the same. This stage of condensation leads to two competitive and coexisting processes, namely the nucleation (formation of nanocrystals) and nanoparticle growth (adhesion of metal vapor around the nucleation center). When the plume thermalizes rapidly, the nucleation process dominates and more number of particles are formed, which are smaller in size. On the contrary, if the process of thermalisation is relatively slow, it leads to the formation of bigger particles owing to the dominance of the crystal growth process over nucleation. Therefore, the dependence of the plasma life-time on the medium density is crucial from the point of view of monitoring the size control of the nanostructures resulting from ablation of metal in liquid media, a subject which forms the future scope of the present experimental work.

In conclusion, the observations suggest that the medium mass density perturbation results due to both, the primary shockwave as well as the reflected stress waves. It has been observed that the velocity of shock and reflected stress waves increase with the increment in the density of the ambient fluid medium. The results related to the charge density of the plume clearly show that the charge density in this region dies off faster in the medium of higher density.

5.3 Controlling the size distribution of nanoparticles through the use of physical boundaries during laser ablation in liquids

The results from the previous two sections reveal that the presence of physical barrier in the vicinity of the ablation site prolongs the lifetime of the plasma plume. Also, the plasma plume quenching depends on the density of the medium. The present sections deals with the experiments wherein the above observations have been exploited to develop one of the simple, yet effective method of controlling the size and size distribution of the metallic nanoparticles produced due to the process of laser ablation.

Details of the experimental setup and the methodology has been discussed in Chapter 3. Laser ablation in liquid (LAL) has been carried out with two different target materials immersed in different liquid ambient media under constant laser fluence and height of the liquid column. The as prepared suspensions carrying ablated nanoparticles have been scanned using SEM (*Zeiss-Merlin*). For the preparation of samples for SEM characterisation, a few drops of the suspension was dried over a cleaned Al foil, which was later put on the sample holder using a carbon tape. Before preparing the samples, the suspension was sonicated well to avoid agglomeration and ensure homogeneity. The SEM images were later analysed using image processing codes to retrieve the particle size distribution. To process the SEM images of Cu and Ti in water and IPA, image processing algorithm and the related code was written in MATLAB7. The images were first processed and filtered to render enhanced contrast between particles (foreground) and background. Depending on the quality of the images, manual and automatic contrast enhancement was carried out on images. Thereafter, considering the particles to be spherical in nature, Hough Transform (HT) was employed to detect the diameter of the circle considering 2D projection of 3D particles from their processed SEM images. The algorithm being computationally extensive, to detect the large number of particles in images with high particle density, same images were processed multiple times through the algorithm with smaller range in diameter distribution. Thereafter, diameters of particles obtained in pixel were converted into their physical dimensions from their respective scale bars. These particle sizes were then sorted for different ranges and the statistical distribution thus obtained was put in the form of histograms. A detailed discussion on the findings have been made in the next section under two headings, *viz.* the effect of physical boundaries in water ambient and the effect of boundaries in IPA ambient. Since the focus of the work is on the investigation of the presence of physical barrier on the size distribution of nanoparticles, the ambient media have been kept similar while analysing the data and hence this classification. The viscosities of water and IPA at 25^{0}C are 0.89 cP and 2.04 cP, respectively, significantly different from one-another [151]. The densities of water and IPA at 25^{0}C are 0.997 g/cm^3 and 0.786 g/cm^3 respectively. Copper and titanium have been chosen as target materials because they respond differently to the applied laser pulse [152]. The compositions of Cu and Ti nanoparticles formed in water and IPA ambient have been thoroughly reported and investigated by many researchers [99,153,154]. The refractive indices (RI) of Cu and Ti are significantly different at the ablation wavelength (1064 nm) and hence for any given liquid medium, these materials exhibit appreciable differences in their reflectivity and transmissivity. The values of refractive indices have been tabulated below in Table 5.1 [151]. The corresponding reflectivity values derived from these RI values have been tabulated in Table 5.2.

Table 5.1: Refractive indices of the target materials and ambient liquids

Material	Copper	Titanium	Water	IPA
RI	0.37861	3.4654	1.332	1.3514

Table 5.2: Reflectivity values at the interfaces

	Copper	Titanium
Water	0.310627	0.197757
IPA	0.316185	0.192616

Primary findings of the laser ablation experiments conducted with two target materials immersed in liquid media have been discussed in this section. Results have been categorized primarily into two different sections; the first section (Section 5.3.1) discusses the effects of the presence of confining boundaries when the target is kept in water ambient, while the observations made with IPA as the liquid environment have been presented in the second subsection (Section 5.3.2). For each liquid medium, the experiments have been conducted with two types of target materials i.e. copper and titanium.

5.3.1 Experiments in water ambient

It has been established by the researchers that the size of the nanoparticles produced by the method of laser ablation depends on a range of parameters that include laser fluence, ambient medium, physical properties of the target material etc. Effect of many of these parameters on the size distribution of the nanoparticles have been investigated by various researchers in the past, both, experimentally as well as theoretically [18, 61, 103, 152, 155]. In the present discussion, all such parameters (e.g. laser fluence, ambient medium etc.) have been maintained constant for each set of experiments conducted such that any change occurring due to the presence of physical barriers may be clearly seen. Thus, the changes that are observed in the sizes and size distribution of nanoparticles produced due to laser ablation can be attributed to the role played by the presence of physical barriers on the target surface.

Under these conditions, the laser ablation has been carried out on the target surface that is either flat (no physical barrier) or is confined by the physical boundaries (walls) on both the sides of the point of laser ablation. Following the methodology discussed in the previous section, samples in the form of suspensions of nanoparticles have been subjected to SEM analysis and the corresponding SEM images have been shown in Figures 5.27 and 5.28. SEM images for copper targets, both flat as well as that fitted with confining walls and the corresponding plots for size distribution of the particles have been shown Figure 5.27. The same studies have been carried out with titanium as the target material and the results have been shown in Figure 5.28. In both the figures, the subfigures (a) show the SEM images of the nanoparticles produced due to the ablation of the flat target plate (without barriers), while the subfigures (c) correspond to the case of copper (Figure 5.27(c)) and titanium (Figure 5.28(c)) target plates with confining walls. The subfigures (b) and (d) are the particle size distribution plots. The SEM images shown have been quantified and the results have been

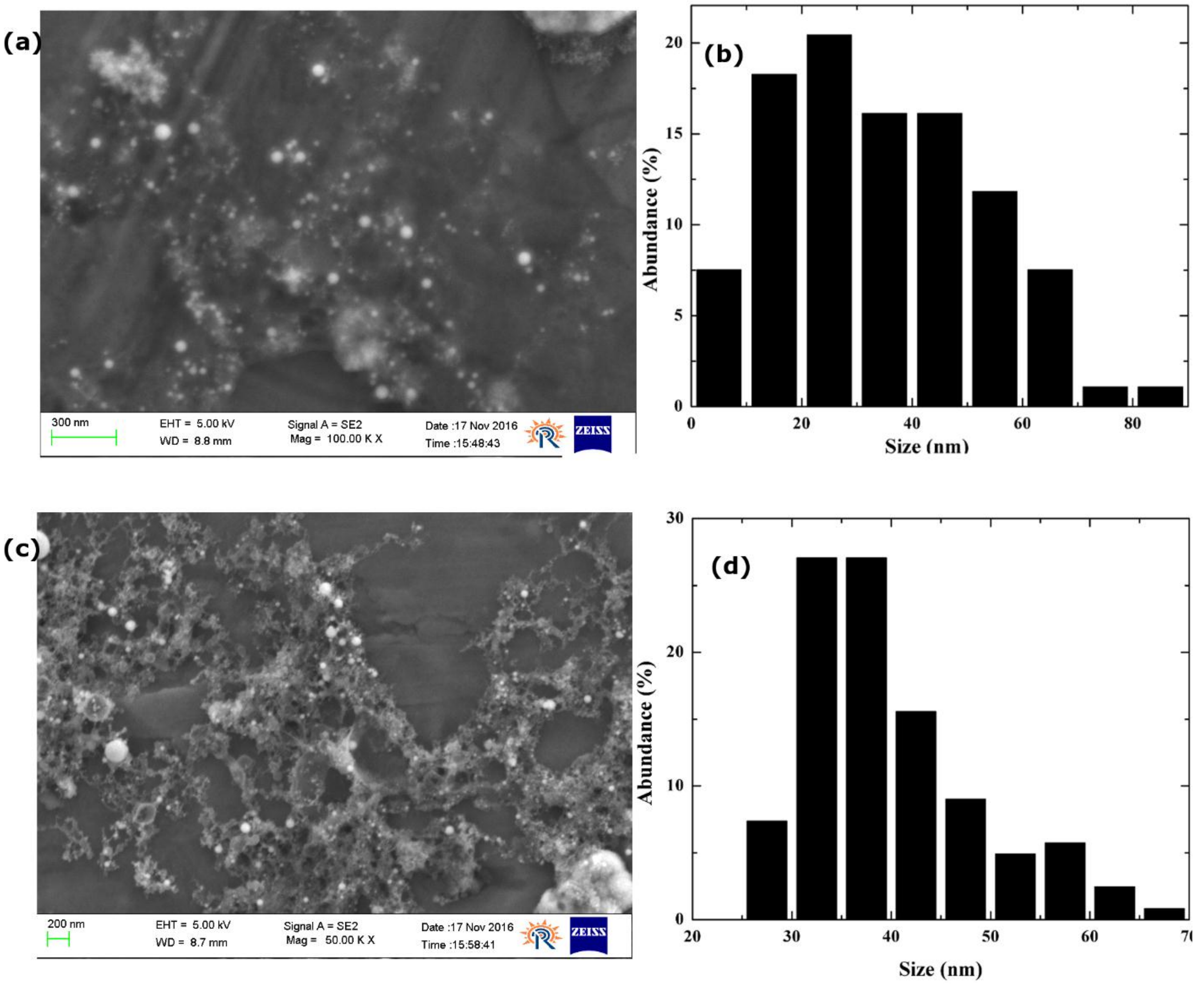

Figure 5.27: SEM micrographs of the nanoparticles produced as a result of ablation of a flat copper target (a) and copper target fitted with confining physical boundaries (c). Corresponding size-distributions of the resultant nanoparticles have been presented in (b) and (d). (Ambient liquid medium: water)

presented in the form of the size distribution plots in Figure 5.27 (b) and (d) (for copper target in water) and Figure 5.28 (b) and (d) (for titanium target in water). These size-distribution plots clearly highlight the possible influence of the confining boundaries in the form that, for any given target material type, the average size of the nanoparticles produced due to the ablation of the flat plate is relatively smaller than that achieved in the case of target surface fitted with physical boundaries. These observations have been quantified in terms of the mean size of the nanoparticles produced with water environment and summarised in Table 5.3. It is to be seen from the table that, for any target material the size of the most abundant nanoparticles is consistently higher in the case of the ablation target fitted with the physical boundaries as compared to the flat of the flat target. For instance, a percentage increase of nearly 66% in the mean size of the copper-based nanoparticles is to be seen as the flat (open) target is replaced by the one fitted with the physical boundaries. Similar trends is to be observed in the case of titanium substrate, though the percentage increase in the mean size of

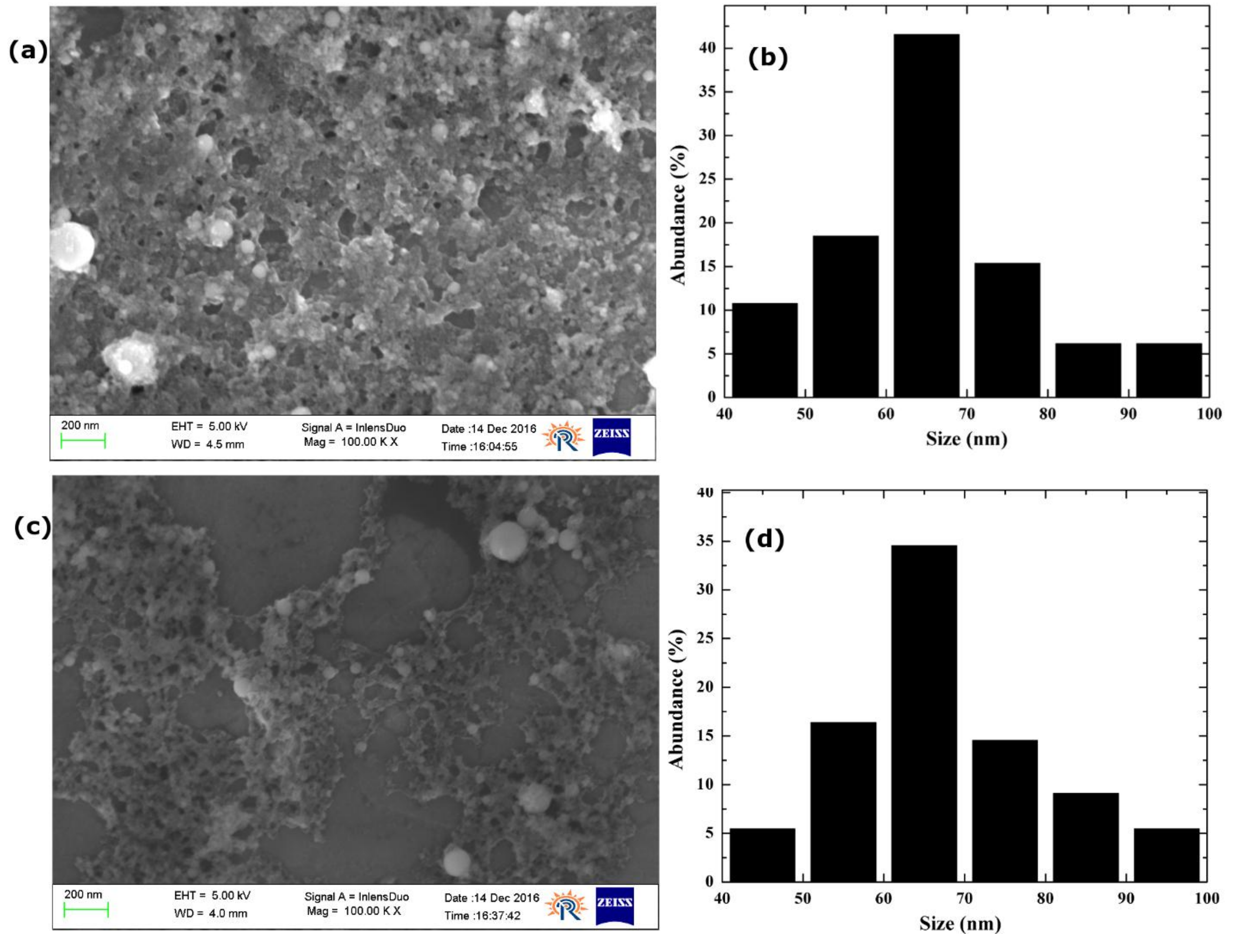

Figure 5.28: SEM micrographs of the nanoparticles produced as a result of ablation of a flat titanium target (a) and titanium target fitted with confining physical boundaries (c). Corresponding size-distributions of the resultant nanoparticles have been presented in (b) and (d). (Ambient liquid medium: water)

the nanoparticles is not as significant as was observed with copper as the target material and here the increase in the nanoparticle size is restricted to ≈ 17.5%.

Table 5.3: Comparison of the mean size of the nanoparticles produced with flat target to those obtained with the target fitted with physical boundaries (Ambient liquid medium: water)

Material	Mean size of nanoparticles		% Increment
	Flat Target	Target with boundary	
Copper	25.5 nm	42.4 nm	66
Titanium	67.6 nm	79.4 nm	17.5

The above observations made in the form of increase in the mean size of the nanoparticles produced with target fitted with physical boundaries may be explained on the basis of the rate at which the thermalisation of the plasma plume takes place. It has been well documented in the available literature that the process of formation of metal nanoparticles by laser ablation takes place due to the thermalisation of the plume. Thus, the rate at which the plasma plume cools down plays an important role in this entire process [156]. A very high cooling rate of the plasma plume is expected to result into smaller size of the nanoparticles produced. This is owing to the fact that the formation mechanism of nanoparticles after the completion of the ablation process depends on two co-occurring processes, namely, nucleation and particle growth. The nucleation process starts as soon as the ablated species come together, followed by the coalescence of these nuclei that in turn leads to the formation of bigger particles. If the thermalisation is fast enough, the nucleation process dominates, leading to the formation of smaller nanoparticles. On the other hand, if the plume lifetime is longer, i.e. if the process of thermalisation takes place over a longer period of time, the nuclei produced as a result of material ablation get enough time to come closer and form bigger particles. In the context of the present work, the presence of the physical boundaries (Al walls), on either sides of the ablation site on the target surface, leads to the reflection of the shockwaves towards the site of laser ablation, thereby compressing the ambient medium. The subsequent increase in the pressure leads to a longer plasma thermalisation time, which causes the enhancement in the sizes of the nanoparticles [156, 157].

Another interesting observation that is to be made from Figures 5.26 and 5.27 is in the form of the larger mean size of the titanium nanoparticles in comparison to that achieved with copper as the target material for any given configuration. The observed differences are to be attributed to the relative differences in the refractive indices of these two materials. Thus, for the given ablation wavelength (1064 nm) employed in the present set of experiments, the absorption coefficients of the two target materials are expected to be different. Due to the differences in the absorption coefficients, the fraction of the total energy of the incident laser pulse that causes the ablation of the target material will be different and hence the extent of ablation. This is because, the amount of mass ejected and the temperature of the plasma will be different for the two materials[10].

5.3.2 Experiments in IPA ambient

Observations made on the possible effects of the confining boundaries on the resultant sizes of the nanoparticles produced in isopropyl alcohol (IPA)-based liquid medium have now been presented and discussed. Figures 5.29 and 5.30 respectively show the SEM images and the respective particle size distributions due to the laser ablation of copper and titanium target surfaces immersed in IPA ambient. Subfigures (a) and (c) in both the figures respectively show the SEM images of the nanoparticles formed with flat target (a) and target fitted with physical boundaries (c). The respective particle size distributions of the produced nanoparticles have been shown in subfigures (b) and (d). Irrespective of the material of the target plate, smaller sized nanoparticles are to be observed in the case of the flat targets while the nanoparticles are relatively bigger in size when produced with confining walls placed on the target surfaces. These results follow the similar trend as was observed in the case of water as the liquid ambient medium presented in the previous section. However, a closer observation of the mean size of the nanoparticles summarised in Table 5.4 reveals that the copper nanoparticles produced under IPA liquid ambient are relatively larger in size as compared to their counterparts obtained with water as the ambient liquid medium (Row 1 of Table 5.3). On the other hand, the IPA ambient-based titanium nanoparticles are smaller in size in comparison with the size of the titanium nanoparticles produced with water as the liquid medium (Row 2 of Table 5.3). These differences may be attributed to the difference in the thermo-physical properties of the two target materials considered in the present set of experiments [152].

[10] It is pertinent to note here that factors such as electron-phonon coupling strength, surface energy, melting and boiling point of the material etc. may also influence the size and the size distribution and may contribute towards the observed differences in the produced nanoparticles [152]. However, the primary findings of the present experiments have consistently revealed the plausible role(s) of the confining physical boundaries in increasing the mean size of the nanoparticles produced as a result of laser ablation of the target material (copper and titanium).

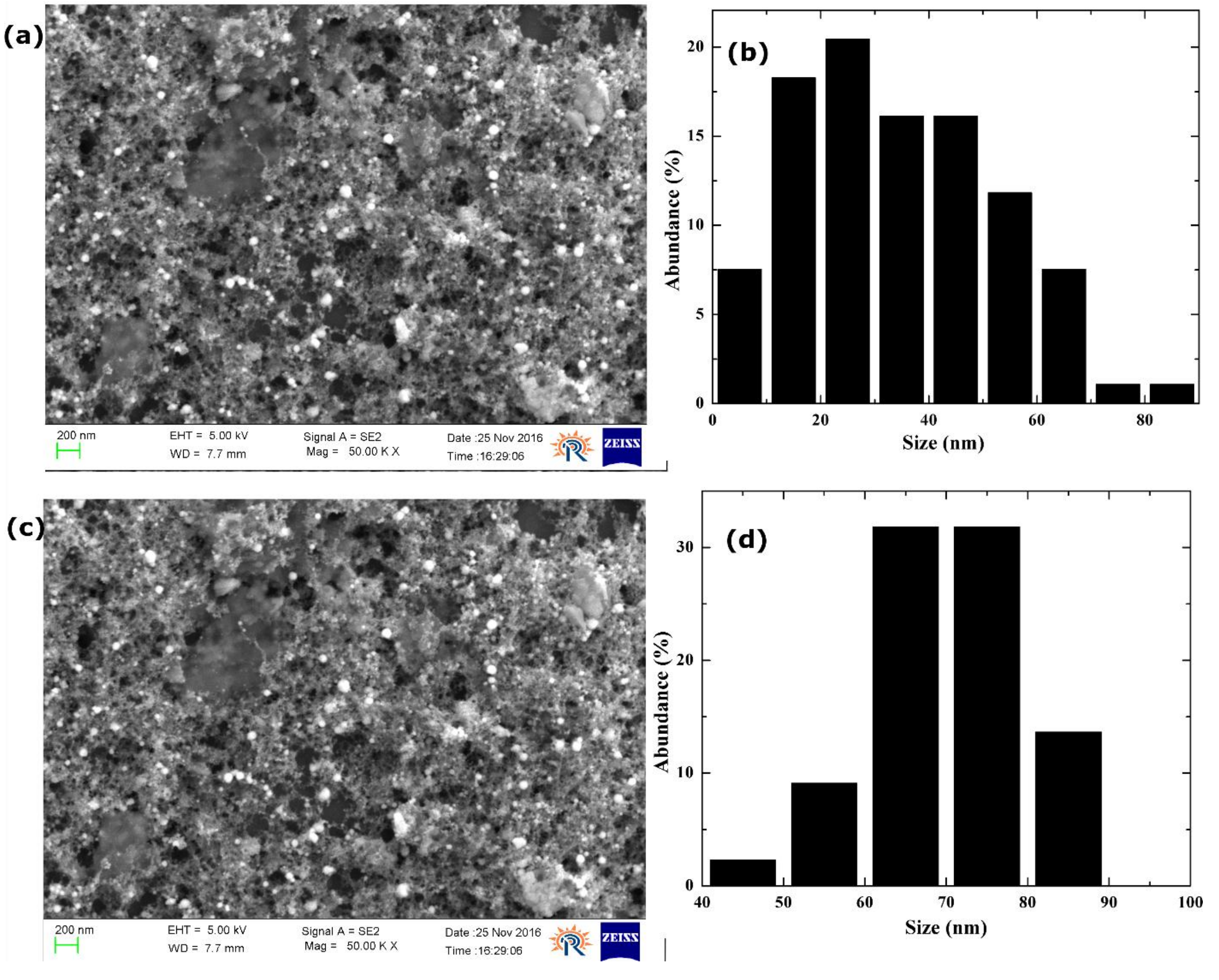

Figure 5.29: SEM micrographs of the nanoparticles produced as a result of ablation of a flat copper target (a) and copper target fitted with confining physical boundaries (c). Corresponding size-distributions of the resultant nanoparticles have been presented in (b) and (d). (Ambient liquid medium: IPA)

Also, a comparison of the mean particle sizes for the two materials presented in Tables 5.3 and 5.4 shows that in any given liquid ambient the difference in the size of copper nanoparticles produced from flat target and walled target is much higher as compared to that observed in the case of titanium nanoparticles produced under similar conditions. Such a trend may be attributed to the differences in the initial plasma temperatures of the two target materials and the amount of mass ejected per shot for a given set of operating parameters maintained during the course of experimental runtime.

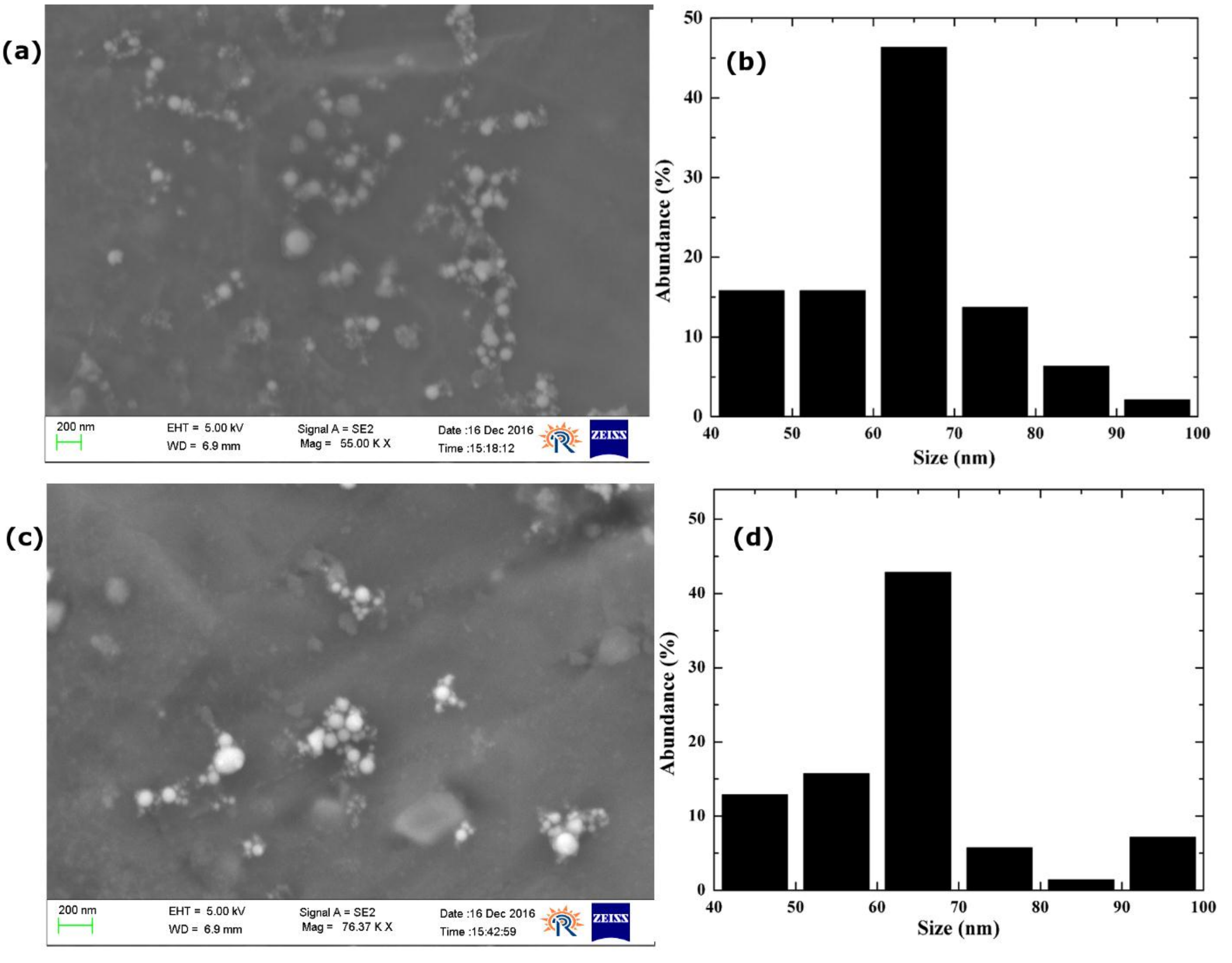

Figure 5.30: SEM micrographs of the nanoparticles produced as a result of ablation of a flat titanium target (a) and titanium target fitted with confining physical boundaries (c). Corresponding size-distributions of the resultant nanoparticles have been presented in (b) and (d). (Ambient liquid medium: IPA)

Table 5.4: Comparison of the mean size of the nanoparticles produced with flat target to those obtained with the target fitted with physical boundaries (Ambient liquid medium: IPA)

Material			% Increment
	Flat target	Target with boundary	
Copper	34.5 nm	76.3 nm	121
Titanium	63.9 nm	70.6 nm	10.5

Results of the various experiments presented in the above two sections reveal that the changes in the size of the nanoparticles (as one goes from the flat target to the ones fitted with physical boundaries) is significantly more appreciable in the case of copper target material as compared to those observed with titanium target. On the other hand, the particle size distribution is found to be sharper in the case of titanium-based target. This observation may be attributed to the large difference in the thermal conductivities of copper (3.98 $Wcm^{-1}K^{-1}$) and titanium (0.22 $Wcm^{-1}K^{-1}$) target materials. Owing to the relatively lower thermal conductivity of titanium the amount of thermal energy produced due to laser ablation remains localized in a smaller spatial domain and hence the mass ablated per shot is expected to be more as compared to that in copper and hence an increment in the resulting particle size is to be expected in the case of titanium-based target material. It is pertinent to mention here that one may explain these trends (resultant particle size distributions) on the basis of parameters, like surface energy, electron-phonon coupling strength etc. as well. However, the primary findings of the present experimental work have clearly identified the plausible roles of the presence of physical boundaries on either sides of the ablation site in deciding the size and the size distribution of the nanoparticles produced due to the laser ablation of the target material(s) placed in two different liquid media.

. The experiments revealed that for any given liquid medium as well as well as irrespective of the target material, the mean size of the nanoparticles obtained due to the ablation of the target plate fitted with confining boundaries is consistently higher than that achieved due to the ablation of the flat target materials. Furthermore, a comparison of the mean particles sizes obtained with the two materials revealed that in any liquid medium, the difference in the size of copper nanoparticles produced from flat and walled targets was much higher and sharper as compared to that observed in the case of titanium nanoparticles produced under similar experimental conditions. The observed increase in the size of the nanoparticles in the presence of the confining boundaries was primarily attributed to the prolonged thermalisation of the plasma plume (due to the reflection of the shockwaves).

Chapter 6: Conclusions and Scope of Future Work

6.1. Conclusions

Experimental studies concerned with the investigation of the phenomena of laser produced plasma-induced shockwaves in media of different densities were reported in the present thesis. The experimental measurements were performed in a purely non-intrusive manner using one of the refractive index-based imaging techniques, namely laser interferometry. Classical MZI coupled with an ICCD camera, was employed to record the fast transients associated with the shockwave phenomena. A high power ND:YAG laser was employed to achieve the ablation of metallic targets placed in media of different densities. The working media included air, water and aqueous solutions of ethylene glycol (25% and 50% w/w). Potential of placing confining physical boundaries on either sides of the ablation point as one of the effective ways of controlling the size and size distribution of nanostructures (produced as a result of laser ablation of metallic targets made up of copper or titanium) was explored and successfully demonstrated. Primary findings of the range of experiments conducted as part of the present work have been summarised below.

The propagation of shockwave in any given medium causes transient density perturbations. Although these perturbations are very short-lived (few microseconds), yet they have the ability to affect the processes that occur post ablation. For this reason the present work explored the effects of transient density jumps on the medium. It was found that the shockwave compresses the medium considerably causing the creation of a high density shockfront, which propagates in the medium. The axial rate of expansion of such a shockfront is higher compared to off-axial rate (i.e. lateral), leading to rapid energy loss in the axial direction as compared to the off-axial direction. Therefore, as the time progresses, the energy of the shock spreads out more towards the sides than the center of the shock. Perturbed medium density profile (due to propagation of shock waves) as well as shape and electron density of the plasma plume is significantly different in confined geometry in comparison to that observed in the absence of any physical boundary on the target material. Strong confinement of the plasma plume and hence an increase of the electron density is observed in the confined geometry. It was observed that the compression of medium is more in the case of lateral confinement when compared to that in the case of longitudinal confinement. Also, this compression of the medium due to the reflected shockwave alters the lifetime of the plasma plume. It was clearly evident from the experimental results that the reflection of shockwave from the physical barrier lengthens the lifetime of the plasma plume and hence it is expected to be crucial from the point of view of all the processes that result from the thermalisation of plasma, like, pulsed laser deposition, formation of nanoparticles etc.

In the case of liquid media, it was interesting to observe that the shockwave dies out faster in a medium of higher density as compared to a medium of lower density. The perturbation of the ambient medium (mass) density was found to be spread over a wider region in liquids, in contrast to the observed sharp shock boundary in the case of air. This is due to the combined effect of the primary shock waves and the successively emerging stress waves that result due to the multiple reflections from within the target surface. It was observed that the increase in the medium density speeds up the thermalisation of plasma and hence leads to a considerable reduction in the charge density in the plume region. Primary findings of the present interferometry-based experiments suggested that the medium density affects the way in which the mass density gets perturbed, an observation that holds importance in a range of practical applications of the phenomenon of laser ablation in liquid.

The plausible control on the size and size distribution of the nanoparticles produced as a result of ablation of metallic target material using confining physical boundaries on either side of the ablation site was experimentally demonstrated. Experiments were performed with copper and titanium target materials with two different ambient liquid medium of water and isopropyl alcohol (IPA). The study clearly highlighted the potential of employing physical boundaries in manipulating the sizes and size distributions of the produced nanoparticles. The experiments revealed that for any given liquid medium as well as for any given target material, the mean size of the nanoparticles obtained due to the ablation of the target plate fitted with confining boundaries is consistently higher than that achieved due to the ablation of the flat target materials (without confining boundaries). Furthermore, a comparison of the mean particles sizes obtained with the two materials revealed that in any liquid medium, the difference in the size of copper nanoparticles produced from flat and walled targets was much higher and sharper as compared to that observed in the case of titanium nanoparticles produced under similar experimental conditions. The observed increase in the size of the nanoparticles in the presence of the confining boundaries was primarily attributed to the prolonged thermalisation of the plasma plume (due to the reflection of the shockwaves). Taking into account the inherent advantages of the proposed methodology over the other conventionally employed techniques (e.g. wet chemical methods), the usage of the physical boundaries on either side of the ablation site presents a novel, yet one of the simpler and greener, ways of controlling the size and size distributions of the produced nanoparticles.

6.2. Scope of Future Work

The experimental work reported in the present thesis brought out some interesting observations pertaining to the characteristics of laser produced plasma-induced shockwaves in medium of different densities. Real time interferometric measurements clearly revealed the strong influence of confining physical boundaries (placed in the vicinity of the ablation site) on thermalisation time of the plasma plume and its impact on the size and size distribution of the resultant nanostructures produced due to the laser ablation of target material in liquids. The potential of the present work may further be explored in the following future directions:

1. Application of electric field assisted laser ablation in liquid (EFLAL) technique in controlling the size as well as shapes of the nanostructures. An attempt has been made as part of the present work and has been presented in the form of Appendix – II.
2. Conduct laser ablation experiments in liquid media of different densities, viscosities and/or permittivity to understand their influence on the shape, size and morphology of the produced nanostructures.
3. Extension of the interferometric measurements reported in the present work into the third dimension using the principles of optical tomography.
4. Thermal characterisation of nanoparticles/nanostructures produced as a result of laser ablation of metallic targets in liquids and their potential applications in the heat transfer studies and other areas of scientific and/or technological interests.

Appendix – I: Phase calculation in an MZI

The process of formation of interference fringes in case of an MZI has been discussed here in this appendix. When an MZI is set for the infinite fringe mode, one of the detectors records a maxima while the other records a minima of intensity. This is due to the fact that the beams reaching one of the detectors interfere constructively while those reaching the other detector interfere destructively. This is because of the phase difference of π between the two beams. The ray diagram of an MZI has been shown in the Figure A-I-1. BS-1 and 2 are the beam splitters with their coated surfaces to the left. M-1 and 2 are the two plain mirrors. D and D' are the two detectors. Here Beam - 1 and 2 represent the two beams that have been derived from a single beam incident on a beam splitter (BS-1).

The MZI set for infinite fringe mode has a square or rectangular geometry with two beam splitters sit at two diagonally opposite positions and two mirrors sit on the other two diagonally opposite positions (as shown in Figure A-I-1). The two optical paths therefore have same length l.The optical path for a single pass through any of the beam splitters is μt.

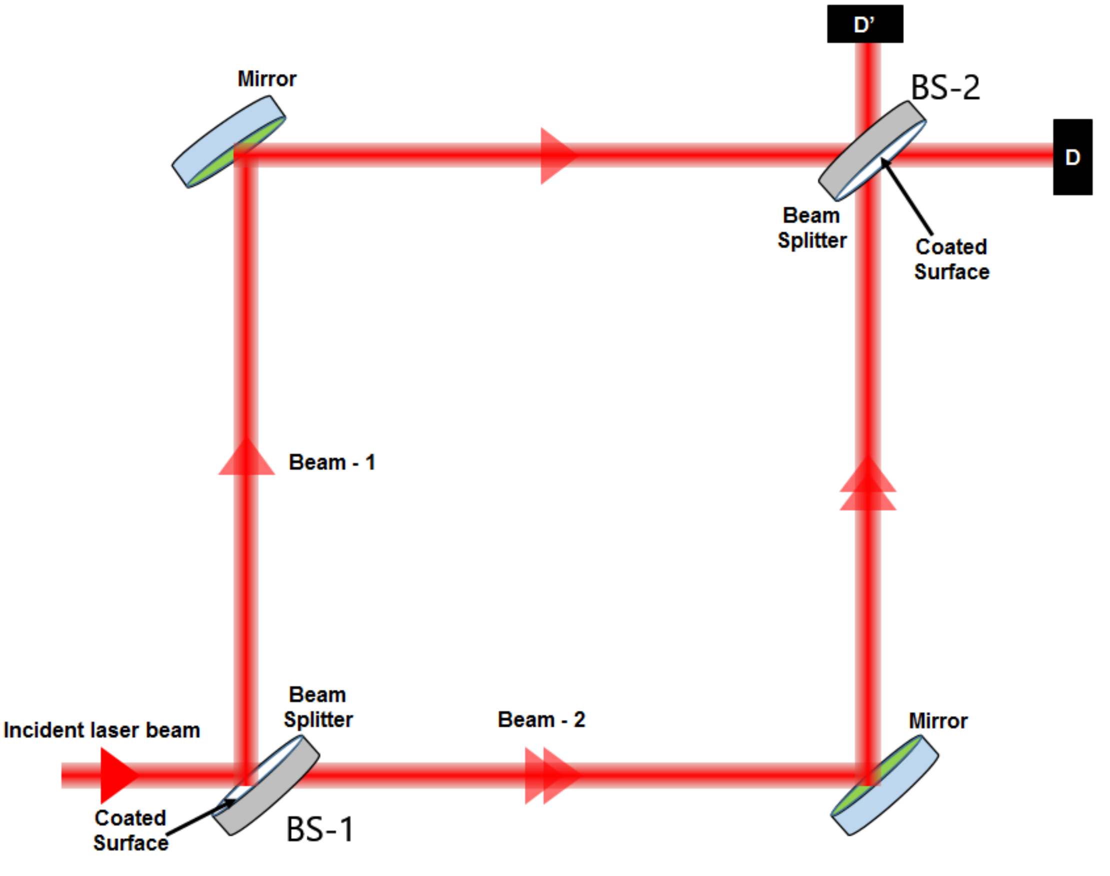

Figure A-I-1: Ray diagram for an MZI

Here μ is the RI of the material of the beam splitter and t is the physical path length. With these considerations we have calculated the path difference accumulated by each beam on each of the detector. The phase difference of π will arise on every reflection.

Phase of beam 1 at detector D:

$$\phi_{1-D} = 2\pi + \frac{2\pi}{\lambda}(l + \mu t) \qquad \text{(A-I-1)}$$

Phase of beam 2 to detector D:

$$\phi_{2-D} = 2\pi + \frac{2\pi}{\lambda}(l + \mu t) \qquad \text{(A-I-2)}$$

Phase of beam 1 at detector D' :

$$\phi_{1-D'} = 2\pi + \frac{2\pi}{\lambda}(l + 2\mu t) \qquad \text{(A-I-3)}$$

Phase of beam 2 to detector D':

$$\phi_{2-D'} = \pi + \frac{2\pi}{\lambda}(l + 2\mu t) \qquad \text{(A-I-4)}$$

Looking at Equation A-I-3 and A-I-4, it seems that a phase change of π has been missed, but a careful observation reveals that the beam splitter BS-2 has a coating on the right surface, which means that the beam 1 getting reflected from it is actually getting reflected from a glass-air interface (and not an air-glass interface like all other beams) leading to no abrupt phase change. For a better clarity of understanding the two beam paths have been separately shown in Figure A-I-2.

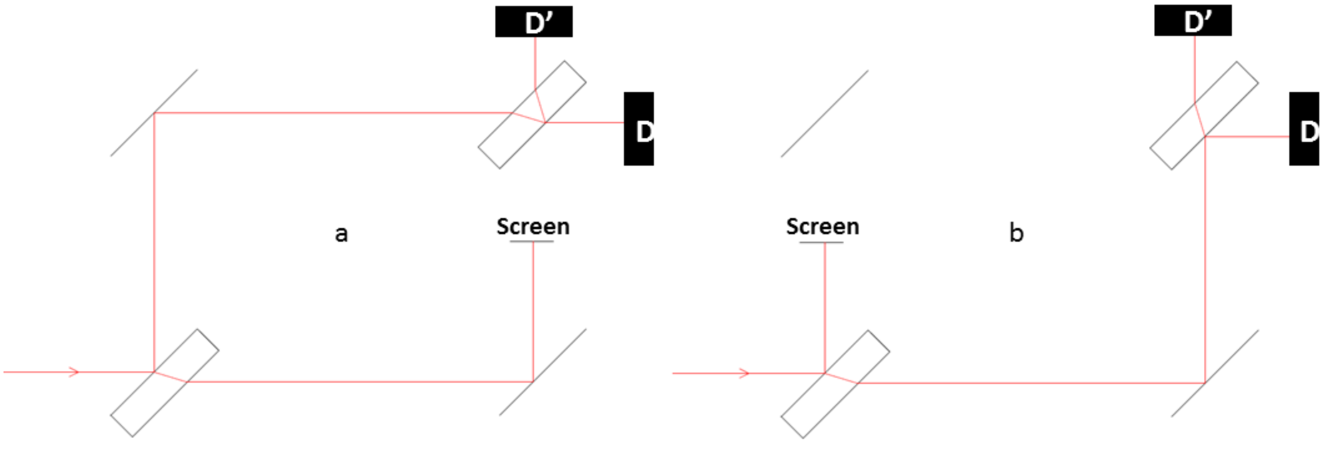

Figure A-I-2: (a) Ray diagram for beam 1 and (b) ray diagram for beam 2. The reflection that beam 1 undergoes at the beam splitter close to the detector does not causes an abrupt phase change because the reflection is from glass-air interface

The phase difference at the detector D;

$$\varphi_D = \phi_{1-D} - \phi_{2-D} = 0$$

The phase difference at the detector D';

$\varphi_{D\prime} = \phi_{1-D\prime} - \phi_{2-D'} = \pi$

The above calculation clearly shows that there is a phase difference of π between the beams reaching the two detectors. This means if there is constructive interference at one of the detectors, there has to be destructive interference at the other. This condition is best realised in the infinite fringe setting with the one of the fields of view completely bright and the other completely dark. Here it is to be noted that the placement of beam splitter (i.e. putting the coated side on left or right) is purely voluntary and no matter how it is put this difference will be there. This is also in concert with the fundamental definition of interference, according to which, interference is nothing but redistribution of energy in the medium. If one assumes that there is an abrupt phase difference in the beam getting reflected from any interface then it will result in zero phase difference or into a phase difference of 2π between the two detectors leading to constructive or destructive interference on both of the detectors, simultaneously. In that case it will be difficult to justify the excess of energy (constructive interference on both the detectors) or the loss of energy (constructive interference on both the detectors) in the existing framework of physics.

Appendix – II: Electric field assisted laser ablation in liquid

In the present thesis, a detailed discussion has been presented on the effect of the presence of physical barriers in the vicinity of the ablation site. It has been shown that the presence of physical barriers on either side of the ablation site causes changes in the thermalisation time of the plasma plume and hence, has plausible effects on the size and size distribution of the nanoparticles that are produced. This method is expected to yield size controlled nanoparticles in the case of ablation of metallic targets immersed in liquid medium with pulsed laser source. However, this simplistic method cannot be employed if one needs to produce nanostructures of different shapes. Conventionally, the most effective methods for controlling shape of nanostructures is by means of using appropriate capping agent and by controlling the reaction environment appropriately [41–43]. The idea of shape control may also be seen as a directed growth or growth along a preferred direction. This is achieved by using a specific capping agent that arrests the growth of crystals (forming the nanostructures) along particular crystallographic plane(s) and hence shifting the aspect ratio of the resulting nanostructure to values higher than unity. Researchers have also been able to synthesise core-shell and dendritic nanostructures, which are more complex than nanorods, nanocubes, spindles etc. [43].

It is important to mention that the size control strategy that is used in the case of laser ablation-based nanoparticle production is same as that in case of chemical synthesis. The capping agent solution is used as the ambient liquid and the concentration and type of capping agent decides the size of the nanoparticle [33]. In addition to this, the particle size control has been achieved by varying parameters like, laser wavelength, laser fluence, laser pulse repetition rate etc. [16, 106]. However, controlling the shape of the nanoparticles produced by laser ablation has always been a challenge. Recently, the phenomena of oriented growth and aggregation has been used in tandem with laser ablation to gain control over the shape of the nanostructures. The efforts made by the researchers across the globe in this direction have been aptly documented in the review article written by Zeng *et.al.* [18]. The oriented growth and aggregation leads to the formation of high aspect ratio metallic nanostructures. Lin *et.al.* has reported a pioneer work in this direction by producing copper nanospindles by ablating a copper target in water without the use of any chemical agent(s) [45]. Similar work has been carried out by Liu *et.al.* where the authors produced GeO_2

nanoparticles, nanocubes and nanospindles in liquid media [104]. In both the studies, electric field was used as an external agent to control the growth of the direction of nanostructures.

Electric field assisted laser ablation in liquid (EFLAL) has evolved as an effective method to control both, shape as well as the size of nanoparticles produced by the process of laser ablation. It has been found that by changing the magnitude of the electric field, the shape of the nanostructures could be modified. Also, the aspect ratio of the nanostructures for a given shape has a direct dependence on the applied external electric field. The mechanism of formation of the nanostructures of specific shapes is based on the idea of oriented growth proposed by Banfield *et.al.* [158, 159]. In this growth mechanism, the bigger particles are assumed to have resulted from the aggregation of smaller particles in a defined direction of orientation. In addition, this process is thermodynamically favoured as well because when such smaller particles self-assemble by sharing a common crystallographic direction and combine over a planar interface, the overall energy of the system is reduced [45]. Along these lines, in the context of the present thesis, investigation of the effect of electric field on the shape and size of the metallic nanoparticles has been carried out towards the final stages of this work. It is to be mentioned here that these experiments are currently in progress and this appendix presents some of the preliminary findings of these experiments to demonstrate the potential of EFLAL in the context of the fabrication of nanostructures with defined shapes and sizes.

The experiment for laser ablation has been setup as discussed earlier in Section 3.2, Chapter 3. However, in the present set of experiments, the target geometry has been changed. The schematic diagram of the target has been shown in Figure A-II-1. The dimensions of the top plate and the target plate are 25mm × 25mm × 5 mm. The top plate has a hole to let the focussed laser beam pass through it. Both the plates are made up of 99.9% pure copper. The two plates are separated from each other by four Teflon spacers of length 15 mm each. The top and bottom plates have two screws that enable electrical connections so that the two plates can serve as two electrodes (positive and negative) during the laser ablation experiment. During the experiments the target plate was immersed in the experimental liquid media. The height of liquid column was maintained at 10mm.

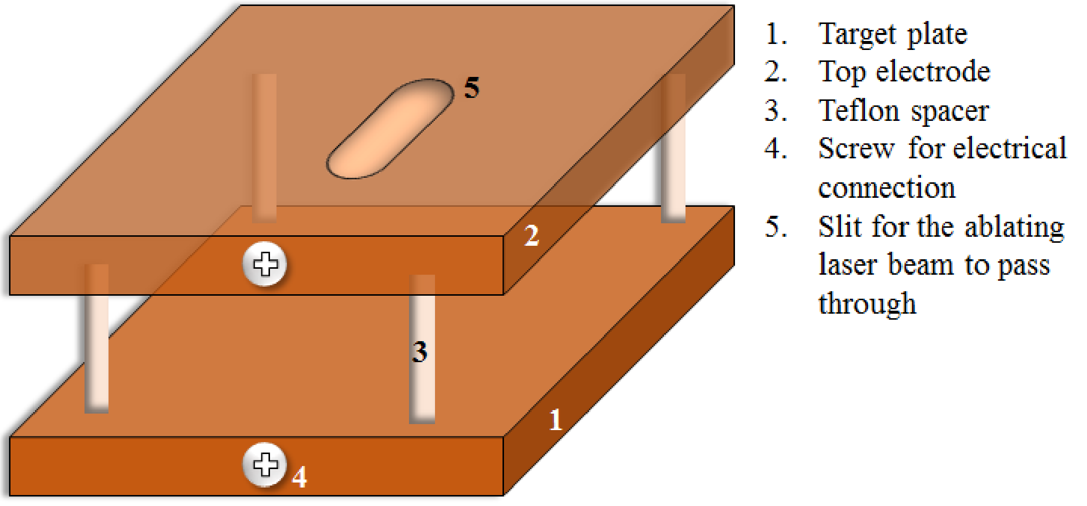

Figure A-II-1: Schematic diagram of the target cum electrode system for EFLAL

For preliminary observations, isopropyl alcohol (IPA) was chosen as the liquid media for EFLAL. Since the dielectric constant for water is high (≈80), to have an electric field of the order of few tens of V/cm, very high potential needs to be applied across the electrodes. In comparison to that, the dielectric constant of IPA is at least four times lower and is closer to 18 at 25^0C. The ablation was carried out for 30 minutes (9000 shots of laser @ 5 Hz). Laser fluence was maintained at 11J/cm^2. Three different configurations were used. The schematic diagram of these configurations have been shown in the Figure A-II-2 (a), (b) and (c). The diagrams shown in Figure A-II-2 (a) and (c) represent the same case as far as the magnitude is concerned, however, the direction of electric field is different in both the cases. These two different configurations have been made to identify if the direction of electric field brings in any difference in the shape and size of the particles obtained from the experiments. In the studies available in published literature the electrodes have been placed laterally and the experiments were performed. Therefore, any change in the polarity only changes the direction of electric field that is perpendicular to the incident ablating laser beam and hence to the produced plasma plume. Contrary to that, in the present setup, the change in polarity will bring in a change in the direction of the applied electric field which is parallel to the plasma plume. This is expected to affect the way the plume expands by influencing the dynamics of the charges (primarily electrons) in the plume. Hence, a change in the size of the particles is expected to occur if the polarity is changed, even though the shape may remain the same.

The corresponding SEM images of the nanoparticles produced in the three configurations have been shown in Figure A-II-2 (d), (e) and (f). The analysis of the images show that the mean sizes of the particles produced with the configurations shown in Figure A-II-2 (a), (b) and (c) are approximately 35 nm, 50 nm and 55 nm, respectively. The observed trend may be qualitatively explained by the way the plume behaves in the three

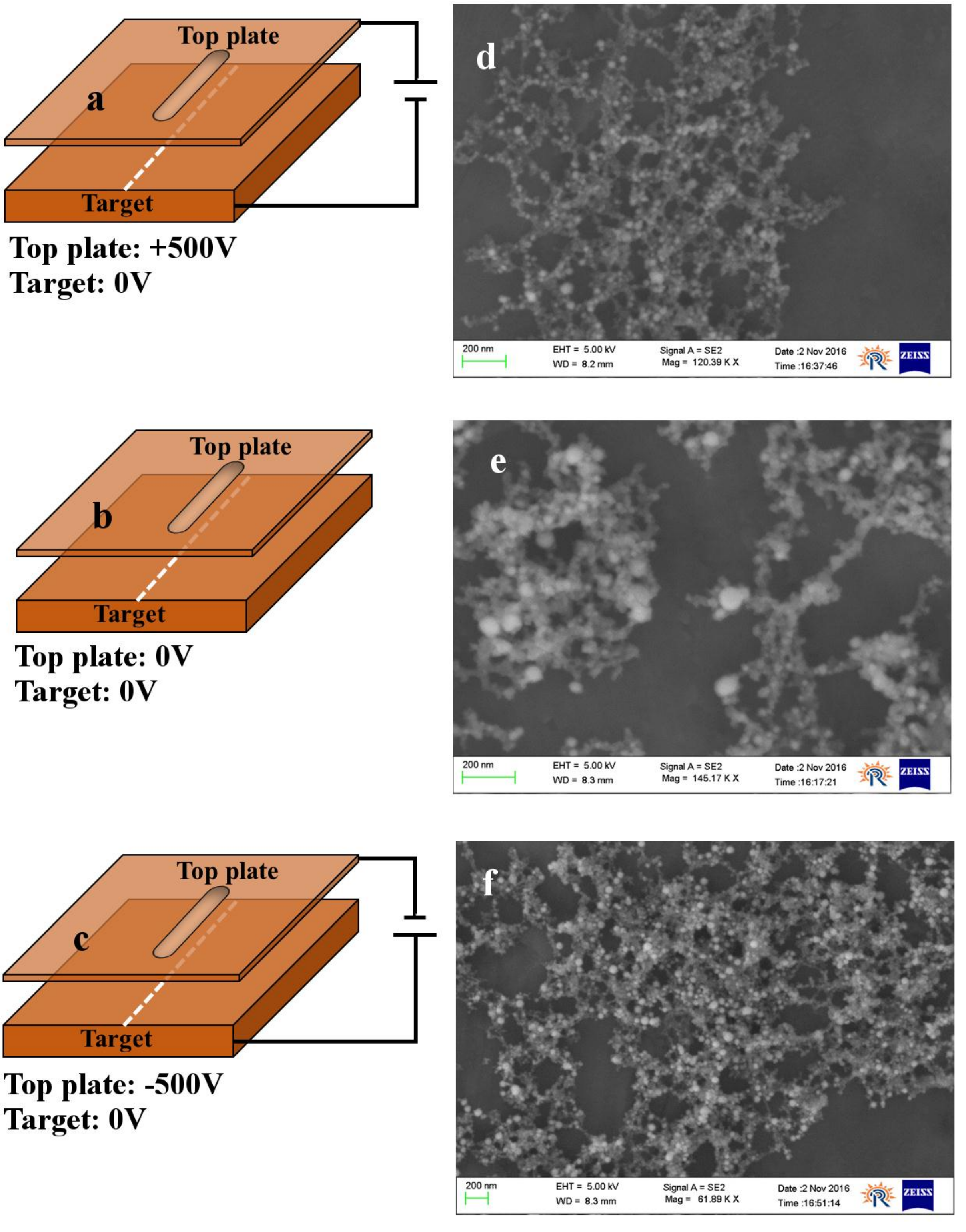

Figure A-II-2: Schematic diagram showing the different target configurations used for conducting the experiments, (a) target is positively biased, (b) target is unbiased and (c) target is negatively biased. The corresponding SEM images have been shown in (d), (e) and (f).

cases.

In the first case, shown in Figure A-II-2(a), the top plate is positive and hence the electrons in the plume will feel an upward force (along the expansion axis). However, the heavier positively charged Cu ions will be closer to the target surface and will experience a slight repulsive force. As the electrons try to move further, tend to feel a stronger collective attractive force from the Cu ions, which will tend to maintain the quasi neutrality of the plasma. Under the effect of these two opposing and competing forces (the resultant of which will try to damp the motion of the electron in either direction), the electrons will lose kinetic energy faster and the thermalisation will be quicker, leading to the formation of smaller size of nanoparticles. Physical interpretation of this phenomenon has been schematically shown in Figure A-II-3. It is noteworthy that not just electrons but the kinetic energy of ions (although lesser compared to that of electrons due to their heavier mass) will also decrease faster owing to the effect of the two opposing forces.

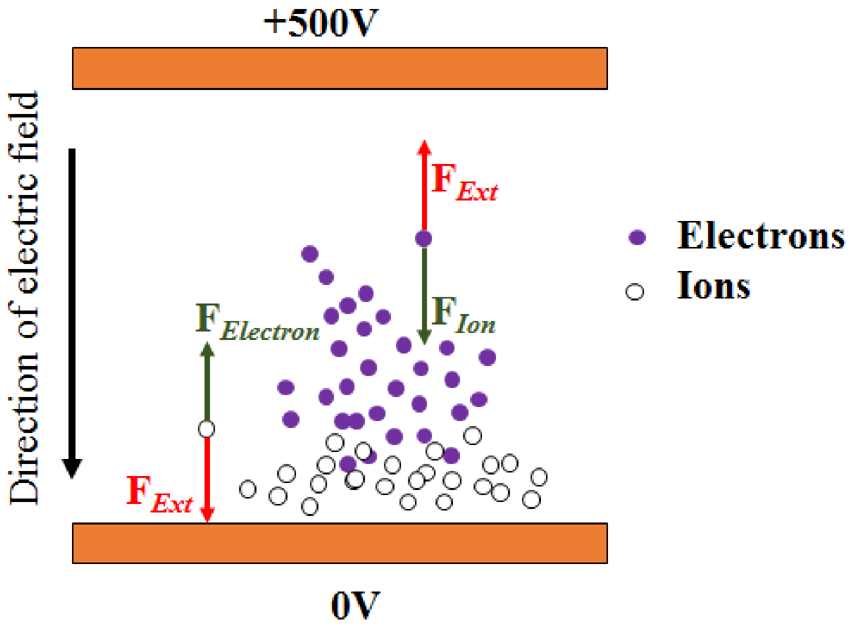

Figure A-II-3: Schematic interpretation of the forces that the electrons and ions in the plasma plume will experience when the target has been biased as per the configuration shown in Figure A-II-2(a)

In the third case, shown in Figure A-II-2(c), the electrons will not get attracted to the top plate and will experience a repulsive force due to the negatively biased top plate. In contrast, the positively charged Cu ions will feel an attractive force towards the top plate. In this case the force on the electrons will be towards the bottom plate only. This is due to the fact that the heavier positively charged ions will move slower under the influence of the applied electric field, but as the ablation takes place, the energetic electrons will move at a much higher velocity before the repulsive force due to the applied electric field (which is from top to bottom) starts affecting their motion. The ions will however, still be lagging the electron cloud. Thus the force on electrons due to the ions will also act downward and will add to the repulsive force because of the negatively biased top plate. This combined effect will enhance the resultant downward velocity of the electrons and the collision rate as well. Due to this the temperature of the plasma will be relatively higher than that achieved in the case of no electric field. Therefore, the thermalisation time will be more and the size of the nanoparticles is expected to be bigger than those produced in the case of positively biased or unbiased top plate. This process has been schematically depicted in Figure A-II-4. Here both, the electrons as well as the ions will get accelerated due to the fact that both the forces acting on them are in the same direction. This is expected to increase the collision rate leading to an increment in the temperature of the plasma and hence, a prolonged thermalisation phenomenon.

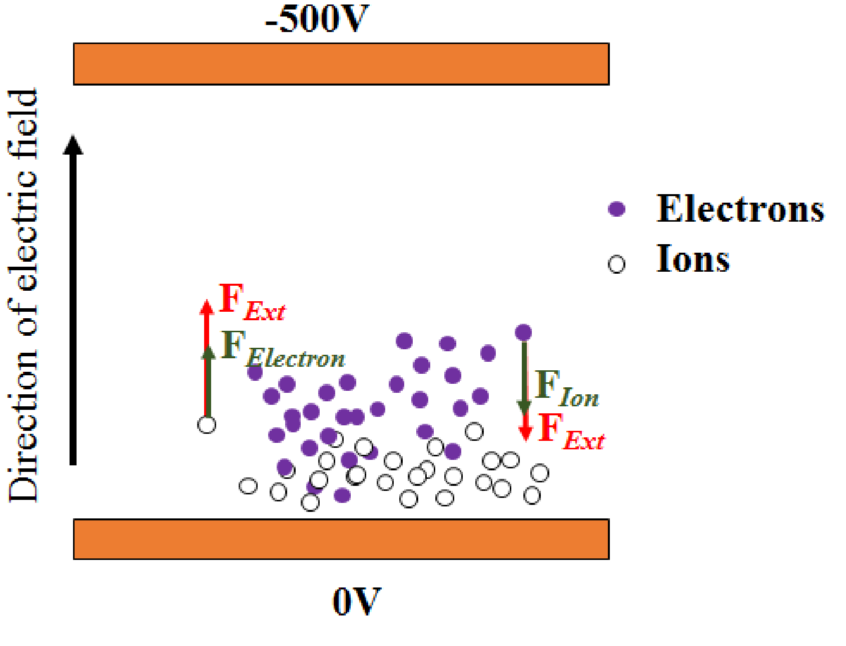

Figure A-II-4: Schematic interpretation the forces that the electrons and ions in the plasma plume will experience when the target has been biased as shown in Figure A-II-2(c)

References

1. R. F. Cozzens and R. B. Fox, Polym. Eng. Sci. **18**, 900 (1978).

2. P. E. Dyer and J. Sidhu, J. Appl. Phys. **64**, 4657 (1988).

3. S. Amoruso, R. Bruzzese, N. Spinelli, and R. Velotta, J. Phys. B At. Mol. Opt. Phys. **32**, 131 (1999).

4. D. . Rusak, B. . Castle, B. . Smith, and J. . Winefordner, TrAC Trends Anal. Chem. **17**, 453 (1998).

5. F. Kokai, K. Takahashi, K. Shimizu, M. Yudasaka, and S. Iijima, Appl. Phys. A Mater. Sci. Process. **69**, 223 (1999).

6. K. Song, D. Kim, H. Cha, Y. Kim, E. C. Jung, I. Choi, H. S. Yoo, and S. Oh, Microchem. J. **76**, 95 (2004).

7. a C. Woods and C. G. Parigger, J. Phys. Conf. Ser. **548**, 12053 (2014).

8. J. F. Ready, Eff. High-Power Laser Radiat. 317 (1971).

9. A. G. Doukas, T. J. Flotte, O. As, and T. J. Flotte, Ultrasound I N Med. Biol. Biol. **22**, 151 (1996).

10. R. O. Esenaliev, A. a Oraevsky, V. S. Letokhov, A. a Karabutov, and T. V Malinsky, Lasers Surg. Med. **13**, 470 (1993).

11. I. Akhatov, O. Lindau, A. Topolnikov, R. Mettin, N. Vakhitova, and W. Lauterborn, Phys. Fluids **13**, 2805 (2001).

12. L. Martí-López, R. Ocaña, J. a Porro, M. Morales, and J. L. Ocaña, Appl. Opt. **48**, 3671 (2009).

13. V. Lazic, J. J. Laserna, and S. Jovicevic, Spectrochim. Acta - Part B At. Spectrosc. **82**, 42 (2013).

14. V. Lazic, J. J. Laserna, and S. Jovicevic, Spectrochim. Acta - Part B At. Spectrosc. **82**, 50 (2013).

15. M. F. Becker, J. R. Brock, H. Cai, D. E. Henneke, J. W. Keto, J. Lee, W. T. Nichols, and H. D. Glicksman, Nanostructured Mater. **10**, 853 (1998).

16. T. Tsuji, K. Iryo, N. Watanabe, and M. Tsuji, **202**, 80 (2002).

17. B. Kumar and R. K. Thareja, J. Appl. Phys. **108**, 1 (2010).

18. H. Zeng, X. W. Du, S. C. Singh, S. A. Kulinich, S. Yang, J. He, and W. Cai, Adv. Funct. Mater. **22**, 1333 (2012).

19. L. Tunna, A. Kearns, W. O'Neill, and C. J. Sutcliffe, Opt. Laser Technol. **33**, 135 (2001).

20. L. Torrisi, S. Gammino, L. Andò, V. Nassisi, D. Doria, and A. Pedone, Appl. Surf. Sci. **210**, 262 (2003).
21. C. Liu, X. L. Mao, S. S. Mao, X. Zeng, R. Greif, and R. E. Russo, Anal. Chem. **76**, 379 (2004).
22. V. Amendola, P. Riello, S. Polizzi, S. Fiameni, C. Innocenti, C. Sangregorio, and M. Meneghetti, J. Mater. Chem. **21**, 18665 (2011).
23. B. Kumar and R. K. Thareja, Phys. Plasmas **19**, (2012).
24. M. Han, Y. Gong, J. Zhou, C. Yin, F. Song, N. Muto, T. Takiya, and Y. Iwata, Phys. Lett. Sect. A Gen. At. Solid State Phys. **302**, 182 (2002).
25. R. Tanabe, T. T. P. Nguyen, T. Sugiura, and Y. Ito, Appl. Surf. Sci. **351**, 327 (2015).
26. S. I. Dolgaev, A. V. Simakin, V. V. Voronov, G. A. Shafeev, and F. Bozon-Verduraz, Appl. Surf. Sci. **186**, 546 (2002).
27. A. Kumar, R. K. Singh, V. Prahlad, and H. C. Joshi, J. Appl. Phys. **104**, 1 (2008).
28. J. Turkevich, Gold Bull. **18**, 86 (1985).
29. J. Turkevich, God Bull. **18**, 125 (1985).
30. J. Turkevich, P. C. Stevenson, J. Hillier, Discussion of Faraday Society. **11**, 55 (1951).
31. G. Compagnini, A. A. Scalisi, and O. Puglisi, J. Appl. Phys. **94**, 7874 (2003).
32. X. Huang and M. A. El-Sayed, J. Adv. Res. **1**, 13 (2010).
33. F. Mafuné, J. Kohno, Y. Takeda, T. Kondow, and H. Sawabe, J. Phys. Chem. B **104**, 9111 (2000).
34. J. N. Anker, W. P. Hall, O. Lyandres, N. C. Shah, J. Zhao, and R. P. Van Duyne, Nat. Mater. **7**, 442 (2008).
35. M. Rai, A. Yadav, and A. Gade, Biotechnol. Adv. **27**, 76 (2009).
36. M. C. Edmundson, M. Capeness, and L. Horsfall, N. Biotechnol. **31**, 572 (2014).
37. W. Cheng, J. Jiang, S. Dong, and E. Wang, Chem. Commun. (Camb). 1706 (2002).
38. G. Frens, Nat. Phys. Sci. **241**, 20 (1973).
39. N. R. Jana, N. R. Jana, L. Gearheart, L. Gearheart, C. J. Murphy, and C. J. Murphy, J. Phys. Chem. B **105**, 4065 (2001).
40. T. P. Yadav, R. M. Yadav, and D. P. Singh, Nanosci. Nanotechnol. **2**, 22 (2012).
41. Y. Sun, Science. **298**, 2176 (2002).
42. Z. Wu, S. Yang, and W. Wu, Nanoscale **8**, 1237 (2016).
43. K. An and G. A. Somorjai, ChemCatChem **4**, 1512 (2012).
44. J.-M. Williford, J. L. Santos, R. Shyam, and H.-Q. Mao, Biomater. Sci. **3**, 894 (2015).
45. X. Z. Lin, P. Liu, J. M. Yu, and G. W. Yang, J. Phys. Chem. C **113**, 17543 (2009).

46. D. Sapkota, Y. Li, O. R. Musaev, J. M. Wrobel, and M. B. Kruger, J. Laser Appl. **29**, 1 (2017).
47. S. B. Wen, X. Mao, R. Greif, and R. E. Russo, J. Appl. Phys. **101**, (2007).
48. J. J. Chang and B. E. Warner, Appl. Phys. Lett. **69**, 473 (1996).
49. A. De Giacomo, M. Dell'Aglio, R. Gaudiuso, S. Amoruso, and O. De Pascale, Spectrochim. Acta - Part B At. Spectrosc. **78**, 1 (2012).
50. Q. Arabia, Tawfik W., S. Arabia, L. I. Breakdown, Q. Arabia, and Tawfik W., Optoelectron. Adv. Mater. - Rapid Commun. **8**, 741 (2014).
51. A. Tamura, A. Matsumoto, K. Fukami, N. Nishi, and T. Sakka, J. Appl. Phys. **117**, (2015).
52. X. Chen, R.-Q. Xu, J.-P. Chen, Z.-H. Shen, L. Jian, and X.-W. Ni, Appl. Opt. **43**, 3251 (2004).
53. R. Zhao, R. qing Xu, Z. hua Shen, J. Lu, and X. wu Ni, Opt. Laser Technol. **39**, 968 (2007).
54. S. S. Harilal, G. V. Miloshevsky, P. K. Diwakar, N. L. Lahaye, and A. Hassanein, Phys. Plasmas **19**, 1 (2012).
55. D. Breitling, H. Schittenhelm, P. Berger, F. Dausinger, H. Huegel, and H. Hügel, Appl. Phys. A **69**, S505 (1999).
56. T. Y. Katsumi Hirano, Chiaki Matsumoto, Katsuji Shimoda, **24**, 1518 (1985).
57. Y. Tao, M. S. Tillack, S. S. Harilal, K. L. Sequoia, B. O'Shay, and F. Najmabadi, J. Phys. D. Appl. Phys. **39**, 4027 (2006).
58. H. Zhang, J. Lu, Z. Shen, and X. Ni, Opt. Commun. **282**, 1720 (2009).
59. A. Srivastava, K. Muralidhar, and P. K. Panigrahi, J. Cryst. Growth **267**, 348 (2004).
60. Y. Utsunomiya, T. Kajiwara, T. Nishiyama, K. Nagayama, and S. Kubota, Appl. Phys. A Mater. Sci. Process. **99**, 641 (2010).
61. G. W. Yang, Prog. Mater. Sci. **52**, 648 (2007).
62. J. C. Miller, *Laser Ablation: Principles and Applications* (Springer-Verlag, 1991).
63. J. C. Miller, AIP Conf. Proc. **288**, 619 (1993).
64. J. A. Eastman, S. U. S. Choi, S. Li, W. Yu, and L. J. Thompson, Appl. Phys. Lett. **78**, 718 (2001).
65. R. Srinivasan, B. Braren, K. G. Casey, and M. Yeh, Appl. Phys. Lett. **55**, 2790 (1989).
66. R. Petkovšek and P. Gregorčič, J. Appl. Phys. **102**, 1 (2007).
67. R. Petkovsek, P. Gregorcic, and J. Mozina, Meas. Sci. Technol. **18**, 2972 (2007).
68. R. Fabbro, J. Fournier, P. Ballard, D. Devaux, and J. Virmont, J. Appl. Phys. **68**, 775

(1990).
69. W. S. Ã, T. Nakano, N. Takada, and K. Sasaki, **116202**, (n.d.).
70. V. Lazic, S. Jovicevic, and M. Carpanese, Appl. Phys. Lett. **101**, (2012).
71. B. Kumar, R. K. Singh, and A. Kumar, **83511**, 1 (2013).
72. W. Demtroeder, *Laser Spectroscopy - Basic Concepts and Instrumentation*, Third (Springer, 2003).
73. S. Parker, Br. Dent. J. **202**, 445 (2007).
74. R. K. Singh and J. Narayan, Phys. Rev. B **41**, 8843 (1990).
75. J. P. Anthes, M. A. Gusinow, and M. K. Matzen, Phys. Rev. Lett. **41**, 1300 (1978).
76. F. Dahmani and T. Kerdja, **9**, 769 (1991).
77. R. A. Burdt, S. Yuspeh, K. L. Sequoia, Y. Tao, M. S. Tillack, and F. Najmabadi, J. Appl. Phys. **106**, 2 (2009).
78. P. Yeates and E. T. Kennedy, J. Appl. Phys. **108**, (2010).
79. P. Yeates and E. T. Kennedy, Phys. Plasmas **18**, (2011).
80. R. Ecault, L. Berthe, F. Touchard, M. Boustie, E. Lescoute, A. Sollier, and H. Voillaume, J. Phys. D. Appl. Phys. **48**, 95501 (2015).
81. T. T. P. Nguyen, R. Tanabe, and Y. Ito, Appl. Phys. Lett. **102**, 1 (2013).
82. T. T. P. Nguyen, R. Tanabe, and Y. Ito, Appl. Phys. A Mater. Sci. Process. **122**, 1 (2016).
83. M. N. R. Ashfold, F. Claeyssens, G. M. Fuge, and S. J. Henley, 23 (2004).
84. S. S. Harilal, B. E. Brumfield, B. D. Cannon, and M. C. Phillips, Anal. Chem. **88**, 2296 (2016).
85. H. Masuhara, Bull. Chem. Soc. Jpn. **86**, 755 (2013).
86. I. Turovets, D. Palanker, Y. Kokotov, I. Hemo, and A. Lewis, J. Appl. Phys. **79**, 2689 (1996).
87. Z. Yan and D. B. Chrisey, J. Photochem. Photobiol. C Photochem. Rev. **13**, 204 (2012).
88. M. Dell'Aglio, R. Gaudiuso, O. De Pascale, and A. De Giacomo, Appl. Surf. Sci. **348**, 4 (2015).
89. W. Soliman, T. Nakano, N. Takada, and K. Sasaki, Jpn. J. Appl. Phys. **49**, (2010).
90. K. Y. Lim, P. A. Quinto-Su, E. Klaseboer, B. C. Khoo, V. Venugopalan, and C. D. Ohl, Phys. Rev. E - Stat. Nonlinear, Soft Matter Phys. **81**, 1 (2010).
91. H. Schmidt, Appl. Organomet. Chem. **15**, 331 (2001).
92. K. Habiba, V. I. Makarov, B. R. Weiner, and G. Morell, in (One Central Press, 2014), pp. 263–292.
93. M. Ullmann, S. K. Friedlander, and A. Schmidt-ott, 499 (2002).

94. F. Bozon-Verduraz, R. Brayner, V. V. Valerii, N. A. Kirichenko, V. S. Aleksandr, and A. S. Georgii, Quantum Electron. **33**, 714 (2003).
95. A. H. Lu, E. L. Salabas, and F. Schüth, Angew. Chemie - Int. Ed. **46**, 1222 (2007).
96. Y. Tamaki, T. Asahi, and H. Masuhara, Japanese J. Appl. Physics, Part 1 Regul. Pap. Short Notes Rev. Pap. **42**, 2725 (2003).
97. A. Menéndez-Manjón, B. N. Chichkov, and S. Barcikowski, J. Phys. Chem. C **114**, 2499 (2010).
98. N. Takada, T. Sasaki, and K. Sasaki, Appl. Phys. A Mater. Sci. Process. **93**, 833 (2008).
99. J. S. Golightly and A. W. Castleman, J. Phys. Chem. B **110**, 19979 (2006).
100. P. V Kamat, M. Flumiani, and G. V Hartland, J. Phys. Chem. B **102**, 3123 (1998).
101. P. Vasa, R. Sharma, M. Singh, A. K. Dharmadhikari, J. A. Dharmadhikari, and D. Mathur, Mat. Res. Express **1**, 35028 (2014).
102. F. Mafuné, J. Y. Kohno, Y. Takeda, and T. Kondow, J. Phys. Chem. B **105**, 9050 (2001).
103. D. Werner and S. Hashimoto, Langmuir **29**, 1295 (2013).
104. P. Liu, C. X. Wang, X. Y. Chen, and G. W. Yang, J. Phys. Chem. C **112**, 13450 (2008).
105. M. H. Mahdieh and B. Fattahi, Appl. Surf. Sci. **75**, 188 (2015).
106. M. H. Mahdieh and B. Fattahi, Appl. Surf. Sci. **329**, 47 (2015).
107. L. E. Euliss, J. A. DuPont, S. Gratton, and J. DeSimone, Chem. Soc. Rev. **35**, 1095 (2006).
108. S. Bhatia, in *Nat. Polym. Drug Deliv. Syst.* (Springer, 2016), pp. 33–93.
109. A. Albanese, P. S. Tang, and W. C. W. Chan, Annu. Rev. Biomed. Eng. **14**, 1 (2012).
110. B. Ankamwar, in *Biomed. Eng. - Tech. Appl. Med.* (Intech, 2012), pp. 93–114.
111. T. M. Allen and P. R. Cullis, Science. **303**, 1818, (2003).
112. H. Zeng, W. Cai, Y. Li, J. Hu, and P. Liu, J. Phys. Chem. B **109**, 18260 (2005).
113. C. Porneala and D. A. Willis, Appl. Phys. Lett. **89**, (2006).
114. D. B. Geohegan, A. A. Puretzky, G. Duscher, and S. J. Pennycook, Appl. Phys. Lett. **72**, 2987 (1998).
115. A. Mohanta and R. K. Thareja, J. Appl. Phys. **106**, 2 (2009).
116. S. Arabia, Tawfik W. Optoelectron. Adv. Mater. Rapid Commun. **8**, 741 (2014).
117. C. M. Limbach and R. B. Miles, 52nd Aerosp. Sci. Meet. 1 (2014).
118. H. Gratz, A. Penzkofer, and P. Weidner, J. Non. Cryst. Solids **189**, 50 (1995).
119. R. G. Knollenberg, J. Aerosol Sci. **20**, 331 (1989).
120. D. B. Geohegan and A. A. Puretzky, Appl. Phys. Lett. **67**, 197 (1995).

121. H. T. Chen, W. H. Christiansen, and H. Chen, **1619**, (1995).
122. R. Azambuja, M. Eloy, G. Figueira, and D. Neely, J. Phys. D. Appl. Phys. **32**, L35 (1999).
123. M. Ye and D. Jiang, Rev. Sci. Instrum. **70**, 691 (1999).
124. D. Breitling, H. Schittenhelm, P. Berger, and F. Dausinger, Appl. Phys. A **69**, S505 (1999).
125. J. U. Kim, H. J. Lee, C. Kim, G. H. Kim, and H. Suk, J. Appl. Phys. **94**, 5497 (2003).
126. K. Bose, *Testing and Measurement of Physical Parameters Using Holographic interferometry* (Birla Institute of Technology 2007).
127. D. Breitling, H. Schittenhelm, P. Berger, F. Dausinger, and H. Hügel, Shock **508**, 505 (1999).
128. P. Hough, T. J. Kelly, C. Fallon, C. McLoughlin, P. Hayden, E. T. Kennedy, J. P. Mosnier, S. S. Harilal, and J. T. Costello, Meas. Sci. Technol. **23**, 125204 (2012).
129. L. Berthe, R. Fabbro, P. Peyre, L. Tollier, and E. Bartnicki, J. Appl. Phys. **82**, 2826 (1997).
130. J. Ma, Z. Wang, M. Vo, and L. Luu, Appl. Opt. **50**, 6399 (2011).
131. J. Ma, Z. Wang, B. Pan, T. Hoang, M. Vo, and L. Luu, Appl. Opt. **50**, 2425 (2011).
132. J. Ma, Z. Wang, M. Vo, and B. Pan, J. Opt. **14**, 65403 (2012).
133. D. C. Ghiglia and M. D. Pritt, *Two Dimensional Phase Unwrapping Theory, Algorithm and Software* (Wiley, 1998).
134. Q. Kemao, W. Gao, and H. Wang, Appl. Opt. **47**, 5420 (2008).
135. S. Mohanan and A. Srivastava, Appl. Opt. **53**, 2331 (2014).
136. S. Ma, H. Gao, and L. Wu, Appl. Opt. **47**, 1350 (2008).
137. S. Ma, Appl. Opt. **50**, 6512 (2011).
138. Y. Liu and P. H. Daum, J. Aerosol Sci. **39**, 974 (2008).
139. M. Born and E. Wolf, *Principles of Optics* (Cambridge University Press, 2000).
140. A. W. J. Burner and W. Goad, NASA Tech. Memo. (1980).
141. M. J. Madsen, D. R. Brown, S. R. Krutz, and M. J. Milliman, Am. J. Phys. **79**, 428 (2011).
142. E. T. Fogg, A. N. Hixson, and A. R. Thompson, Anal. Chem. **27**, 1609 (1955).
143. K. E. Paul P, D. Haridas, and A. Srivastava, Int. J. Therm. Sci. **96**, 70 (2015).
144. D. Haridas, N. S. Rajput, and A. Srivastava, Int. J. Heat Mass Transf. **88**, 713 (2015).
145. S. George, R. K. Singh, V. P. N. Nampoori, and A. Kumar, **377**, 391 (2013).
146. T. Y. Choi and C. P. Grigoropoulos, J. Appl. Phys. **92**, 4918 (2002).

147. H. Hornung, Annu. Rev. Fluid Mech. **18**, 33 (1986).
148. D. Haridas, N. S. Rajput, and A. Srivastava, Int. J. Heat Mass Transf. **88**, 713 (2015).
149. L. Godson, B. Raja, D. Mohan Lal, and S. Wongwises, Renew. Sustain. Energy Rev. **14**, 629 (2010).
150. L. Martí-López, R. Ocaña, E. Piñeiro, and A. Asensio, Phys. Procedia **12**, 442 (2011).
151. W. M. Haynes, editor , *CRC Handbook of Chemistry and Physics*, 97th ed. (CRC Press, 2016).
152. Z. Lin, L. V. Zhigilei, and V. Celli, Phys. Rev. B - Condens. Matter Mater. Phys. **77**, 1 (2008).
153. R. M. Tilaki, A. Iraji zad, and S. M. Mahdavi, Appl. Phys. A **88**, 415 (2007).
154. Y.-H. Yeh, M.-S. Yeh, Y.-P. Lee, and C.-S. Yeh, Chem. Lett. **27**, 1183 (1998).
155. N. Haustrup and G. M. O'Connor, Phys. Procedia **12**, 46 (2011).
156. M. Stafe, A. Marcu, and N. N. Puscas, *Pulsed Laser Ablation of Solids* (2014).
157. K. Choudhury, R. K. Singh, S. Narayan, A. Srivastava, and A. Kumar, Phys. Plasmas **23**, (2016).
158. R. L. Penn and J. F. Banfield, Science. **281**, 969 (1998)
159. J. F. Banfield, S. A. Welch, H. Zhang, T. T. Ebert, and R. L. Penn, Science **289**, 751 (2000).

List of Publications

Journal

1. Kaushik Choudhury, R. K. Singh, Surya Narayan, Atul Srivastava, Ajai Kumar, Time resolved interferometric study of the plasma plume induced shockwave in confined geometry: 2D mapping of the ambient and plasma density, *Physics of Plasmas*, **23,** 042108 (2016).
2. Kaushik Choudhury, R. K. Singh, Surya Narayan, Atul Srivastava, Ajai Kumar, Time resolved whole field study of plasma plume-induced shockwave in liquid media of different densities, *Applied Physics B*, **123**, 163 (2017).
3. Kaushik Choudhury, R. K. Singh, Mukesh Ranjan, Ajai Kumar, Atul Srivastava, A novel method for fabrication of size-controlled metallic nanoparticles, *Proc. SPIE 10603, Photonics, Devices, and Systems VII*, 1060304 (2017).
4. Kaushik Choudhury, R. K. Singh, Ajai Kumar, Atul Srivastava, Controlling the size distribution of nanoparticles through the use of physical boundaries during laser ablation in liquids (Manuscript under review with Applied Surface Science).
5. Kaushik Choudhury, R. K. Singh, Ajai Kumar, Atul Srivastava, Controlling the size distribution of nanoparticles through the use of electric field during laser ablation in liquids (Manuscript under preparation).

Conference

1. Kaushik Choudhury, R. K. Singh, Surya Narayan, Atul Srivastava, Ajai Kumar, Interferometric and Shadowgraphic Study of Laser Plasma Induced Shockwaves, *q-PaCE 2016*, held at IIT (ISM), Dhanbad, 9th to 11th January 2016.
2. Kaushik Choudhury, R. K. Singh, Mukesh Ranjan, Ajai Kumar, Atul Srivastava, A novel method for fabrication of size-controlled metallic nanoparticles, *Photonics Prague 2017*, held at Prague, Czech Republic, 28th to 30th August 2017.

Acknowledgements

This thesis reflects my journey this far as a researcher, but this wouldn't have been possible without all those who have believed in me and supported me in more than one ways in this. This acknowledgement is just a compilation of words, for feelings – I can't write.

I am grateful to Professor Atul Srivastava for guiding me through the course of my research work. I express my sincere gratitude to him for having faith in me during the most unproductive phase of my Ph.D. tenure. The ideas presented in this thesis would not have seen the light of the day had he not given me the freedom to explore these even after knowing that I had very less time and a lot to do. I am thankful to you for all the technical and moral support that you had given to me.

I would like to thank Professor Ajai Kumar for extending support to me when I needed it the most. Without his generosity, this thesis would not have been completed. I am thankful to you for having trusted me with some of the best instruments that I have used in the experiments. I would like to thank him for the fruitful scientific discussions that helped me move ahead whenever I got stuck.

I would like to thank Professor Wenlong Cheng for his patience and consistent support during my research work. I would like to thank him for letting me reconsider my thesis topic and helping me in switching to a different topic when I was stuck and struggling.

I am indebted to Dr. Rajesh Kumar Singh (Scientific Officer E) of the Laser Diagnostics Group, IPR for his cooperation. He had always been available for the scientific discussions and to sort out the technical problems with any of the instruments. Without his help it would have been difficult to smoothly perform the complex experiments.

My sincere thanks to Professor Suneet Singh of Department of Energy Science and Engineering (IIT Bombay) for his constructive feedbacks as an RPC member during all the discussions. I express my sincere gratitude to him for introducing me to Professor Srivastava and showing me a way to continue with my PhD when I had lost hopes.

I would like to thank my colleagues from the Optical Instrumentation Lab, especially Srinivas, Gulshan, Surya, Divya and Biswajit for the time that they have given to me. I would also like to thank my lab-mates Alamgir and Narayan from the Laser Diagnostics Laboratory at Institute for Plasma Research at Gandhinagar for the insightful discussions.

My sincere thanks to my brothers Dr. Shakil and Prasoon for being the pillar of supports. Without you guys, I would not have reached this point. Thanks to both of you for all your time and effort to get me out of my dilemmas in personal and professional life. I would like to thank my friends Amit, Dr. Atif, Reeshab and Varun for tolerating me when I was at my worst and the help that you guys have extended, specially letting me use your rooms when I needed it the most. A special thanks goes to my girlfriend Shayeri Sarkar for standing by my side and trusting and encouraging me. I wouldn’t have been so firm with my decisions without you believing in them.

Last but not the least, this thesis would not have been completed without the support I received from my mom and dad. You two have been a source of inspiration to me and I really don’t have words to express my gratitude to you for letting me chose my own path since I started with my studies. Whatever little I did this far is all because of your support and blessings.